

A MODELING STUDY OF HORIZONTAL TRANSPORT AND RESIDENCE TIME IN THE  
DUPLIN RIVER ESTUARY, SAPELO ISLAND GA

by

CHARLES JARED MCKNIGHT

(Under the direction of Daniela Di Iorio)

ABSTRACT

A high-resolution, three-dimensional, hydrodynamic model of the Duplin River estuary on Sapelo Island Georgia has been developed using Finite Volume Community Ocean Model. Using a model to describe transport and retention is a good way to estimate the efficiency of an estuary at remediating contaminants. The model shows good agreement with time series of sea surface height and salinity from monitoring stations within the domain. The model does well at predicting tidal oscillations and subtidal SSH and salinity variations. However, there is room for improvement with regard to salinity variability in the upper model domain. A Lagrangian particle tracking analysis was carried out to study the effects of semi-diurnal tides, spring/neap tidal cycles, and seasonal forcings on residence times. Residence time is most sensitive to the stage of the tide (slack high or slack low) when starting the particle tracking and had maximum values on slack low water. Neap tides had characteristically longer residence times than spring tides. Residence time was also dependent on seasonal changes and was higher during periods of low river discharge which correspond to higher sea surface inundation than periods of high river discharge. An Eulerian salt flux analysis was carried out to study the relative roles of advective and dispersive flux on transport processes. The residual or advective flux, dominates the transport within the system and marsh circulation in the upper reaches shows net inward movement along the channel and net outward movement

over the marsh. Tidal flux dominates the dispersive flux over estuarine exchange flux and thus controls the horizontal dispersion. The horizontal dispersion coefficient was dependent on seasonal river discharge as the horizontal salinity gradient switches from a positive to a negative estuary causing very large and highly variable values during periods of high river discharge. Alternatively, the horizontal dispersion coefficient was more periodic and controlled by the spring/neap cycle, showing maxima on spring tides during the season of low river discharge and high sea surface inundation.

INDEX WORDS: hydrodynamic modeling, Duplin River estuary, GCE LTER, FVCOM, horizontal transport, Lagrangian particle tracking, residence time

A MODELING STUDY OF HORIZONTAL TRANSPORT AND RESIDENCE TIME IN THE  
DUPLIN RIVER ESTUARY, SAPELO ISLAND GA

by

CHARLES JARED MCKNIGHT

B.S., B.S., Clemson University 2006, 2012

A Thesis Submitted to the Graduate Faculty  
of The University of Georgia in Partial Fulfillment  
of the  
Requirements for the Degree

MASTER OF SCIENCE

ATHENS, GEORGIA

2016

© 2016

Charles Jared Mcknight

All Rights Reserved

A MODELING STUDY OF HORIZONTAL TRANSPORT AND RESIDENCE TIME IN THE  
DUPLIN RIVER ESTUARY, SAPELO ISLAND GA

by

CHARLES JARED MCKNIGHT

Approved:

Major Professor: Daniela Di Iorio

Committee: David Stooksbury (co-Major Professor)  
Renato Castelao  
C. Brock Woodson  
Christof Meile

Electronic Version Approved:

Suzanne Barbour  
Dean of the Graduate School  
The University of Georgia  
August 2016

## ACKNOWLEDGEMENTS

There are many people who helped and contributed to this work that I need to thank. Thank you Dr. Daniela Di Iorio, for being supportive and helping me finish this research. You were always available and took time to help me understand concepts and grow as a scientist. Thanks to the members of my committee: Dr. David Stooksbury, Dr. Brock Woodson, Dr. Renato Castelao, and Dr. Christof Meile for being patient and helpful throughout this process. I am very grateful to Dr. John Schalles for allowing us to use his canoe and outboard motor to carry out the echo sounding. Thanks to everyone on the GCE LTER project for their feedback and contributions to this work.

Thank you to my wife, Ciara, for being supportive of me and encouraging during this experience and to our daughter, Cherry. Even though she hasn't been born yet, she has been a major motivation to complete this work.

I am grateful to Jonathan Taylor for helping me with the early stages of the research and giving me MATLAB pointers. Thanks David Miklesh for always being willing to talk through research problems and for providing valuable feedback. Thanks Dr. Yuntao Wang for helping me with some of the residence time analysis codes.

Thank you to the staff and faculty at the Georgia Advanced Computer Resource Center (GACRC) for their help setting up and compiling the model, especially Dr. Shan Ho Tsai, who was extremely helpful during this process.

I am grateful for everyone from the FVCOM User's meeting in 2015 for their input on my work. It was very important in moving this research along. I would like to thank Dr. Lianyuan Zheng, who helped me with the groundwater input files by showing me an example. I would also like to thank Dr. Jianhua Qui, who helped me get the Lagrangian particle tracking module to work and also helped with creating input files.

Thanks to UGAMI for all the logistical support when we were out doing our field sampling, specifically Jacob Shalack and Caroline Reddy. I would also like to acknowledge NSF (grant OCE-1237140) for funding this work.

## TABLE OF CONTENTS

	Page
ACKNOWLEDGEMENTS . . . . .	iv
LIST OF FIGURES . . . . .	viii
LIST OF TABLES . . . . .	xii
CHAPTER	
1 INTRODUCTION . . . . .	1
1.1 MOTIVATION . . . . .	1
1.2 SITE DESCRIPTION . . . . .	4
1.3 OBJECTIVES . . . . .	8
1.4 THESIS OUTLINE . . . . .	8
2 METHODS AND MODEL DESCRIPTION . . . . .	10
2.1 HIGH RESOLUTION DIGITAL ELEVATION MODEL . . . . .	10
2.2 MESHING PROCESS . . . . .	12
2.3 MESH QUALITY . . . . .	17
2.4 DESCRIPTION OF MODEL FORCINGS . . . . .	17
2.5 FVCOM3.2.2 . . . . .	20
2.6 COMPUTATIONAL RESOURCES . . . . .	22
2.7 MODEL SENSITIVITY . . . . .	23
2.8 DATA/MODEL COMPARISONS . . . . .	30
3 RESIDENCE TIMES THROUGH LAGRANGIAN PARTICLE TRACKING . . . . .	36
3.1 INTRODUCTION . . . . .	36

3.2	METHODS . . . . .	37
3.3	RESULTS AND DISCUSSION . . . . .	40
3.4	SUMMARY AND CONCLUSIONS . . . . .	48
4	HORIZONTAL TRANSPORT AND SALT FLUX ANALYSIS THROUGH EULERIAN DECOMPOSITION . . . . .	52
4.1	INTRODUCTION . . . . .	52
4.2	METHODS . . . . .	58
4.3	RESULTS AND DISCUSSION . . . . .	75
4.4	SUMMARY AND CONCLUSIONS . . . . .	88
5	CONCLUSIONS AND FUTURE RECOMMENDATIONS . . . . .	93
5.1	SUMMARY OF MAJOR CONCLUSIONS . . . . .	93
5.2	FUTURE RECOMMENDATIONS . . . . .	95
	BIBLIOGRAPHY . . . . .	98

## LIST OF FIGURES

1.1	An infrared satellite view of the GCE domain together with long term monitoring stations. The Duplin River model domain is outlined in yellow on Sapelo Island, Georgia. . . . .	6
1.2	An infrared satellite view of the Duplin domain together with long term monitoring sites at Marsh Landing (ML) and GCE 10. The Duplin model domain is outlined in yellow. . . . .	7
2.1	The original bathymetry map with merged, corrected LIDAR and swath bathymetry referenced to mean sea level (MSL in m). . . . .	11
2.2	a) The field work mascot. b)The canoe setup with a RTK GPS and echo sounder attached. . . . .	13
2.3	High resolution echo sounding depths in yellow and exaggerated in size are superimposed on merged, corrected LIDAR and swath data (referenced to MSL). . . . .	14
2.4	A close up example of the mesh in the mid-Duplin. . . . .	15
2.5	The 4 m digital elevation model (DEM) interpolated to the model mesh with monitoring stations identified. . . . .	16
2.6	GCE6 sea surface height, temperature, and salinity that is used to force the model on the open boundary shown in comparison to the Altamaha discharge from the Doctortown station. . . . .	19
2.7	a) The surface salinity field plot on an ebb tide with velocity vectors shown. b) The surface salinity field plot on a flood tide with velocity vectors shown.	22

2.8	a) The inundation field plot on a slack low tide displaying depth above the surface. b) The inundation field plot on a slack high tide displaying depth above the surface. . . . .	23
2.9	Residual circulation patterns in the middle Duplin plotted on the bathymetry (m). . . . .	24
2.10	Layout for ground water inputs for earlier model runs. Total discharge is $0.1073 \text{ m}^3 \text{ s}^{-1}$ . . . . .	28
2.11	Location of groundwater nodes for latest model runs. Total discharge is $0.6808 \text{ m}^3 \text{ s}^{-1}$ . . . . .	29
2.12	Tidal elevation at GCE10 and a nearby model node. . . . .	31
2.13	A comparison of daily averaged SSH and salinity model output to GCE 10 data. . . . .	32
2.14	Tidal elevation at Marsh Landing and a nearby model node. . . . .	34
2.15	A comparison of daily averaged SSH and salinity model output to Marsh Landing data . . . . .	35
3.1	The starting particle positions for all Lagrangian particle tracking simulations.	39
3.2	Average residence time for all 8 simulations starting on a) a spring tide and b) a neap tide during the HRD period. . . . .	42
3.3	Average residence time for all 8 simulations starting on a) a spring tide and b) a neap tide during the period of LRD. . . . .	44
3.4	Average residence time for all 8 simulations starting on a) slack high tide and b) slack low tide during the HRD period. . . . .	45
3.5	Average residence time for all 8 simulations starting on a) slack high tide and b) slow low tide during the period of LRD. . . . .	47
3.6	Average residence time for all 16 simulations during the a) high river and b) low river discharge period. . . . .	49

4.1	(upper panel) Tidal height versus the tidal component of salinity with red representing spring tides and green representing neap tides. (lower panel) The along channel salinity gradient during September/October 2003 in the upper Duplin. . . . .	55
4.2	A vertical profile of model salinity along the thalweg demonstrating a positive estuary. . . . .	56
4.3	A vertical profile of model salinity along the thalweg demonstrating the negative estuary effect in the mid to upper Duplin, with the locations of the 4 cross sections identified by asterisks. . . . .	57
4.4	The locations of cross sections with inundation at a flood tide. . . . .	61
4.5	The along channel velocity at CS1 during the HRD period on a flood tide. . . . .	63
4.6	The cross sectional salinity at CS1 during the HRD period on a flood tide. . . . .	64
4.7	The residual, exchange, and tidal components of salinity and velocity at cross section 1. . . . .	66
4.8	The residual, exchange, and tidal components of salinity and velocity at cross section 2. Residual area is also shown. . . . .	68
4.9	Residual circulation patterns in the lower Duplin plotted on the bathymetry (m) with cross sections 1 and 2 identified. . . . .	69
4.10	The residual, exchange, and tidal components of salinity and velocity at cross section 3. Residual area is also shown. . . . .	71
4.11	The residual, exchange, and tidal components of salinity and velocity at cross section 4. Residual area is also shown. . . . .	72
4.12	Residual circulation patterns in the upper Duplin plotted on the bathymetry (m) and showing cross sections 3 and 4. . . . .	74
4.13	An example of depth averaged salinity as a function of distance along the thalweg for two different river discharge times. . . . .	75
4.14	Tidal, exchange, residual, and total salt fluxes shown at CS1. . . . .	77

4.15	(upper panel) The sum of exchange and tidal oscillatory flux. (middle panel) The horizontal salinity gradient. (lower panel) The horizontal dispersion coefficient at CS1 with spring tides indicated by a circle and neap tides indicated by an asterisk. . . . .	79
4.16	The tidal, exchange, residual, and total salt flux, respectively at CS2. . . . .	80
4.17	(upper panel) The sum of exchange and tidal oscillatory flux. (middle panel) The horizontal salinity gradient. (lower panel) The horizontal dispersion coefficient at CS2 with spring tides indicated by a circle and neap tides indicated by an asterisk. . . . .	82
4.18	The tidal, exchange, residual, and total salt flux at CS3. . . . .	84
4.19	(upper panel) The sum of exchange and tidal oscillatory flux. (middle panel) The horizontal salinity gradient. (lower panel) The horizontal dispersion coefficient at CS3 with spring tides indicated by a circle and neap tides indicated by an asterisk. . . . .	85
4.20	The tidal, exchange, residual, and total salt flux at CS4. . . . .	87
4.21	(upper panel) The sum of exchange and tidal oscillatory flux. (middle panel) The horizontal salinity gradient. (lower panel) The horizontal dispersion coefficient at CS4 with spring tides indicated by a circle and neap tides indicated by an asterisk. . . . .	89
4.22	Horizontal dispersion coefficients at all cross sections displayed over seasonal scales. . . . .	91

## LIST OF TABLES

2.1	Optimization of Model Stability and Speed . . . . .	25
2.2	Tidal Harmonic Analysis Comparison at GCE10 . . . . .	31
2.3	Tidal Harmonic Analysis Comparison at Marsh Landing . . . . .	34
3.1	Statistical summary of residence time (RT) analysis during a high river discharge period. . . . .	51
3.2	Statistical summary of residence time (RT) analysis during a low river discharge period. . . . .	51

## CHAPTER 1

### INTRODUCTION

#### 1.1 MOTIVATION

The patterns of transport and residence time can have strong effects on water quality within estuaries, as wetlands are known to be natural filters and treatment sites for contaminants or pollutants (*Bodin et al.*, 2013; *Persson et al.*, 1999; *Musner et al.*, 2014; *Savickis et al.*, 2016). Residence time distributions have been shown to control the efficiency of wetlands at contaminant removal (*Savickis et al.*, 2016). The efficiency of a wetland to remove contaminants is driven by the amount of time the contaminants are in contact with the vegetated zone (*Persson et al.*, 1999; *Musner et al.*, 2014). Vegetated zones slow flows and create areas where suspended solids will floc and fall out of the water column and also are the site where biochemical processes will transform the substances (*Musner et al.*, 2014). Residence times and transport therefore are important to describe as they can be crucial when considering the capability of an estuary to remove pollutants and sediments. This utility is a major motivation to create a model capable of describing these important phenomena for scientific and engineering applications.

Salinity and inundation patterns are also two important drivers for state changes within estuarine habitats. Understanding the atmospheric and oceanic forcings that govern variations in inundation and salinity is vital to predicting ecological shifts associated with changing climate and land uses. It is important to predict the salinity, along with inundation patterns, and how these parameters will change temporally and spatially in order to understand long-term changes in ecosystem processes (*DiIorio and Castelao*, 2013). How these parameters change is dependent on the major forcings that govern the salinity gradients and inundation

within estuarine systems. Tidal forcing, offshore sea surface height (SSH), and freshwater inputs are the major drivers that can control salinity and inundation in coastal salt marsh estuaries.

Tides are one of the most important forcings in estuarine systems. Tidal mixing is strong and can dominate at times, especially on spring tides, for estuaries in the southeast. Also, ebb dominated estuaries have longer, slower rising tides and stronger, shorter ebb currents that are typical on the Georgia coast where deep channels, extensive mud flats and marsh regions dominate. The high characteristic shear on ebb leads to very well mixed conditions (*McKay and DiIorio, 2010*). The spring/neap modulation of along channel velocity and tidal height is also very apparent on the Georgia coast. Previous measurements in the Altamaha River (*DiIorio and Kang, 2007*) and in the Duplin River (*McKay and DiIorio, 2010*) on the Georgia coast have shown along channel velocities as high as  $1.2 \text{ m s}^{-1}$  on the spring ebb tide with corresponding neap ebb flows with values half that magnitude. Maximum tidal heights ranging from  $1 \text{ m}$  to  $2.6 \text{ m}$  on neap and spring tides, respectively were also observed.

Offshore SSH forcing is an important driver of inundation along the Georgia coast. Winds can strongly modulate SSH on sub-tidal timescales in estuarine systems (*DiIorio and Castelao, 2013*). As wind forcing on the coast of Georgia varies seasonally, SSH due to winds also varies on seasonal time scales (*Weber and Blanton, 1980*). *DiIorio and Castelao (2013)* found that sub-tidal SSH was positively correlated with alongshore winds and negatively correlated with cross-shore winds and can vary up to  $0.6 \text{ m}$  within the Georgia coast. Inundation generally increases in the fall and winter when the prevailing northeasterly winds cause downwelling conditions and decreases in the spring and summer when winds dominate from the southwest and promote upwelling conditions or offshore transport (*DiIorio and Castelao, 2013*). The fact that winds can cause such large variations in SSH shows that it is important to capture this phenomenon if the goal is to accurately simulate inundation.

Freshwater inputs are another major driver of estuarine dynamics. River discharge can be one of the major drivers of exchange within complicated estuarine systems (*Traynum and*

*Styles*, 2008). Estuarine circulation is a well studied phenomenon even though the major drivers are not completely understood. In the classical definition of estuarine circulation, the salinity gradient leads to an up-estuary baroclinic pressure gradient that becomes greater from the surface layer to the bottom layer. There is also a down estuary barotropic pressure gradient. This force is constant in the vertical direction. Together, these forces lead to inflows of salty water on the bottom and outflows of fresher water at the surface (*Schulz et al.*, 2015). This is the classical estuarine circulation. River discharge is the major contributor to freshwater on the Georgia coast and the formation of the coastal frontal zone within the inner shelf (*Blanton and Atkinson*, 1983). Groundwater can also be a source of freshwater to estuaries on the Atlantic coast (*Porubsky et al.*, 2011). Its contribution to salinity is not well known, but it can have significant effects on nutrients and biogeochemical processes in estuaries.

In order to understand biogeochemistry in estuarine systems, it is important to first understand the fates of water masses that are dependent on the dynamics of the system. Understanding the patterns of nutrient delivery is very important in order to quantify anthropogenic effects on ecosystems and the governing biogeochemical cycles (*Porubsky et al.*, 2011). Changes in inundation patterns and residence times, or the intensity of flushing, which is dependent on spring/neap cycles, semi-diurnal tidal cycles, and seasonal forcings can have powerful effects on the magnitude of nutrients exported into estuarine systems (*Porubsky et al.*, 2011; *Snyder et al.*, 2004). The strength of the salinity gradient and the level of inundation can affect the chemical speciation of nutrients by altering the composition of the water masses at the boundary of the tidal range and thus can affect the type and amount of nutrients added to estuaries (*Snyder et al.*, 2004; *Porubsky et al.*, 2011). Due to these facts, it is important to quantify inundation patterns and residence times in order to investigate biogeochemistry with estuarine systems.

Understanding the patterns of mixing and transport within estuaries and the physical forcings that govern these patterns is extremely important. In order to understand the trends

of salinity, the factors that drive salt fluxes must be explored. All estuaries are unique and salt fluxes depend on the physical characteristics of the estuary, such as bathymetry, along with the magnitude of the physical forcings, such as tides and freshwater inputs. A model can be a useful tool to investigate the patterns of transport under specific forcing scenarios (*Devkota and Fang, 2015*). This is mainly due to the fact that many of these physical measurements are time consuming and difficult to obtain, especially when trying to capture spatial and temporal variability.

## 1.2 SITE DESCRIPTION

The Georgia Coastal Ecosystems Long Term Ecological Research (GCE LTER <https://gce-lter.marsci.uga.edu>) domain is the governing site for the research carried out in this thesis. The GCE domain is a complicated system of tidal creeks, back barrier islands, forested upland areas, and receives much of its freshwater from the Altamaha River. This river is Georgia's largest river and its watershed extends to Athens and south of Atlanta. The entire GCE domain can be seen in infrared in Figure 1.1, which illustrates this variable and complex system. Long term monitoring stations within the GCE domain (GCE1 through GCE10) collect hydrographic data of salinity, temperature, and water depth, which has been catalogued over the past 15 years. The USGS Doortown gauge is where volumetric flow rates are measured for the Altamaha River. The Altamaha River is the primary mode for salinity variation throughout the GCE domain and affects the latitudinal and longitudinal gradients of salinity within the estuaries (*DiIorio and Castelao, 2013*). It has been established that advection of river inputs along with groundwater flows are two of the major contributors to the salinity gradient (*Kjerfve, 1973; Ragotzkie and Bryson, 1955*). Freshwater can make its way north to Doboy and Sapelo Sounds through the complex connections of tidal creeks, marsh, and Intracoastal waterway.

The Duplin River, the polygon highlighted in yellow in Figure 1.1, is the site of the current research and is a large elongated bay located on Sapelo Island within the GCE LTER

project site. The Duplin River is an ideal site because it is a good proxy for the entire GCE LTER site, in which the Duplin is located, and it has been studied extensively over a long period of time (*Ragotzkie and Bryson, 1955; Kjerfve, 1973; Snyder et al., 2004; Porubsky et al., 2011; McKay and DiIorio, 2008, 2010*). The salt and heat budgets for the Duplin have been quantified in earlier studies showing that tidal mixing and transport dominate the variability (*McKay and DiIorio, 2008, 2010*). The patterns of freshwater inputs have also been explored, but more research is necessary to determine the major drivers of the dynamics (*Kjerfve, 1973*). Groundwater was determined to be an important contributor of freshwater to the domain (*Schultz and Ruppel, 2002; Porubsky et al., 2011; Ragotzkie and Bryson, 1955*). Salinity variation within the Duplin River is heavily influenced by tidal cycles in conjunction with fresh and salt water inputs from Doboy sound at the mouth, which takes into account riverine discharge effects from the Altamaha (*Kjerfve, 1973*).

A close up infrared satellite image of the Duplin River watershed, with the model domain highlighted in yellow, can be seen in Figure 1.2. This image shows a tidal river surrounded by salt marsh and the Sapelo barrier island to the east. Tall *Spartina alterniflora* dominates the marsh in the low marsh zone and medium *Spartina alterniflora* dominates in the mid marsh zone. The high marsh is made up of a mixed community of vegetation including short *Spartina alterniflora*. Tall *Spartina alterniflora* dominates where tidal inundation is very regular (low marsh zone) and short *Spartina alterniflora* dominates where inundation is very irregular (high marsh zone) (*Hladik et al., 2013; Hladik and Alber, 2014*).

There are long term monitoring stations within and nearby the Duplin that collect real time data that can be used for comparisons to model predicted values, and is used as input for the model. The long term monitoring site used for model forcings is from GCE6 and data used for model comparisons are from Marsh Landing (ML), where a partnership with the Sapelo Island National Estuarine Research Reserve maintains a water quality and atmospheric weather station, and GCE10.

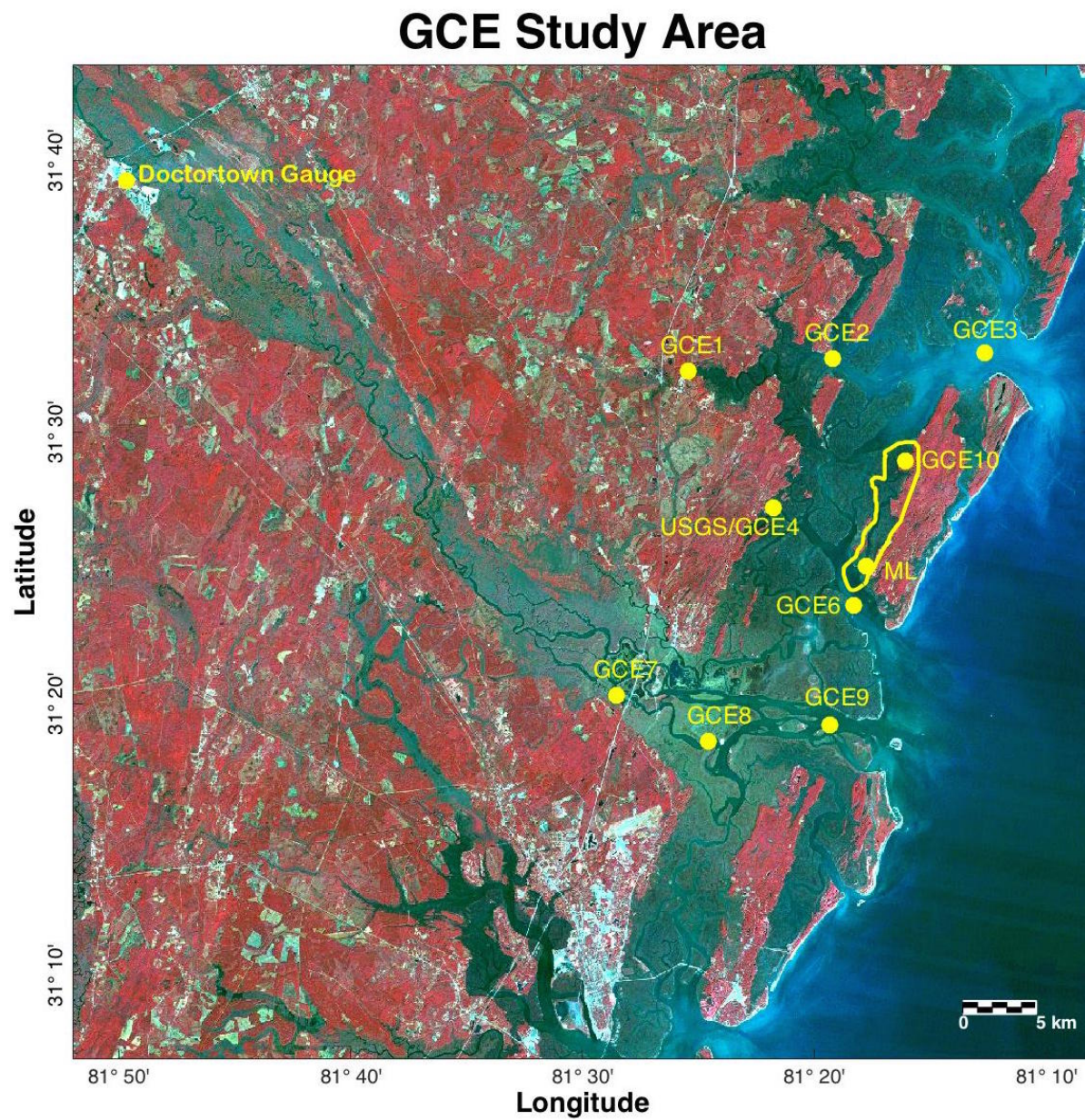


Figure 1.1: An infrared satellite view of the GCE domain together with long term monitoring stations. The Duplin River model domain is outlined in yellow on Sapelo Island, Georgia.

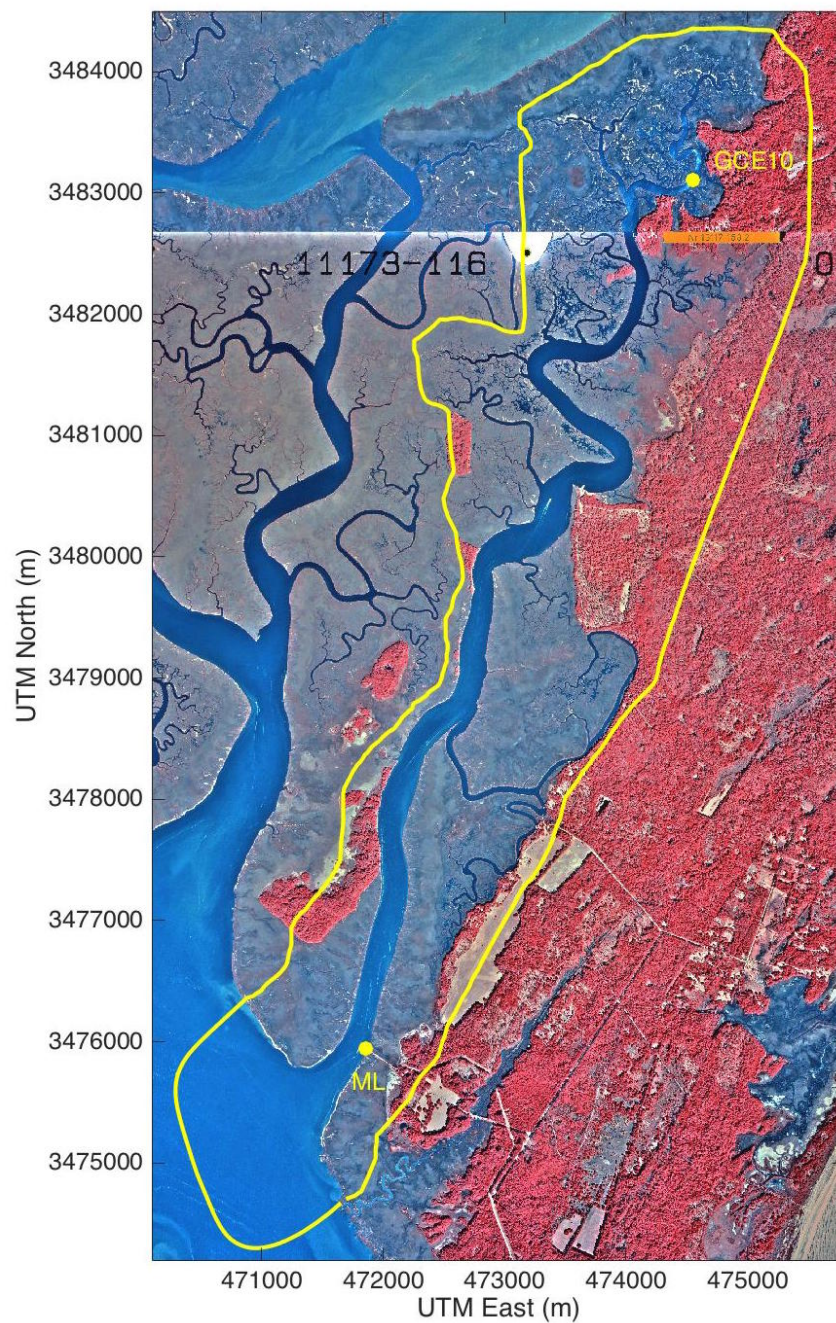


Figure 1.2: An infrared satellite view of the Duplin domain together with long term monitoring sites at Marsh Landing (ML) and GCE 10. The Duplin model domain is outlined in yellow.

### 1.3 OBJECTIVES

The major research objectives of this Master's thesis are as follows:

1. To create a high resolution three dimensional hydrodynamic model of the Duplin River estuary on Sapelo Island using the Finite Volume Community Ocean Model (FVCOM).
2. To model salinity and inundation patterns for the Duplin, obtaining good comparisons of model predicted values with time series data taken from the long term monitoring stations within the system.
3. To use this model to quantify horizontal transport and determine residence times using Eulerian decomposition salt flux analysis and the Lagrangian particle tracking module, respectively, for the Duplin River.

### 1.4 THESIS OUTLINE

Chapter 2 is a summary of the experimental approach taken over the breadth of this research. This includes a description of the high resolution digital elevation model (DEM) created for the Duplin River. The process used to create the high resolution mesh and to improve this mesh are also described in detail. This chapter also includes a description of all of the major forcings incorporated into the model. The modeling software and computational resources used are also described. A discussion of the sensitivity testing that was carried out will be discussed as well. This includes a discussion of optimizing speed with stability, variation of mixing parameters, as well as the variation of the groundwater forcing. The last section in this chapter will discuss model/data comparisons at stations within the domain as well as using a tidal harmonic analysis to compare to the model.

Chapter 3 discusses results from the Lagrangian particle tracking module within the model. The spring/neap, seasonal, and semidiurnal tidal effects on residence times will also be addressed within this section.

Chapter 4 will discuss the Eulerian decomposition used to quantify salt transport and horizontal dispersion within the model domain. This chapter includes a description of the major flux components that contribute to horizontal transport within the system and how these components vary seasonally and on spring/neap time scales. This chapter also includes the quantification and discussion of how the horizontal dispersion coefficient can vary temporally and spatially.

Chapter 5 will summarize all significant findings and make recommendations for future directions and studies to continue this research.

## CHAPTER 2

### METHODS AND MODEL DESCRIPTION

#### 2.1 HIGH RESOLUTION DIGITAL ELEVATION MODEL

Initially, a digital elevation model (DEM) was created from merging light detection and ranging (LiDAR) data, which provides the surface elevation, with multibeam acoustic swath bathymetry mapping carried out by collaborators (R. Viso and R. Peterson) from Coastal Carolina University. *Hladik et al.* (2013) found that LiDAR data errors varied depending on the amount of vegetation cover and that LiDAR was more error prone in areas of dense vegetation. Due to this, the authors developed and applied correction factors for specific vegetation classes and the LiDAR elevation data was corrected using this approach. With the corrected LiDAR and merged swath data the DEM still had many areas where data was missing. The areas of missing data led to instabilities within model runs. This was due to these areas being misrepresented by the depths within the DEM through interpolating over areas without data. Figure 2.1 displays the original DEM (merged, corrected LiDAR with swath data) where white areas represent no data.

Due to instability problems created from these gaps in the data, it was decided that these areas needed to be filled in. A high resolution echo sounder together with a real time kinematics (RTK) GPS unit was mounted on a small canoe with a small outboard motor in order to be able to access the narrow, shallow creeks. The survey setup is shown in Figure 2.2 along with a picture of a curious alligator, the project mascot. On numerous dates, areas of missing data were surveyed by traversing the creeks and channels using a “mowing the lawn” survey technique. Multiple passes were made over the areas to better represent the actual bathymetry and to have a better range for data interpolation. A Hydrobox data acquisition

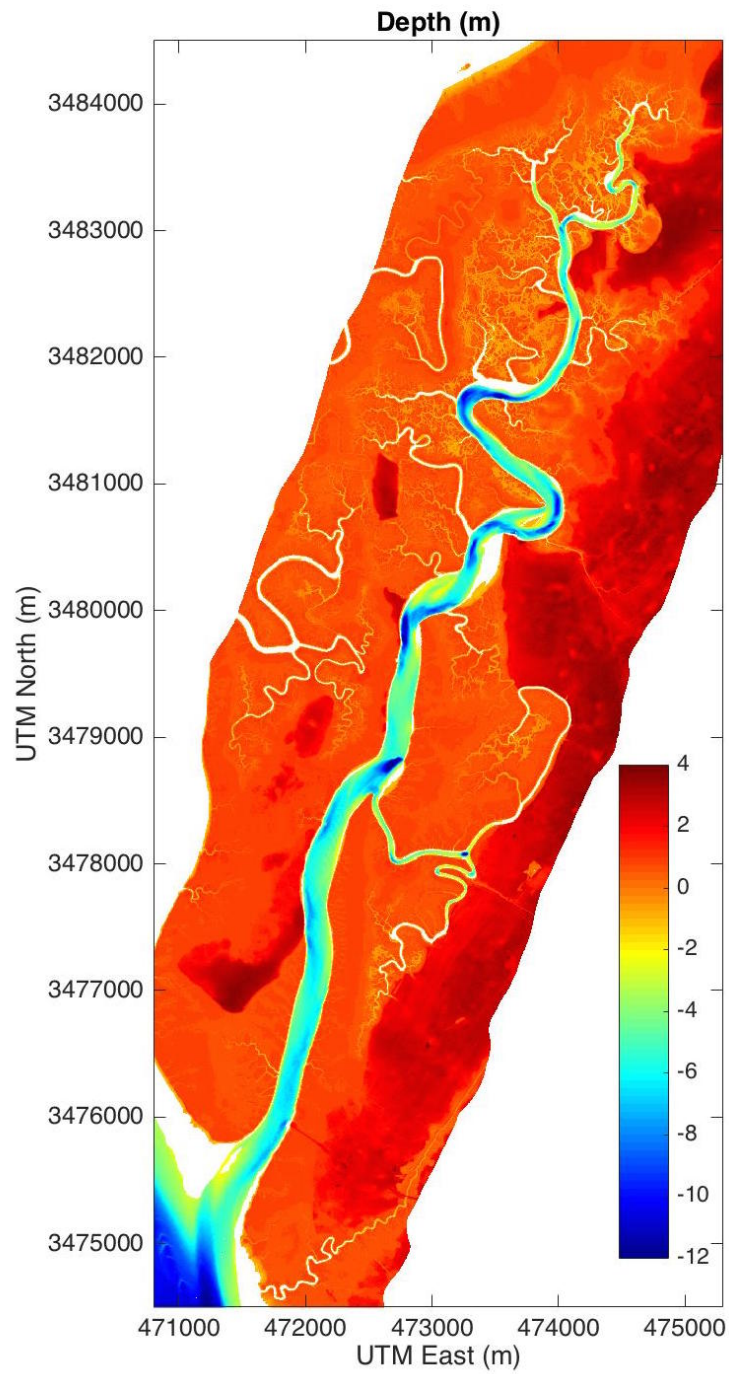


Figure 2.1: The original bathymetry map with merged, corrected LIDAR and swath bathymetry referenced to mean sea level (MSL in m).

system connected the echo sounder to the laptop. The new echo sounding bathymetry data was then merged with the existing data set after each sampling trip until the bathymetry map was deemed acceptable for our modeling purposes.

Over the course of the project, most of the major creeks and channel edges were filled in using this method. This new data was merged to the DEM and is represented by depth (in yellow) but highly exaggerated in size in order to show the survey locations in Figure 2.3. The final corrected, merged, and interpolated 1 *m* DEM was then averaged to create a 4 *m* high resolution DEM.

## 2.2 MESHING PROCESS

The model mesh was created using Surface-water Modeling System (SMS), which is a software from Aquaveo (<http://www.aquaveo.com>). A model boundary was first developed using Google Earth to trace out the outer edges of the Duplin watershed and then the Google Earth kml data points were converted to a ascii file type that could be read in SMS. The zero meter contour line was then found to create a polygon of the Duplin main channel which was within the larger polygon representing the entire watershed boundary. Both these polygons were smoothed so that the nodes were evenly spaced depending on the characteristics of the domain: the open boundary nodes at the mouth of the Duplin were spaced at 30 *m* apart, the outer boundary nodes were also spaced at approximately 30 *m* apart, the nodes along the main channel of the Duplin were spaced at approximately 15 *m* apart, the nodes along the smaller side channels were spaced at approximately 5-10 *m* apart depending on the size of the channel. The mesh was then generated for the domain using SMS and the final mesh is such that the triangular elements follow the channel edges (see Figure 2.4 in a sinuous section of the Duplin).

The mesh was edited to meet FVCOM standards: allowable angles within triangles must be greater than 30 degrees and less than 130 degrees, area changes from triangle to triangle cannot change by more than 50 percent from element to element, and the maximum allowable



a)



b)

Figure 2.2: a) The field work mascot. b) The canoe setup with a RTK GPS and echo sounder attached.

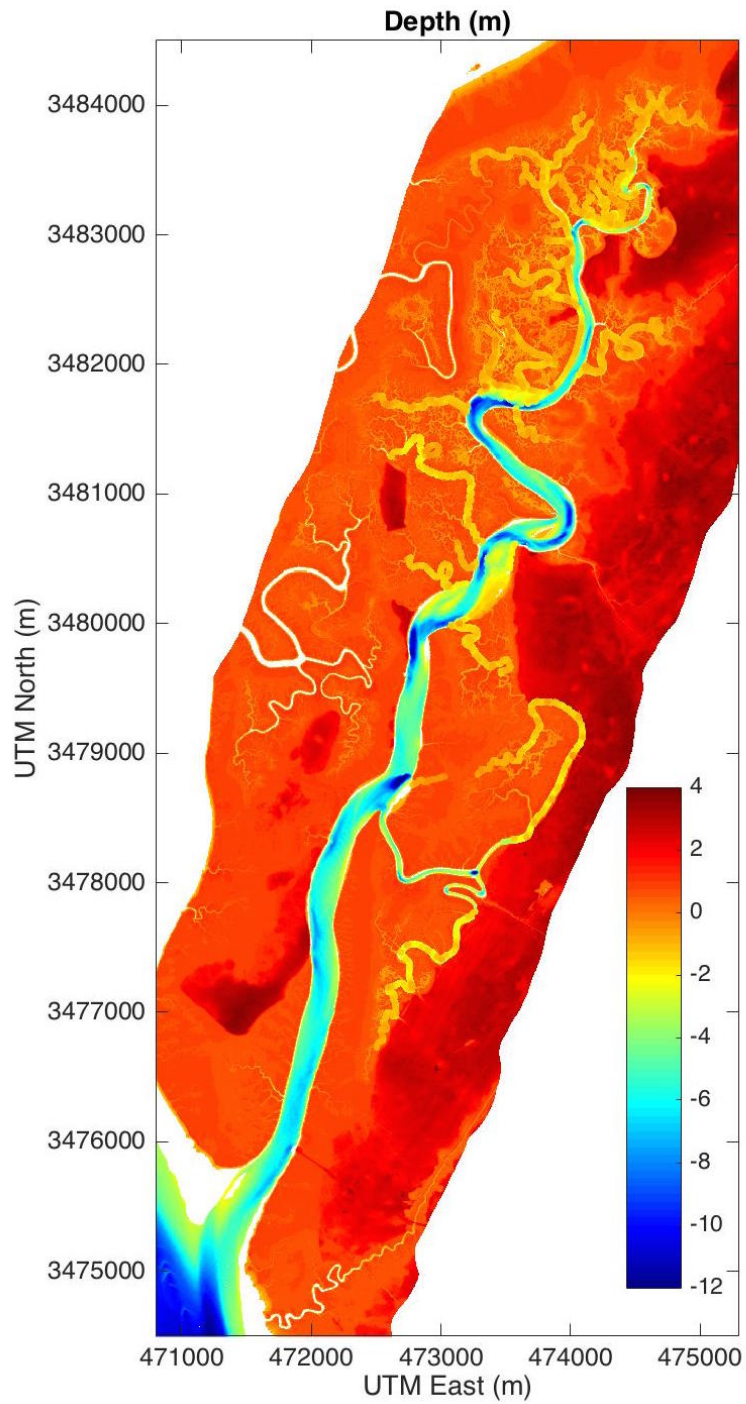


Figure 2.3: High resolution echo sounding depths in yellow and exaggerated in size are superimposed on merged, corrected LIDAR and swath data (referenced to MSL).

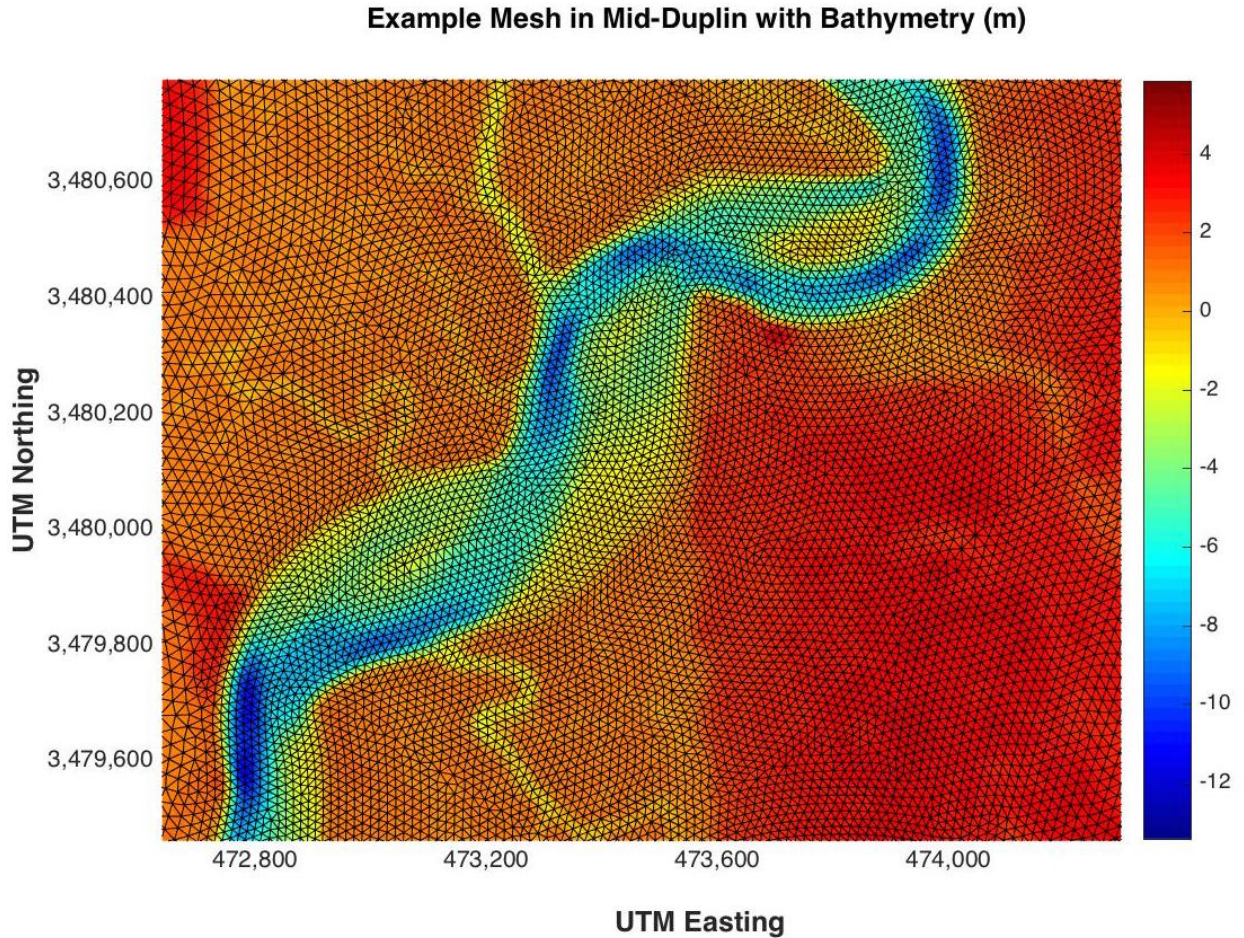


Figure 2.4: A close up example of the mesh in the mid-Duplin.

elements connected to a node cannot exceed 8. The final mesh contains 77,032 nodes and 153,247 elements. After successfully generating a mesh, the high resolution 4 *m* bathymetry data, described in the previous section, was interpolated to the mesh nodes using SMS and smoothed using the smoothfield function provided with the FVCOM source code to remove large depth gradients and discontinuities in the bathymetry associated with the vegetation correction factors applied to the LiDAR data (see Figure 2.5).

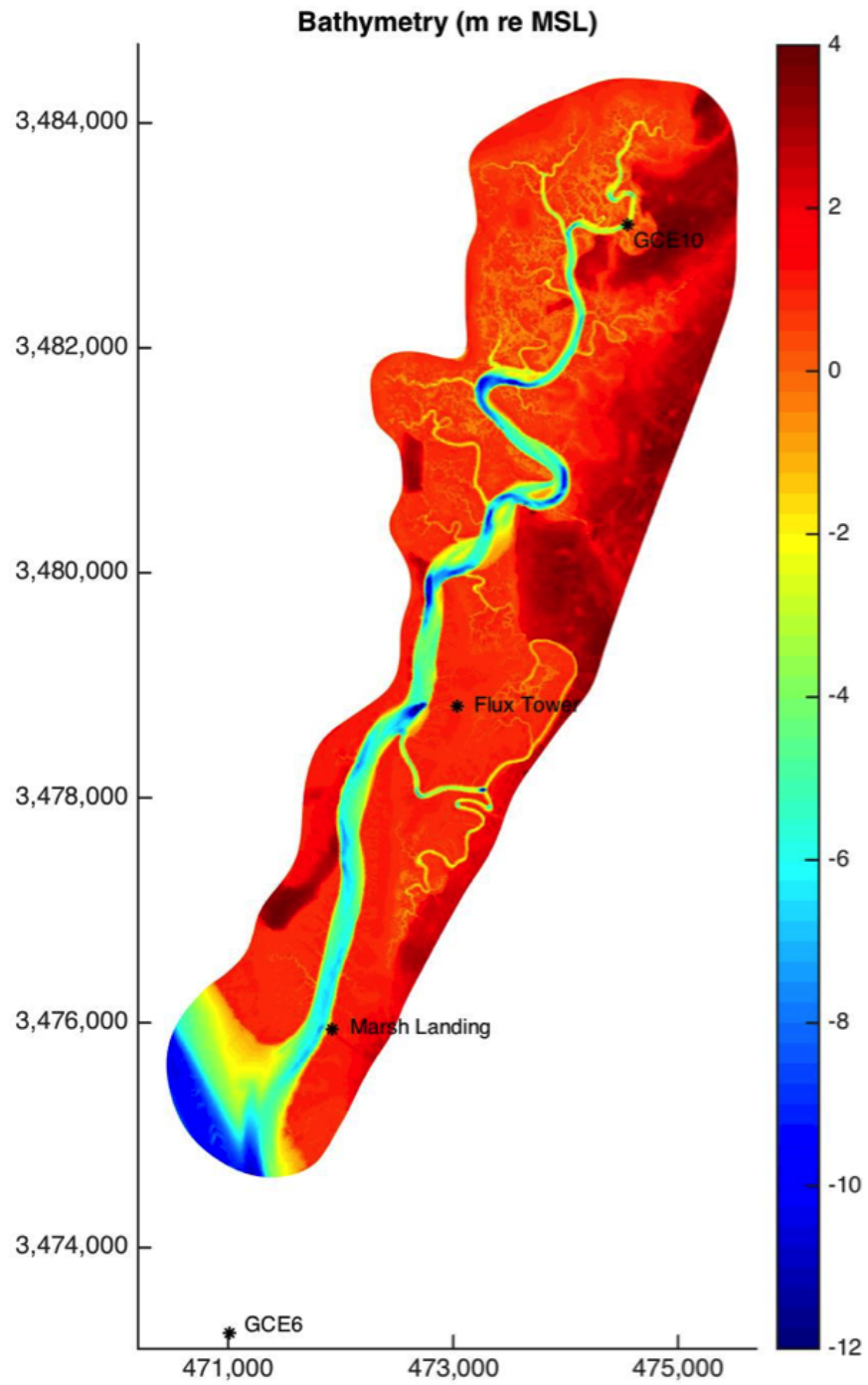


Figure 2.5: The 4 m digital elevation model (DEM) interpolated to the model mesh with monitoring stations identified.

### 2.3 MESH QUALITY

Troubleshooting the mesh to deal with mesh quality issues is accomplished by running the model and generating output variables quickly, every 10 seconds or at smaller time increments. When the model went unstable, the output is transferred into MATLAB. Using scripts written for these specific purposes, the elements where velocities went unstable would then be identified. The mesh was then edited to correct mesh elements and this process was repeated until no further instabilities were found. This method was also used to identify areas where bathymetry data needed to be filled in by using the echo sounding methods described in the previous section, or corrected by smoothing using the `smooth_field` MATLAB program provided with the FVCOM source code. Using this approach, the quality of the mesh was improved until the model could run to completion with a refined time step. There was a total of 70 meshes developed before the final mesh was deemed complete.

### 2.4 DESCRIPTION OF MODEL FORCINGS

Tides are a dominant forcing for estuaries. Of particular importance is how the spring/neap cycle determines exchange and mixing between the upper and lower Duplin. The GCE6 station in Doboy Sound, close to the mouth of the Duplin, is used to input real sea surface height measurements into the model and hence input realistic tides (see Figure 2.6 upper panel). One major goal is to model the effect of the spring/neap cycle on the salinity and inundation patterns within the domain.

The effect of offshore wind forcing on SSH can be included in the model by forcing the open boundary with the hourly time series of SSH from GCE6 within Doboy sound since this data also includes the subtidal effects. By using a real time series of SSH, as opposed to forcing with just tidal constituents, inundation effects by offshore wind forcing can be incorporated into the model. As it is well documented that offshore winds can have strong

effects on SSH (see *DiIorio and Castelao (2013)*), it is important to include these effects in the model inputs if the goal is to accurately predict inundation.

Forcing the model with hourly times series of sea surface height is one way to ensure that the model is capable of handling a large range of tidal forcings. For the year 2014, the tidal height range varies from -1.7 to 1.6 *m* for a total range of 3.3 *m* on spring tides. Thus the model is capable handling any tidal forcing within this range without leading to instabilities and is also capable of handling subtidal changes caused by offshore wind forcings for the year 2014.

The meteorological diurnal, semidiurnal, and seasonal heat input is accounted for by forcing the model with real time hourly temperature data from GCE6. By using a hourly time series taken from the GCE6 station within Doboy sound, the model can account for large temperature variations within the model domain. Refer to Figure 2.6 for a visualization of the temperature forcing on the model open boundary for the year 2014. The model can handle temperatures ranging from 8 to 30 °C.

Freshwater is incorporated into the model through two major mechanisms. The major drivers of freshwater in this system are groundwater inputs along with pulses of freshwater effluent from Doboy Sound at the mouth of the Duplin. This effluent from Doboy has salinities that are modulated by freshwater from the Altamaha River. The time series salinity data for the Year 2014 used to force the model at the open boundary can be seen in Figure 2.6. An example of volumetric flow from the Altamaha, measured at the Doctortown station can also be seen in Figure 2.6. Note that when the river discharge is high, salinities are reduced with an approximate time delay of 7-14 days. The salinity variability is also controlled by the tidal patterns of the domain. The model can handle a large range of salinity, and during the year 2014, the salinity from GCE6 ranges from 10 to 35 PSU.

The other major driver of the salinity variability may be attributed to groundwater input along with surface flow from precipitation. Groundwater input has been shown and accepted to be a major contributor of freshwater in the domain (*Ragotzkie and Bryson, 1955; McKay*

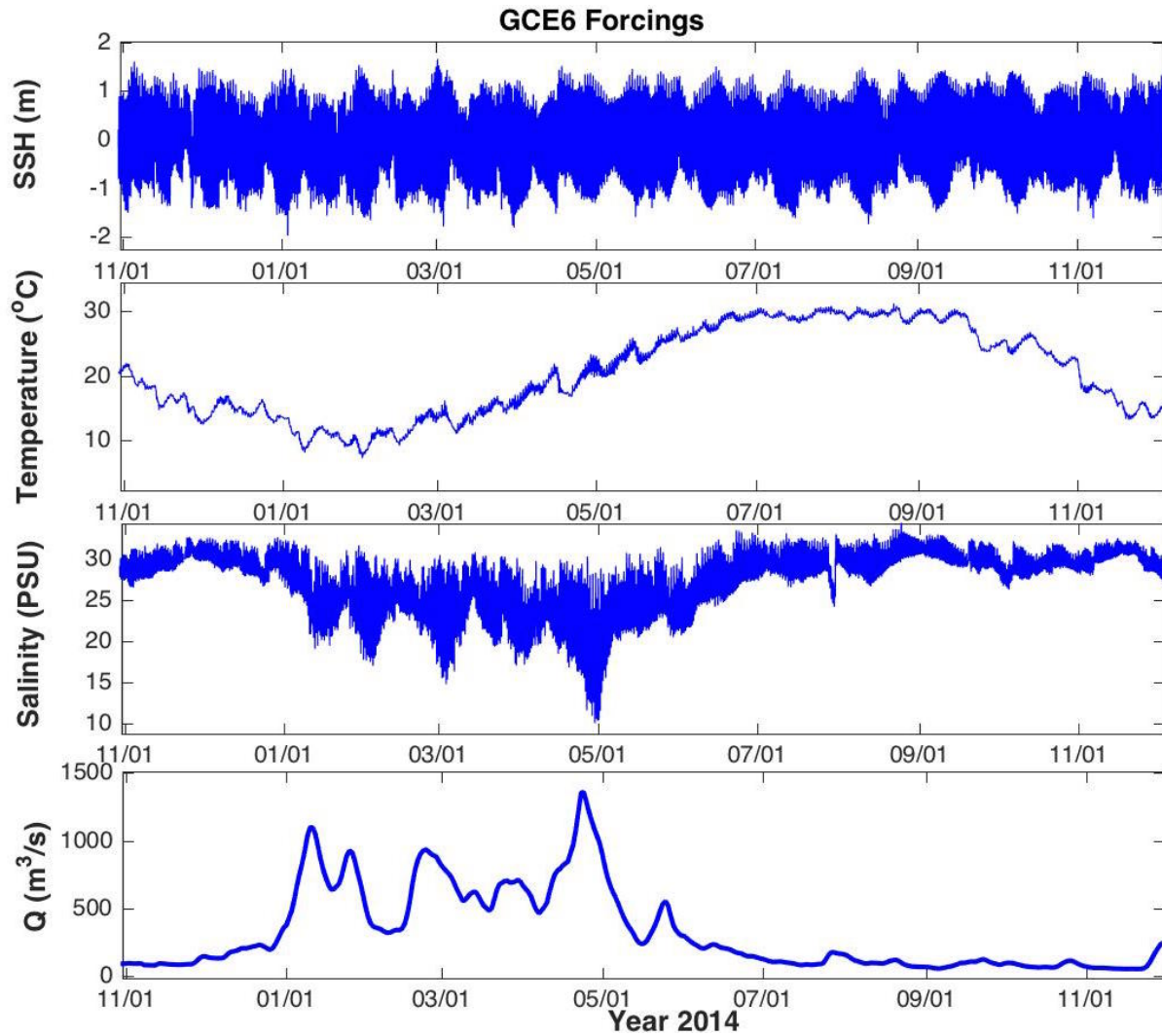


Figure 2.6: GCE6 sea surface height, temperature, and salinity that is used to force the model on the open boundary shown in comparison to the Altamaha discharge from the Doctortown station.

and DiIorio, 2010; Porubsky et al., 2011). It is important to be able to predict groundwater inputs because groundwater acts as a source of nutrients and is integral to the exchange of geochemical materials between the tidal prism and the salt marsh (Carter et al., 2008; Porubsky et al., 2011; Schultz and Ruppel, 2002). Based on studies of groundwater in the upper Duplin, the amount of groundwater is expected to vary spatially and temporally (Schultz and Ruppel, 2002).

Hourly SSH, temperature, and salinity were forced at the open boundary to capture tidal and subtidal variability, diurnal and seasonal patterns of heat energy, and the effects of freshwater from the Altamaha river on salinity. These inputs were created by using existing Matlab scripts from the FVCOM Matlab toolbox (<https://github.com/GeoffCowles/fvcom-toolbox>) in conjunction with custom scripts written to create these inputs using the proper format for FVCOM. Using only these components to force the model is the simplest approach possible to accomplish the goals of this research.

## 2.5 FVCOM3.2.2

The model has been transitioned to run the latest version of FVCOM (3.2.2), in order to make use of the improved groundwater module. FVCOM uses a finite volume scheme to solve integral versions of the momentum, salt, temperature, continuity, and density equations. The benefits of using a finite-volume scheme is that it combines the geometric flexibility of the finite-element method with computational efficiency and simple discretization techniques of the finite-difference method (Chen and Liu, 2003). This version of FVCOM has very similar architecture to FVCOM 2.7.1, that was initially used, but has a more robust groundwater module. As groundwater is a component of freshwater input into the study system, this version of FVCOM was necessary to test its relative importance and the effects on the salinity distribution. For a description of the model and governing equations, refer to Chen and Liu (2003).

The model has been run using the 3-D baroclinic mode with the wetting and drying mode activated with a 5 *cm* minimum depth. The Mellor-Yamada 2.5 turbulence closure model was used for all model runs (*Mellor and Yamada, 1982*). The Lagrangian particle tracking module has also been activated for model runs where needed (*Chen et al., 2013*). Currently, the highest external time step that can be used without the model becoming unstable is 0.2 seconds. This is with 5 sigma layers, and an *Isplit=2* (*Chen et al., 2013*). The *Isplit* is the ratio of the internal time step to the external time step. The initial conditions for the model run is a salinity of 5 PSU and a temperature of 15 °C. Year 2014 has been the major emphasis of the modeling efforts as this is considered to be an average year in terms of freshwater input for the Altamaha river to the GCE domain and because there was extensive biogeochemical sampling that took place during this time period, which led to an interest in transport processes during this time from collaborators on the GCE project (*Wang, 2016a*). The model was started on November 1, 2013 and was allowed to ramp up over a 2 month period.

The major output from the model used for analysis is salinity, SSH, and velocity data. Figures 2.7 and 2.8 are an example of these outputs for the Duplin domain. Figure 2.7 displays surface salinity data with surface velocity vectors on an ebb and flood tide. The water is fresher at the mouth during the flood compared to the ebb tide showing that fresher water is being tidally advected into the Duplin at this time. Figure 2.8 shows inundation throughout the entire domain on a slack low and slack high tide, respectively. Inundation here refers to how much water is above the bottom. The marsh and mudflats are considerably more inundated on the high tide as expected and inundation can reach the outer boundary to the north and the west side. Figure 2.9 shows the depth averaged, tidally filtered velocity at the centroids of every tenth mesh element. This was taken during the month of September and shows the major patterns of circulation within the mid Duplin domain. The vectors are scaled to  $0.1 \text{ m s}^{-1}$ , which is shown in the plot. Eddies can be seen concentrated over deep holes within the domain and show that this model can be used to understand morphological

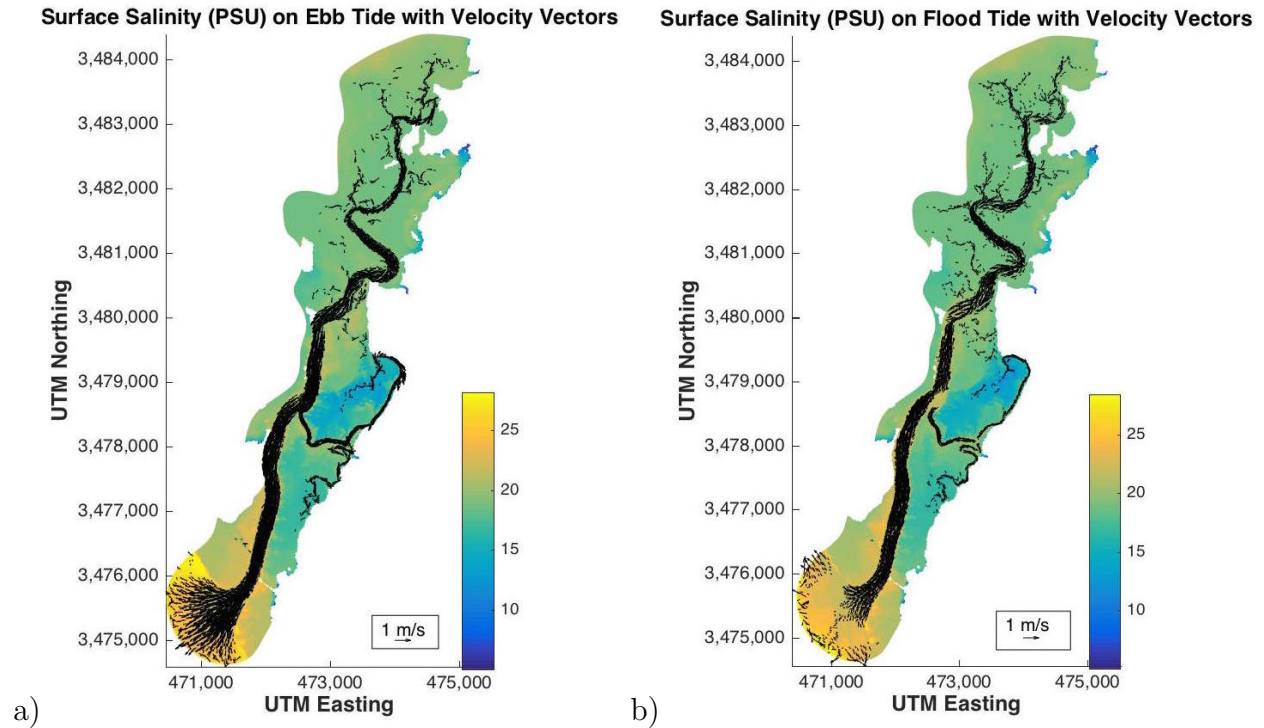


Figure 2.7: a) The surface salinity field plot on an ebb tide with velocity vectors shown. b) The surface salinity field plot on a flood tide with velocity vectors shown.

features of deep holes and shallow bars and their formation (a topic which is beyond the scope of this thesis).

## 2.6 COMPUTATIONAL RESOURCES

Throughout the course of this research, three different computational systems were used. Initially, the z-cluster, which is University of Georgia's advanced computer campus resource was used to run FVCOM 2.7.1, the first version of the model to be used. Next, a 32 core tower bought for the lab was used to run the model to test for stability since there was no queueing system. Ultimately, due to time constraints with the previous resources, Sapelo, which is University of Georgia's newest and most powerful computational resource was used to compile and run the model. Sapelo is a Linux cluster using a 64-bit CentOS 6.5 operating

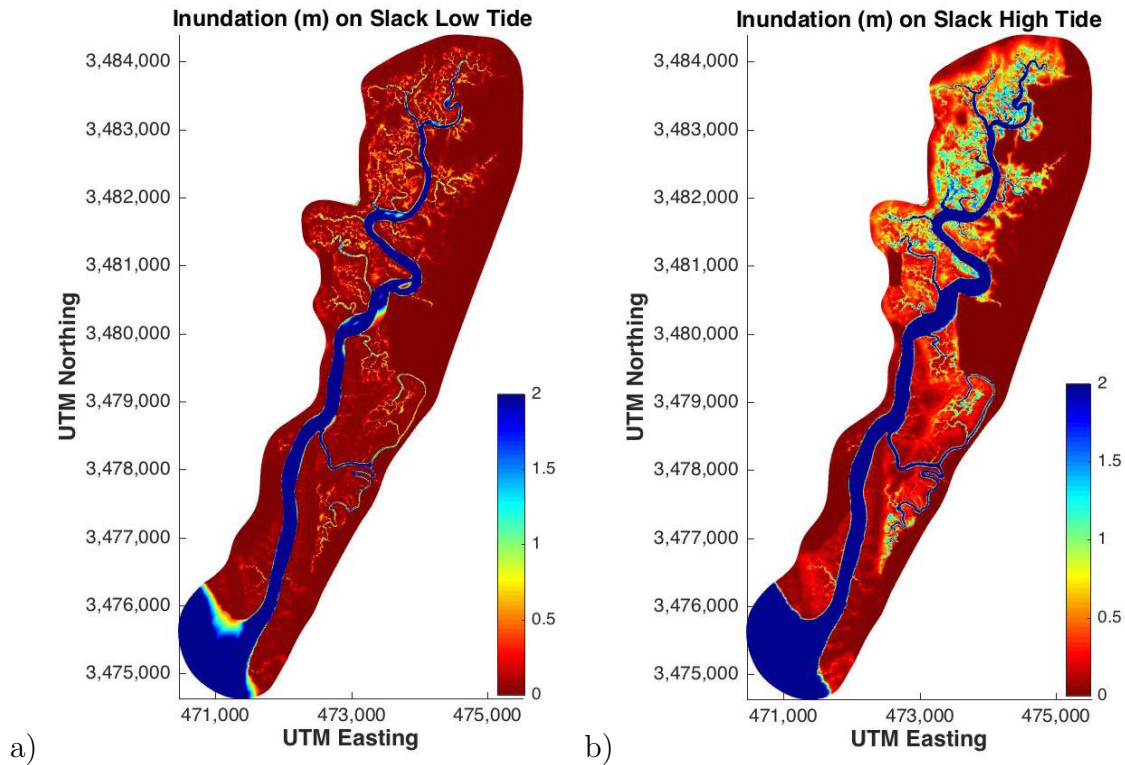


Figure 2.8: a) The inundation field plot on a slack low tide displaying depth above the surface. b) The inundation field plot on a slack high tide displaying depth above the surface.

system. The login nodes use Intel Xeon processors. There are 112 compute nodes that have AMD 48 core Opteron processors with 128 GB of RAM on each node (<http://gacrc.uga.edu>). Eight nodes were used to run the model as will be described. The newest addition to this computational arrangement was a clustering of 21 nodes purchased by 9 UGA faculty. This subcluster is referred to as Aquarinode.

## 2.7 MODEL SENSITIVITY

### 2.7.1 OPTIMIZING MODEL SPEED WITH STABILITY

Originally, the approach to running the model was that more computing nodes (and hence speed) was better. After discussions with colleagues at the FVCOM users meeting in Hal-

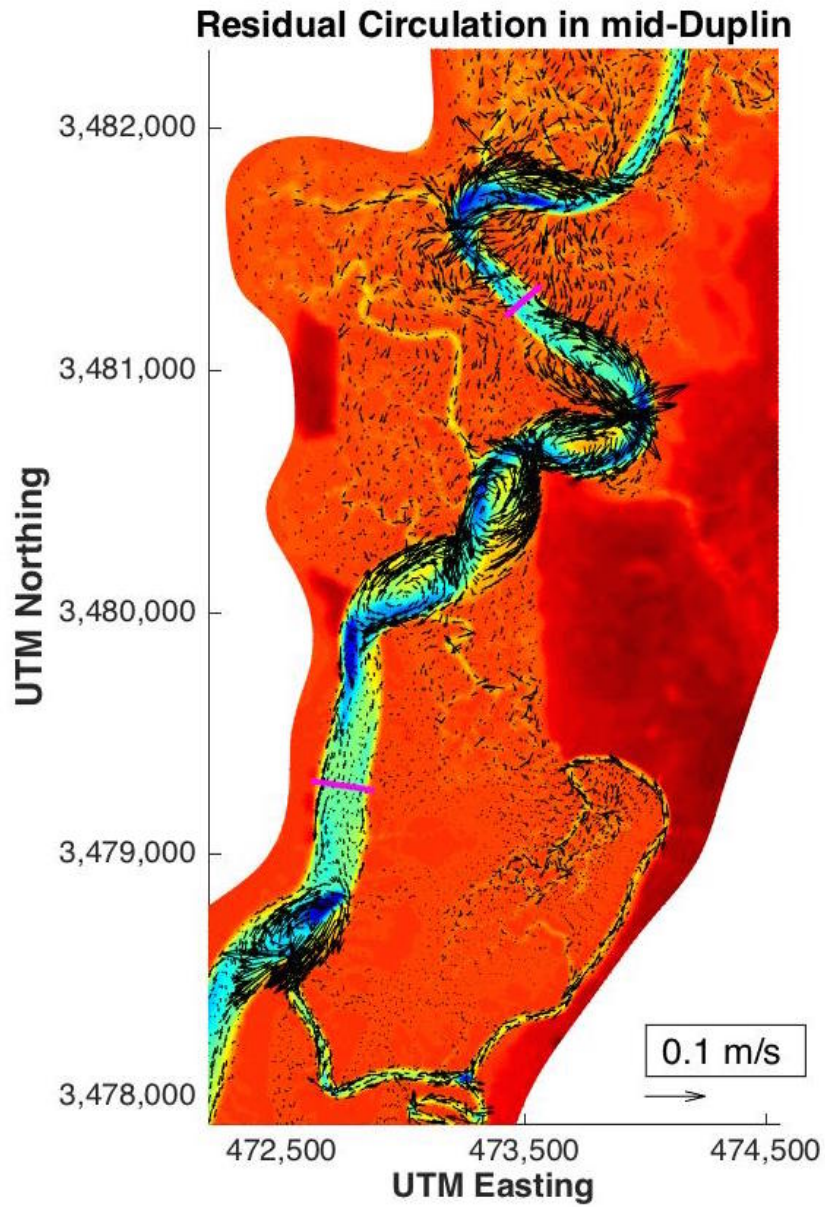


Figure 2.9: Residual circulation patterns in the middle Duplin plotted on the bathymetry (m).

ifax, Nova Scotia in October 2015 (<http://fvcom.smast.umassd.edu/2015/09/03/2015-fvcom-users-workshop/>), it was determined that the model needed to be optimized in terms of speed, number of computing nodes, and stability. This was due to the phenomenon of error propagation through message passing between nodes. Using the Sapelo advanced computer resource, the model was tested on different numbers of nodes ranging from a single node to the maximum allowed 10 nodes for the system. Stability is quantified as the number of days the model runs before instability causes the model to crash. Speed was quantified as the ratio of how far the model progressed before instability to the total run time. Speed can vary slightly from model run to model run depending on the strain on the computer cluster due to use at run time. Replicates of the 144, 240, and 384 core runs were done to ensure that stability and speed were relatively constant from run to run. Stability was rounded to the nearest day. These runs were completed using an external time step of 0.5 seconds with an Isplit of 1. Refer to Table 2.1 for a summary.

From these model runs, it was determined that 384 cores was the ideal setup to run our model. By reducing the external timestep to 0.2 seconds and changing the Isplit to 2, which

Table 2.1: Optimization of Model Stability and Speed

Number of Cores	Stability (Days)	Speed(Ratio)
48	49 Days	12
96	49 Days	21
144	108 Days	30
192	49 Days	40
240	108 Days	46
288	108 Days	48
336	62 Days	55
384	151 Days	56
432	62 Days	60
480	108 Days	67

changes the internal timestep from 0.5 to 0.4 seconds, model stability was achieved for the entirety of the run spanning November 2013 to December 2014.

### 2.7.2 VARIATIONS OF HORIZONTAL MIXING PARAMETERS

The horizontal mixing coefficient used in the Smagorinsky method to calculate horizontal diffusion was varied over a large range to test for sensitivity and to optimize our model stability. For a description of this method, see *Smagorinsky (1963)*. It was found through many model tests that the model was most stable using a Smagorinsky horizontal mixing coefficient of 0.18. Runs using mixing coefficients of 0.02, 0.04, 0.1, 0.15, 0.17, 0.19, 0.2, 0.3, 1.0, and 2.0 were all carried out. The runs starting with 0.02 and increasing to 0.17 all went unstable very quickly, within 30 days of model run time. The larger values (1.0 and 2.0) also became unstable very quickly. It was decided that among the stable runs, 0.18 was the best in order to improve the salinity output in the upper Duplin at GCE10. The horizontal Prandtl number, which is a dimensionless ratio of the diffusivity of momentum to thermal diffusivity, was also varied from 0.1, 1, and 3. Due to stability issues, 1 was chosen as the best horizontal Prandtl number.

### 2.7.3 VARIATIONS OF GROUND WATER INPUTS

Many different model runs were carried out with varying inputs of the groundwater. Originally, the groundwater was concentrated at 29 nodes that were chosen in the upper Duplin along the shoreline at Moses Hammock. These nodes were chosen as they outlined the coastline of Moses Hammock. Refer to Figure 2.10 for a layout of the original setup for groundwater inputs. Groundwater was initially input at a constant rate of  $3.7 \times 10^{-3} \text{ m}^3 \text{ s}^{-1}$  and at an initial salinity of 0 PSU. The magnitude of the volumetric flow was initially estimated by starting with values that collaborators, Rich Viso and Rick Peterson, from Coastal Carolina University had come up with from running Radon tracing experiments in the upper Duplin. They estimated that the magnitude of the groundwater input in the upper region of the

Duplin was  $11 \text{ m}^3 (\text{m of coastline})^{-1} (\text{tidal cycle})^{-1}$ . For a distance of 435 m along the coastline of Moses Hammock with 29 nodes being used and the dominant tidal cycle of 12.4 hrs, the volumetric flow rate at each node was calculated to be  $3.7 \times 10^{-3} \text{ m}^3 \text{ s}^{-1}$  and the total groundwater input was  $0.1073 \text{ m}^3 \text{ s}^{-1}$ . From conversations with our collaborators from CCU, it was determined that the groundwater input would be much saltier than the original 0 PSU inputs. Using this same arrangement, model runs with 15 PSU inputs and 30 PSU inputs were then carried out. The volumetric flow rates were also doubled and tripled.

After further tests, it was decided that the most realistic and reasonable approach to including groundwater in the model was to distribute the inputs along the entire length of the Duplin with the majority of the inputs being concentrated in the upper Duplin and gradually being reduced along the nodes in the southward direction. Groundwater was input on nodes distributed along the thalweg. As the nodes are more heavily concentrated in the top of the Duplin and become more spaced out in the southward direction, the desired effect of the cascading groundwater inputs was achieved. See Figure 2.11 for a visualization of the layout for the groundwater inputs for the final model runs. Many different runs were carried out with this arrangement by varying the volumetric inputs at each node and the salinity at each node. The original magnitude of the volumetric input of  $3.7 \times 10^{-3} \text{ m}^3 \text{ s}^{-1}$  was used and this value was doubled and tripled. Salinity was varied from 20 PSU to 30 PSU over different runs. By comparing the salinity profiles of all the different model runs and considering what was a realistic input, it was determined that using a salinity of 20 PSU with a volumetric input of  $7.4 \times 10^{-3} \text{ m}^3 \text{ s}^{-1}$  was the most reasonable and realistic values to input groundwater at every node. The total volumetric input for groundwater for all input nodes is thus  $0.6808 \text{ m}^3 \text{ s}^{-1}$  for the final model runs which is approximately 6 times greater than the previous run. This is approximately  $2.5 \text{ m}^3 (\text{m of coastline})^{-1} (\text{tidal cycle})^{-1}$  on average for the entire length of the Duplin, with the majority of the groundwater being concentrated in the upper Duplin. This is with 92 input nodes along the thalweg, with a length of 12 km for the entire thalweg, and with the dominant tidal cycle of 12.4 hrs. This number is smaller than

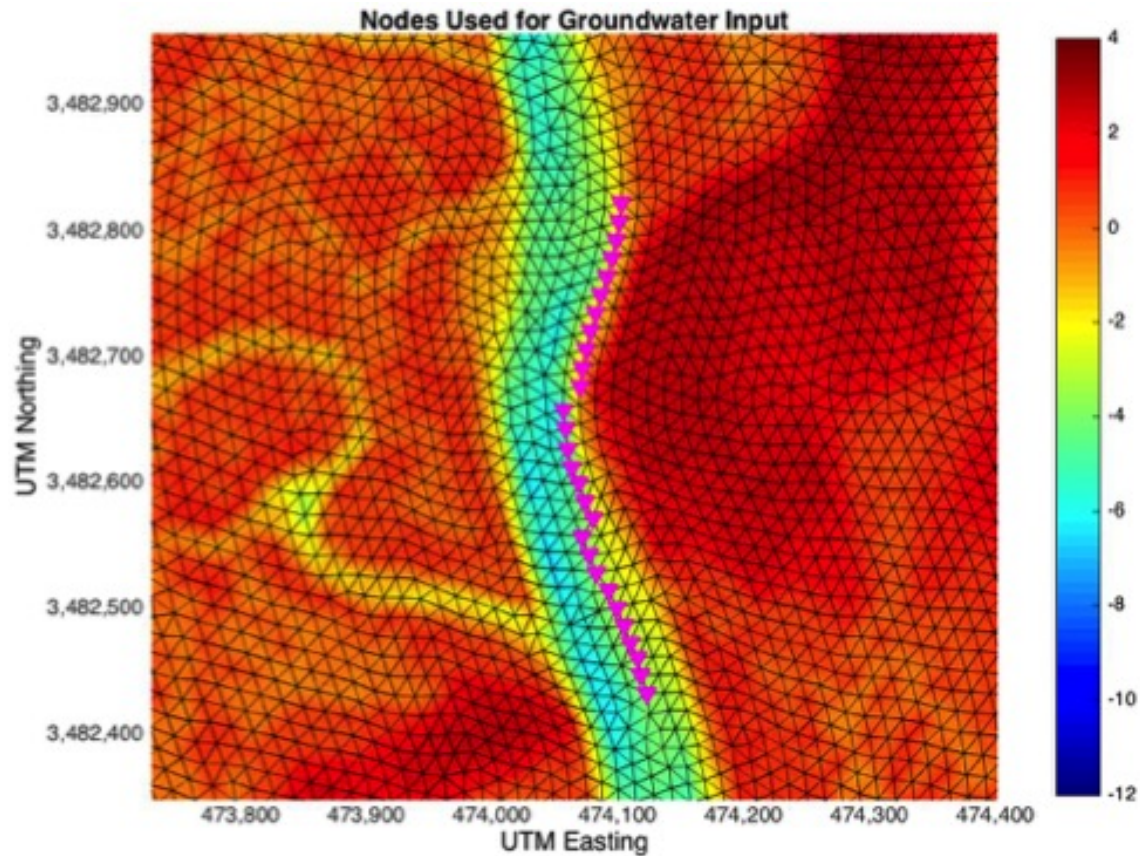


Figure 2.10: Layout for ground water inputs for earlier model runs. Total discharge is  $0.1073 \text{ m}^3 \text{ s}^{-1}$ .

the  $11 \text{ m}^3 (\text{m of coastline})^{-1} (\text{tidal cycle})^{-1}$  originally recommended, but it should be noted that the smaller value represents the entire length of the thalweg, while the original was just for the upper domain around Moses Hammock where groundwater inputs are known to be greatest.

It should be noted that with regards to volumetric flow rate, this groundwater input is treated as a new source of volume, and not strictly as freshwater input. With regards to salinity, the groundwater is treated as stored seawater that has been mixed with fresher groundwater within the estuary and recirculated within the ground.

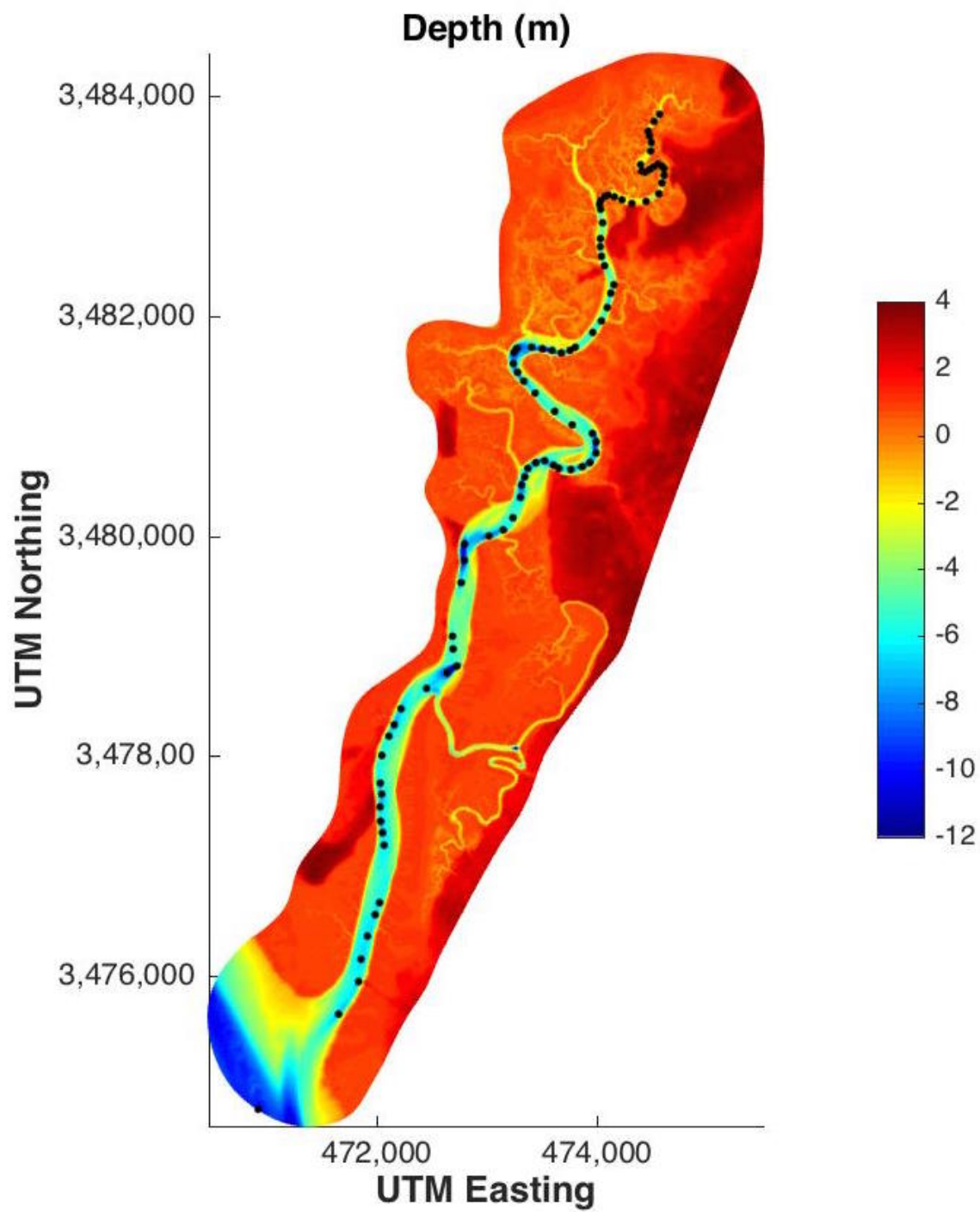


Figure 2.11: Location of groundwater nodes for latest model runs. Total discharge is  $0.6808 \text{ m}^3 \text{ s}^{-1}$ .

## 2.8 DATA/MODEL COMPARISONS

The model output has been compared to real time monitoring stations within the model domain. These long term monitoring stations are GCE10 and Marsh Landing. Refer to Figure 2.5 showing where these stations are located within the domain. A tidal harmonic analysis using T\_tide (*Pawlowicz et al.*, 2002) has also been carried out on model output of surface elevation data at representative model nodes near each station, to allow for comparisons of the dominant tidal constituents between the model and measured SSH. Starting in the top of the domain, GCE10 will be compared first. In order to simplify the figures, a 31 day period has been identified for direct model comparisons. Figure 2.12 displays the tidal height for GCE10 and for a representative model node for the month of March in 2014. The model does very well at simulating tidal variations with a  $r^2$  value of 0.98 at this station.

The entire model run for the year 2014 has also been used for a tidal harmonic analysis showing only those tidal constituents with a signal to noise ratio larger than 100. Table 2.2 displays the six major tidal constituents from the tidal harmonic analysis at the representative model node and at the GCE10 station. The standard error reported from T\_tide is also included for each amplitude and phase below. The model does well at creating these tidal constituents and matches up very closely to the tidal analysis done on the observed data from GCE10.

Figure 2.13 (upper panel) shows the sub-tidal (daily averaged) salinity and SSH comparison at GCE10 to the same model node for the year 2014. The model does very well at capturing sub-tidal effects on SSH, with a  $r^2$  value of 0.91, and generally displays very good agreement with daily averaged values from the GCE10 station. However for salinity, the comparison is not so good as the model tends to underestimate the salinity in the second half of the year. The correlation coefficient is still high with an  $r^2$  value of 0.86 indicating that the variability is captured.

Tidal comparisons were also carried out at the Marsh Landing station with tidal height. The comparisons for tidal height were carried out on the same 31 day period shown above

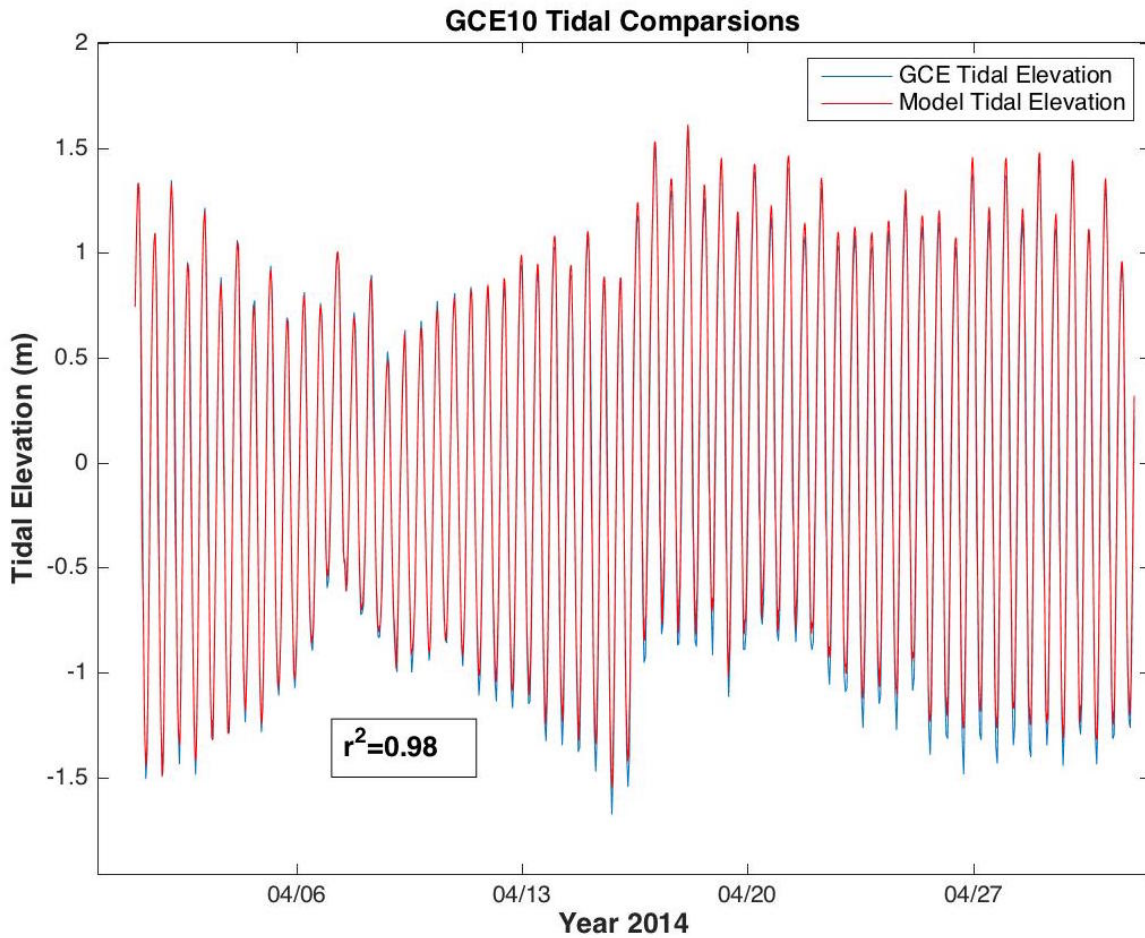


Figure 2.12: Tidal elevation at GCE10 and a nearby model node.

Table 2.2: Tidal Harmonic Analysis Comparison at GCE10

Tidal Constituent	Model Amplitude	GCE10 Amplitude	Model Phase	GCE10 Phase
O1	$0.0804 \pm 0.007$	$0.0872 \pm 0.007$	$213.823 \pm 4.3$	$215.632 \pm 4.4$
K1	$0.111 \pm 0.006$	$0.116 \pm 0.006$	$204.899 \pm 3.3$	$207.872 \pm 3.1$
N2	$0.213 \pm 0.01$	$0.223 \pm 0.01$	$9.816 \pm 3.0$	$14.354 \pm 3.0$
M2	$0.999 \pm 0.009$	$1.0386 \pm 0.01$	$21.385 \pm 0.6$	$24.133 \pm 0.6$
S2	$0.162 \pm 0.01$	$0.168 \pm 0.01$	$56.618 \pm 4.0$	$61.117 \pm 4.4$
M4	$0.0446 \pm 0.006$	$0.0702 \pm 0.007$	$161.767 \pm 7.6$	$182.618 \pm 5.3$

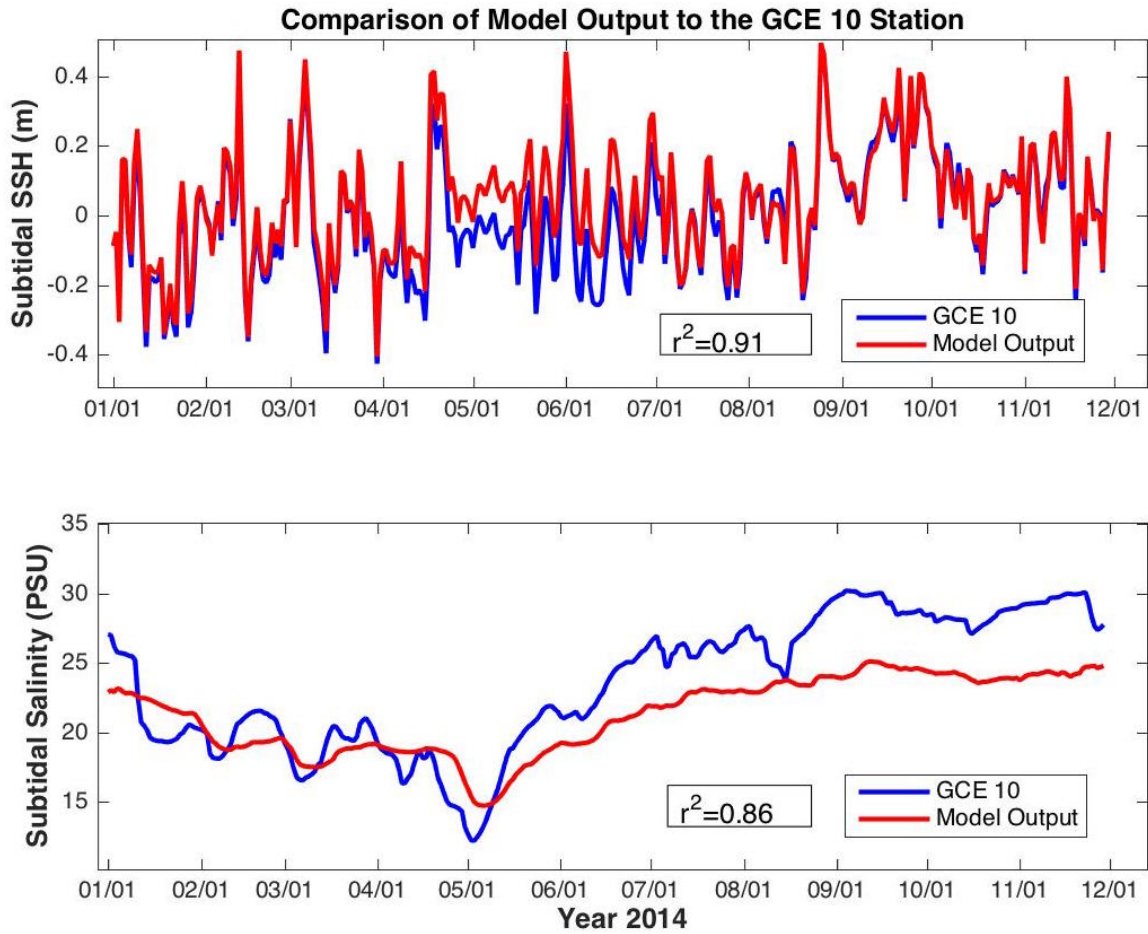


Figure 2.13: A comparison of daily averaged SSH and salinity model output to GCE 10 data.

for GCE10. Figure 2.14 displays the comparison of the model at the representative node to the Marsh Landing monitoring station. This figure shows that the model is very capable of modeling the tidal height at this station with a  $r^2$  value of 0.97. A tidal harmonic analysis using T\_tide was also carried out for the model data and real time series data at the Marsh Landing station. The only components with a signal to noise ratio greater than 100 at this station were the N2, M2, and S2 tidal constituents. For this reason, these are the only components reported in Table 2.3 from the tidal analysis. The standard errors from T\_tide are also reported in Table 2.3. Overall, the model does very well at picking up the phases and amplitudes of the major tidal constituents at the Marsh Landing station. The amplitudes and phases are within two standard errors of each other for both constituents. The phases are less than 10 degrees of each other.

Figure 2.15 shows the comparison of sub-tidal model SSH and salinity output from the representative node to the Marsh landing station. The model does a very good job of picking up the daily averaged values of SSH. However model salinity seems to underestimate the data by approximately 2 PSU. A correlation analysis gives  $r^2$  values of 0.93 and 0.92, respectively.

When considering these comparisons, it can be concluded that the model does well at predicting tidal heights from the major tidal constituents and subtidal variations from offshore forcing. Thus inundation patterns are expected to be well represented. It can also be concluded that the model does well in the lower Duplin at predicting daily averaged salinity but becomes less accurate in the upper ranges of the Duplin, especially later in the year when offshore SSH forcing is large. We hypothesize that overflow from the western and northern boundaries having higher salinities may happen during periods of high SSH forcing. Nonetheless, this model development is a good start to understanding the dynamics in the Duplin.

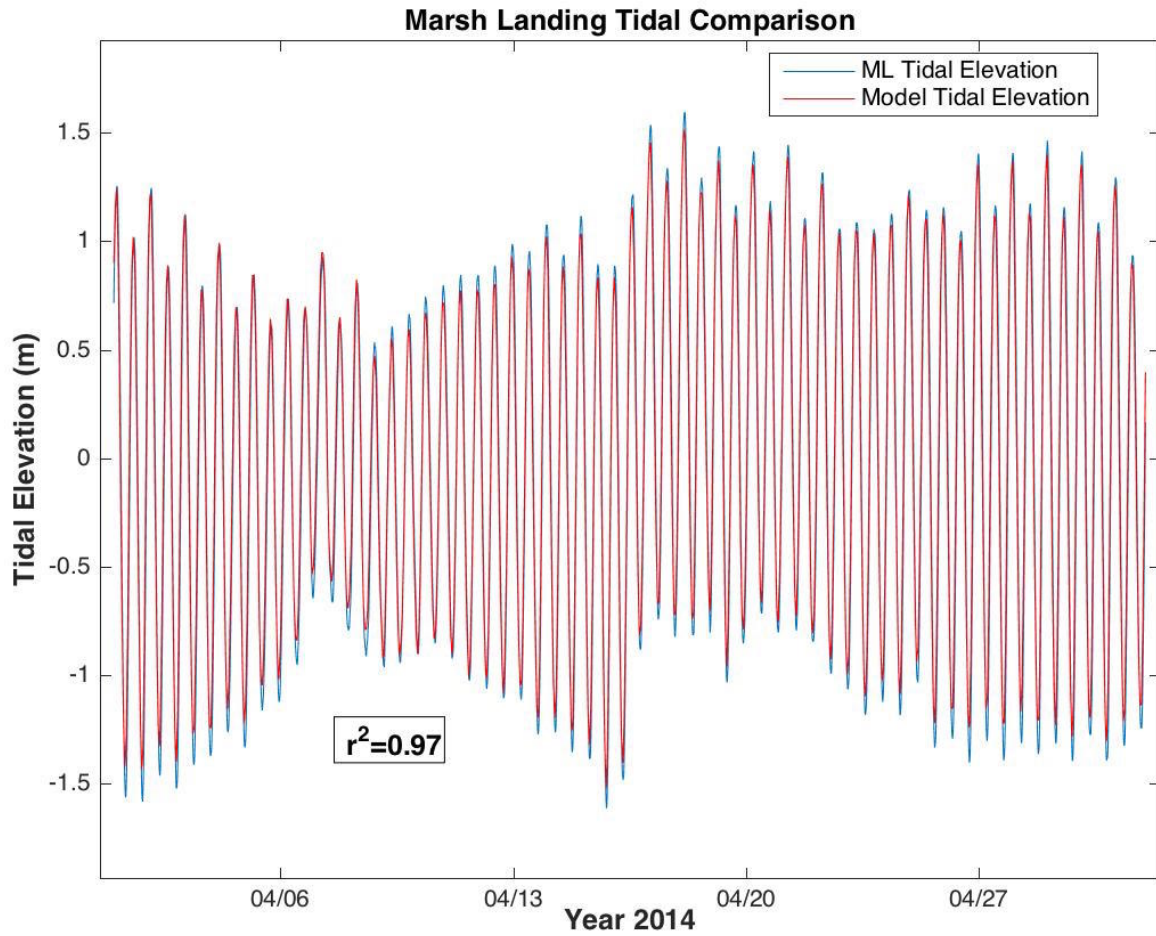


Figure 2.14: Tidal elevation at Marsh Landing and a nearby model node.

Table 2.3: Tidal Harmonic Analysis Comparison at Marsh Landing

Tidal Constituent	Model Amplitude	GCE10 Amplitude	Model Phase	GCE10 Phase
N2	$0.223 \pm 0.02$	$0.200 \pm 0.02$	$12.813 \pm 6.7$	$2.982 \pm 6.6$
M2	$1.027 \pm 0.02$	$0.975 \pm 0.02$	$25.043 \pm 1.4$	$15.116 \pm 1.2$
S2	$0.162 \pm 0.02$	$0.174 \pm 0.03$	$49.22 \pm 7.44$	$60.03 \pm 9.1$

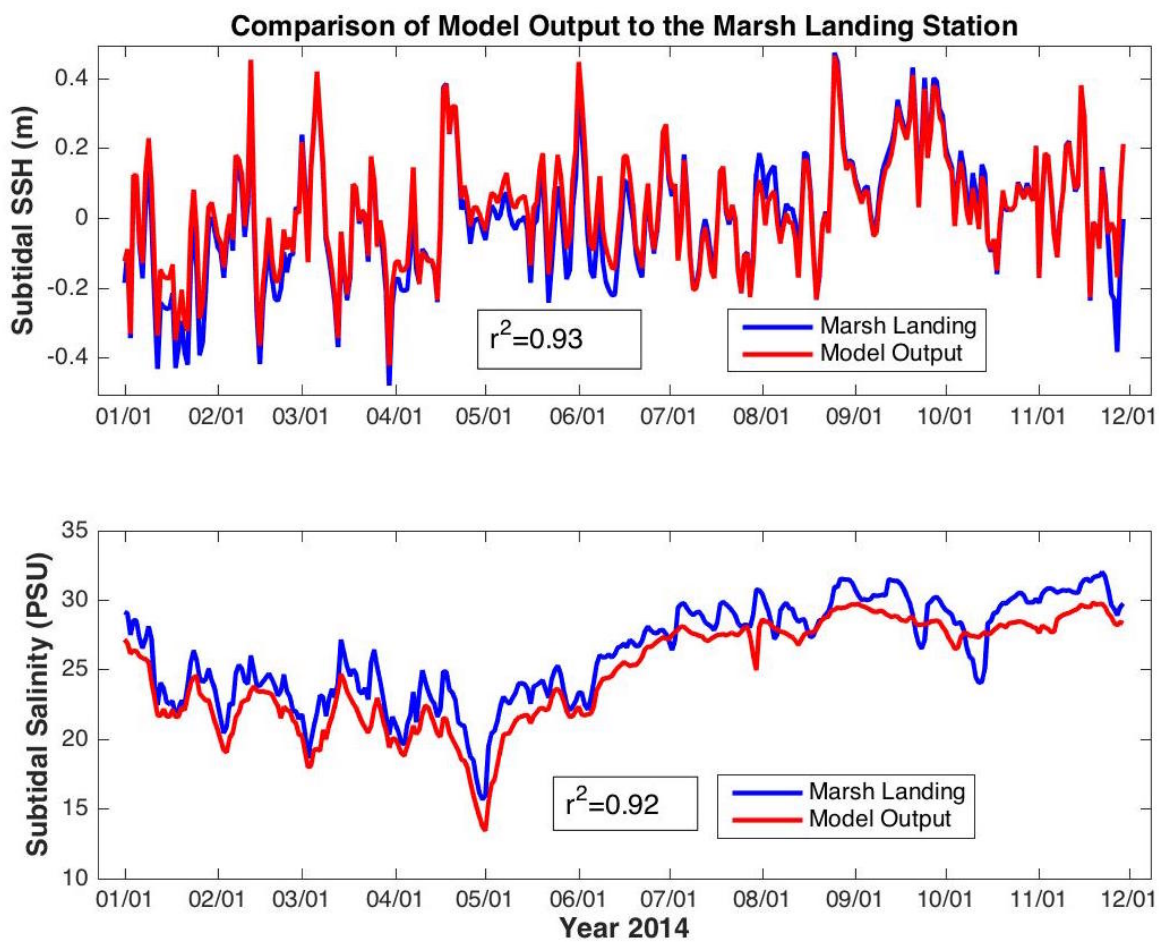


Figure 2.15: A comparison of daily averaged SSH and salinity model output to Marsh Landing data

## CHAPTER 3

### RESIDENCE TIMES THROUGH LAGRANGIAN PARTICLE TRACKING

#### 3.1 INTRODUCTION

Estuaries are major hosts for plankton larvae, pollution or contaminants, and sediment plumes (*Spencer et al.*, 2014). Lagrangian analysis techniques can help shed light on the fates of these impactful scalar groups. Many studies have focused on both numerical modeling based approaches and actual observational approaches using drifters. *Spencer et al.* (2014) carried out a drifter study in Moreton Bay, Australia using two different types of drifters and found that different drifter designs could have strong impacts on the scale of the effect of shear dispersion from winds. Numerical modeling approaches for Lagrangian particle trajectory analysis have been established as useful tools to investigate the sources and ultimate fates of water masses (*Jonsson et al.*, 2011). This study focuses on the numerical modeling of Lagrangian particles for residence time estimations.

Many different studies have used numerical models to carry out Lagrangian particle tracking analyses. *Bilgili et al.* (2005) used an embedded Lagrangian particle tracking module within a two dimensional finite-element model to study transport and exchange and to quantify residence times within the Great Bay Estuarine System located in New Hampshire and found that residence time varied significantly spatially throughout the estuary. *Kenov et al.* (2012) used a two dimensional hydrodynamic model coupled with a Lagrangian transport model to quantify residence time in the Mondego estuary in Portugal and discovered that freshwater input was a major driver of residence time. *Jonsson et al.* (2011) used a three dimensional circulation model and then applied a Lagrangian trajectory analysis to the model output to study the fate of water masses in the Gulf of Finland and learned that the Gulf was

mainly made up of water that originated in the Baltic. *Arega* (2013) used a hydrodynamic model coupled with a Lagrangian particle tracking module to study and quantify residence times in West Scott Creek Estuary in South Carolina and found that residence time varied spatially throughout the estuary. *Huhn et al.* (2012) used a three dimensional hydrodynamic model in conjunction with surface drifters to study the surface Lagrangian transport in the Ria de Vigo estuary in northwestern Spain. *Safak et al.* (2015) used a 3-dimensional finite-volume model coupled with a Lagrangian particle tracking module to quantify residence time and exchange in 14 different bays along the Atlantic coast of the United States and showed that residence time was spatially variable and was dependent on the phase of the tide when the particles were released. *Andutta et al.* (2016) used a three dimensional hydrodynamic model coupled with particle tracking simulations to study how the release time of particles, including slack high and low tides with spring and neap tides, will affect residence time for the Caraveles and Peruípe Rivers in southern Brazil and found that residence time would be most heavily influenced by the tidal phase when the particles were released. This study will present a similar scientific approach detailing the effect of semidiurnal tidal cycles, the spring/neap cycle, and different seasonal time frames on residence time throughout the Duplin model domain.

### 3.2 METHODS

The online Lagrangian particle tracking module provided with the FVCOM source code solves a non-linear system of ordinary differential equations (ODEs) (*Chen et al.*, 2013). The system of equations are defined as,

$$\frac{d\vec{x}}{dt} = \vec{v}(\vec{x}(t), t) \quad (3.1)$$

where,  $\vec{x}$  is the 3-dimensional position of any particle at time  $t$ , the time rate of change of particle position is given by  $\frac{d\vec{x}}{dt}$ , and  $\vec{v}(\vec{x}, t)$  is the three dimensional velocity field taken from the model generated output. There is no random-walk component to this approach as this

is not necessary in this highly advective domain. This system of equations is solved using a fourth order four stage explicit Runge-Kutta algorithm solving method. These runs have been carried out using the online mode within the FVCOM source code. For a description of this method see *Chen et al.* (2013).

Custom MATLAB scripts were written to prepare netcdf input files necessary to run the online Lagrangian particle tracking module within the model. The information needed to create the input files were start and stop times for the particle tracking and start locations for all particles. The starting locations for the particles were the same for all Lagrangian particle tracking runs. With the final mesh, all mesh element centroids where the depth was greater than 0.5 *m* were identified. A starting particle was positioned at every centroid that met this criteria and placed at mid-depth. Because this is a well mixed system, particles can overturn very quickly and thus the position within the water column is arbitrary. Figure 3.1 shows the starting particle configuration for all Lagrangian model runs. There were ultimately 24,150 starting particles for every particle tracking simulation.

In all, 32 particle tracking simulations were carried out. Two major seasonal time frames were identified to carry out this analysis. These were the high river discharge (HRD) time period, starting in March which corresponds to low SSH, and the low river discharge (LRD) time period, starting in August that corresponds to high SSH. See Figure 2.6 (bottom panel) for the river discharge in 2014 and Figure 2.13 for SSH. Sixteen simulations were carried out for each discharge time respectively. Each simulation was set for a maximum of 45 days. This value was determined through trial and error given that particles never stayed in the system longer than this time except for particles that were deemed to have become stuck in the uplands or high marsh regions and thus were thrown out of the analysis. For each seasonal time frame, the model was started at 8 different times spanning both a spring tide and a neap tide. Within each spring and neap period there were 4 time points that were started at slack low tide and 4 that were started at slack high tide each spanning a two day period.

### Particle Starting Positions with Inverse Bathymetry (m)

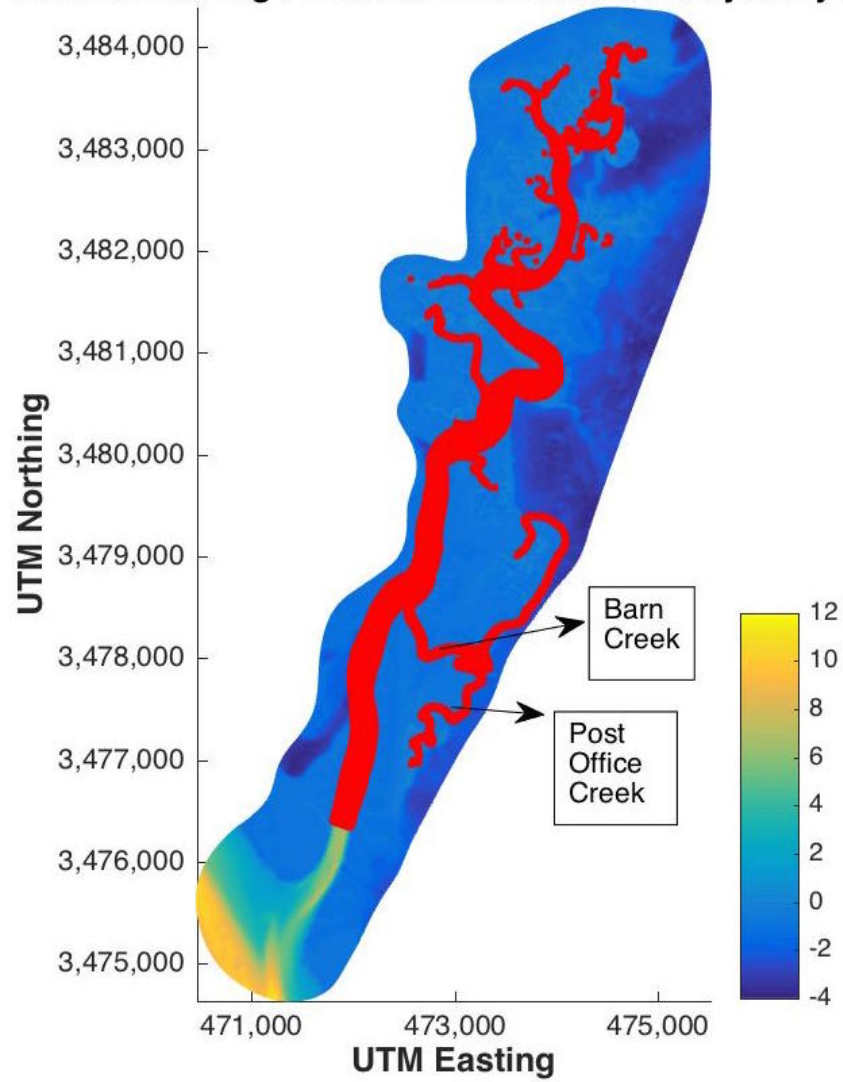


Figure 3.1: The starting particle positions for all Lagrangian particle tracking simulations.

This was in order to better understand how the spring/neap cycle in conjunction with the stage of the tide will affect residence times within the domain.

After all the runs were completed, residence time was calculated for every particle. This was determined by setting an exit point at Marsh Landing and calculating the time it takes a particle to cross this point and exit the domain the first time. Thus, for this study, residence time is defined as the time it takes a water particle to pass Marsh Landing in the lower model domain. Particles could theoretically return into the domain, but this is not considered for the scope of this research. For each particle, all other particles within a 50 *m* distance were identified and a weighted average was obtained for both the  $(x, y)$  position and the residence time resulting in a spatial average for both. It is important to note that the spatially averaged  $(x, y)$  positions will be the same for all 32 different simulations, as the starting positions for the particles are the same for all runs. The weight function used is,

$$W = e^{-r/10} \tag{3.2}$$

where  $r$  is the distance between the particle position in question and each particle that falls within the 50 *m* range (*Wang*, 2016b). This weight function has the property that a particle 10 *m* away will only contribute 36.8% to the average position and residence time. At a 50 *m* distance, the contribution would be less than 1%. After all the weighted values were calculated for each run, the residence times were then averaged over different periods. Ten different residence time averages and resulting statistics are obtained which represents a temporal average of the dynamics under investigation.

### 3.3 RESULTS AND DISCUSSION

The output from the Lagrangian particle tracking simulations was averaged in a variety of ways to investigate the goals of this project. One goal was to understand how residence time will change under different seasonal forcings. The Altamaha River effluent that makes its way to Doboy Sound and subsequently into the Duplin is one specific seasonal forcing that

was concentrated on for this study since it also corresponds to different levels of SSH and inundation. Another goal was to understand how the spring/neap cycle in conjunction with the semi-diurnal tidal cycle would affect residence time within the domain.

Figure 3.2(a) displays the average residence time for all 8 simulations starting on a spring tide during the HRD period. Of these 8 simulations, 4 were started on slack low water and 4 were started on slack high water. The upper Duplin has a greater residence time (approximately 7 days) compared to the lower Duplin. This is likely due to the fact that on the spring tide, more particles can be transported further into the Duplin and into the upper marsh in areas that only become inundated on spring tides. The residence time averaged over the whole domain during this spring tide was 1.29 days with a standard deviation of 1.05 days. The median was 1.05 days and the maximum was 10.37 days. Due to the high energetics associated with spring tides, we expect that the residence time will be smaller on average. This is because the high energy tide will flush the system faster when compared to the overall residence time for neap tides as will be shown.

Figure 3.2(b) displays the average residence time for all 8 simulations that started on a neap tide during the HRD period. This includes 4 times at slack low water and 4 times at slack high water spanning 2 days of the neap tide. The highest residence times are within Barn and Post Office Creeks, which implies that water can be trapped in these waters until the next spring tide comes along to flush the creeks. The residence time averaged over the whole domain on this neap tide during the period of HRD was 1.54 days with a standard deviation of 1.56 days, which are slightly higher than those values for the spring tide HRD period. The median was 0.99 days and the maximum is 23.61 days which is observed in Barn and Post Office Creek areas. This can be interpreted to mean that residence time can be much larger and more variable throughout the domain as the neap tides are less energetic for transporting water out of the system.

Figure 3.3(a) displays the average residence time for the 8 simulations started on the spring tide during the period of LRD and relatively high SSH. The higher residence times

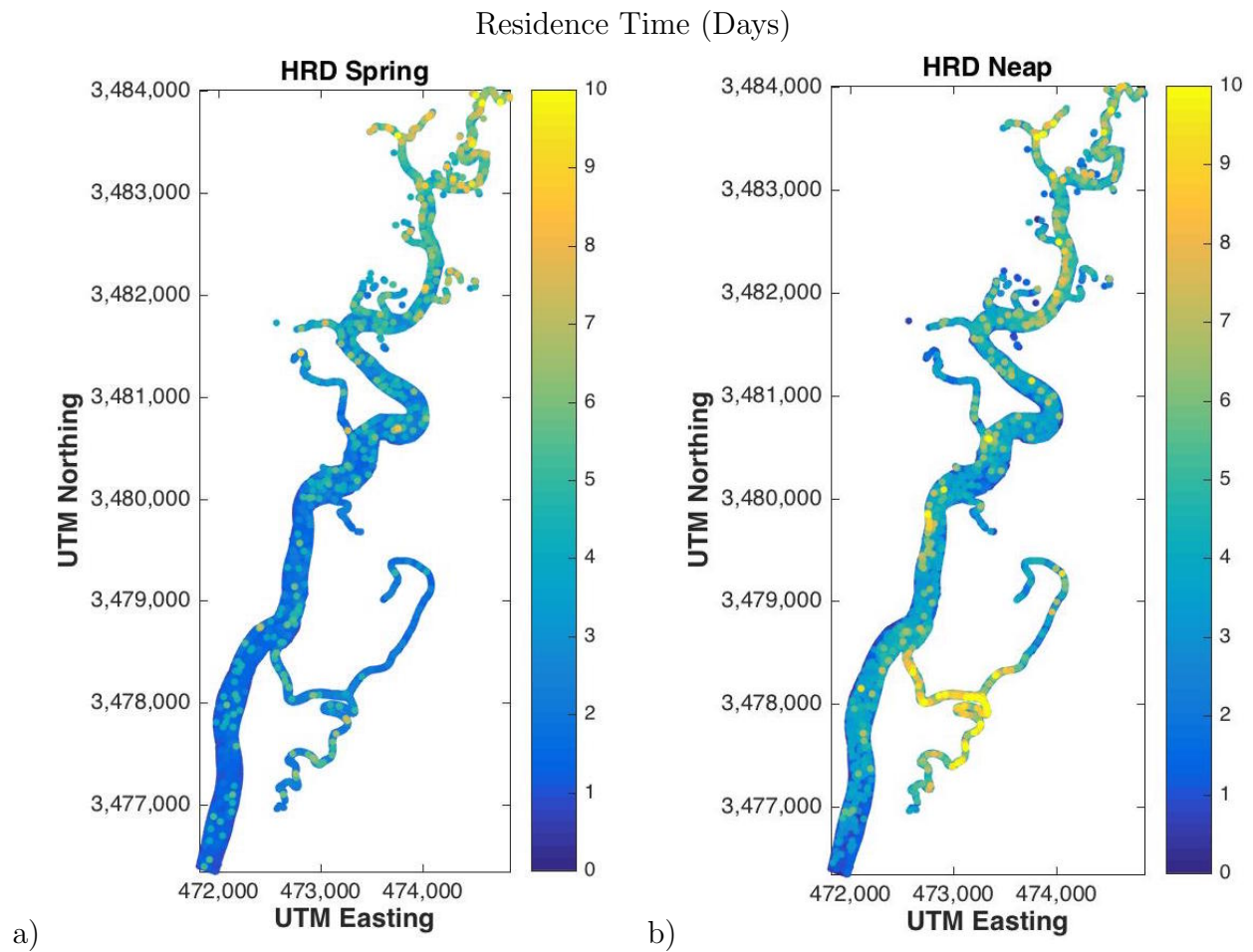


Figure 3.2: Average residence time for all 8 simulations starting on a) a spring tide and b) a neap tide during the HRD period.

are now distributed over more of the Duplin spanning the mid to upper reaches compared to the spring HRD period, where higher values were focused only in the upper reaches. The residence time averaged over the entire domain was 1.95 days with a standard deviation of 1.70 days. The median was 1.60 days and the maximum was 13.1 days. These values are higher than the values reported for the period of HRD shown in Figure 3.2(a). Simulations started on the spring tides can have large average residence times due to the higher levels of inundation pushing water particles back into the farther ranges of the Duplin and this is enhanced when there is less freshwater influence. Thus, the residence time is generally higher during the LRD period.

Figure 3.3(b) illustrates the average residence time for the 8 simulations started on the neap tide during the period of LRD. Once again, the mean residence times for the neap tide simulations are higher than the mean residence time values from the spring tide simulations and values are distributed throughout the domain. The residence time averaged over the entire domain was 2.08 days with a standard deviation of 1.58 days. The median was 1.68 days and the maximum was 16.52 days. Similar to the comparison between the HRD and LRD spring tides, these values are much higher than the values shown for the corresponding neap tide during the period of HRD shown in Figure 3.2(b).

Figure 3.4(a) displays the residence time when averaging over the 8 simulations starting on slack high water for the HRD time period. This includes 4 spring and 4 neap tide starts and thus averages out their effect. The simulations starting on slack high water begins with all water particles moving out of the system, so residence time should be smaller throughout the domain. The residence time averaged over the entire domain for all high tide starts during the period of HRD was 1.12 days with a standard deviation of 1.23 days. The median was 0.69 days and the maximum was 13.0 days. The mean and the median residence times are generally smaller than the spring or neap runs discussed previously.

Figure 3.4(b) shows the average residence time for all simulations starting on slack low water during the HRD period, with 4 simulations starting on both neap and spring tides,

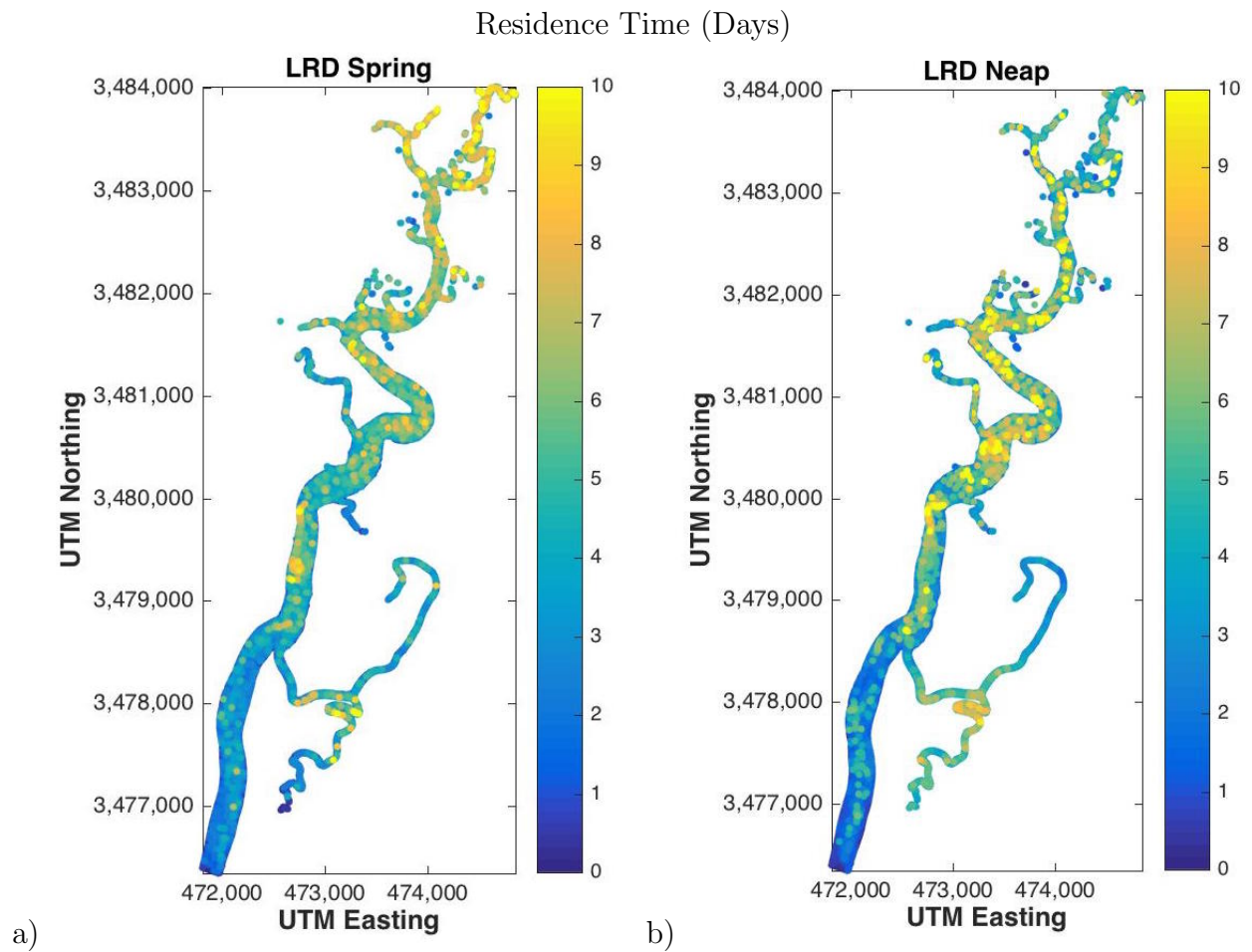


Figure 3.3: Average residence time for all 8 simulations starting on a) a spring tide and b) a neap tide during the period of LRD.

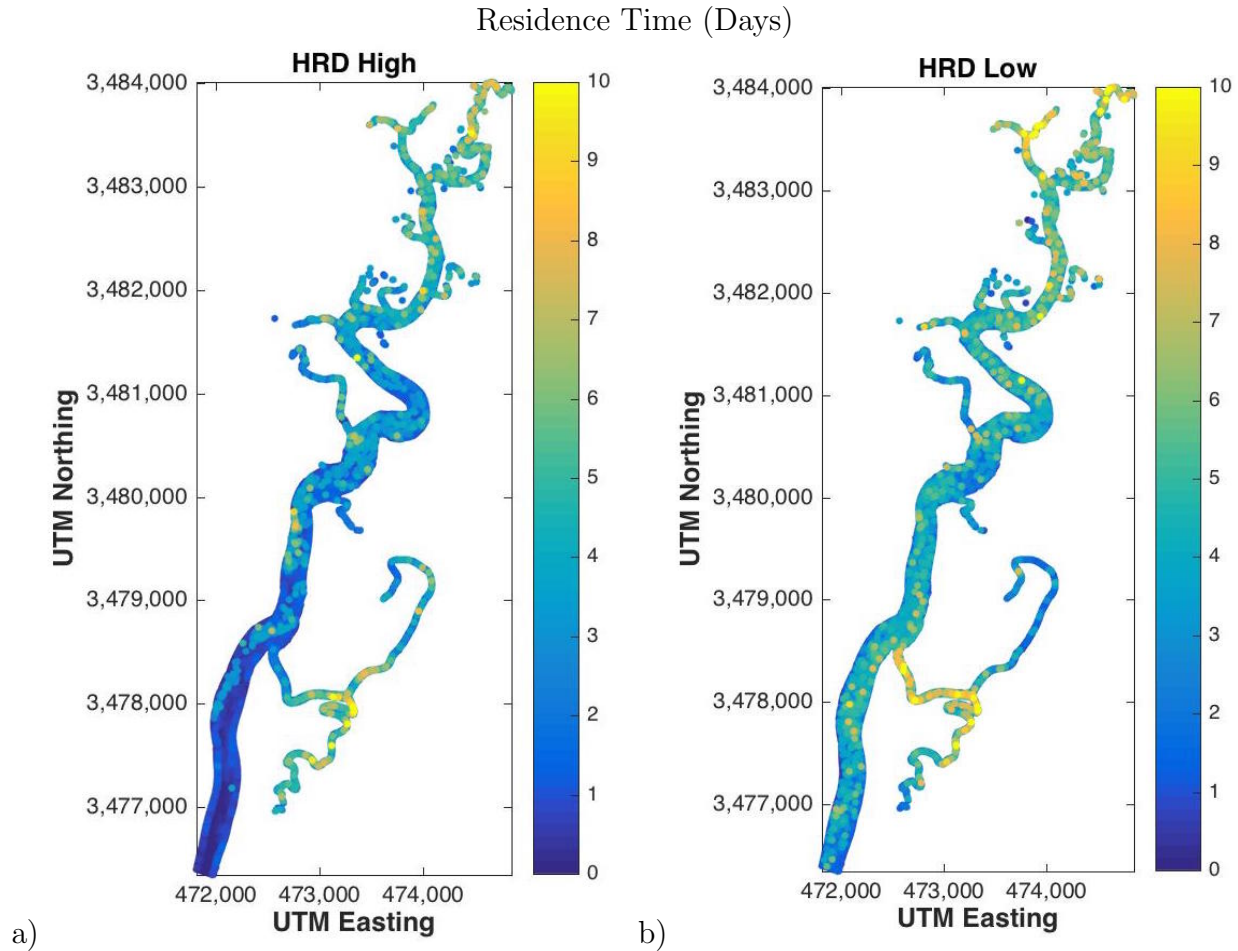


Figure 3.4: Average residence time for all 8 simulations starting on a) slack high tide and b) slack low tide during the HRD period.

thus averaging out their effect. The simulations that start on slack low water move particles into the domain as the tide begins to flood. Particles are pushed back into the marsh and into smaller side creeks. The average residence time is then increased because it takes longer for these particles to get flushed back out of the marsh and back ranges of these smaller side creeks. The residence time averaged over the entire domain for all low tide starts during the period of HRD was 1.72 days with a standard deviation of 1.40 days. The median was 1.32 days and the maximum was 13.22 days. The mean and the median residence time are the largest for all starting arrangements under HRD conditions.

Figure 3.5(a) shows the average residence time for the 8 simulations started on the slack high tide during the period of LRD with 4 simulations started on neap and spring tides, thus averaging out their effects. Similar to what has been shown with HRD simulations, runs started on the slack high tide have the lowest mean residence time and median values among all the LRD simulations. Again, this is due to the fact that when simulations are started on slack high water, the particles are immediately flushed out of the domain with the powerful ebb dominated tide. The residence time averaged over the entire domain was 1.61 days with a standard deviation of 1.61 days. The median was 1.14 days and the maximum was 14.74 days. The average residence time is higher than the average residence time reported in Figure 3.4(a) from slack high tide starts during the HRD period.

Figure 3.5(b) displays the average residence time for the 8 simulations started on the slack low tide during the period of LRD averaged over 4 neap and 4 spring tide starts. When compared to other simulations from the low river discharge period, simulations started on slack low tide display the highest mean residence times. This is the same as what was seen when comparing the slack low tide run for the HRD period. The residence time averaged over the entire domain was 2.41 days with a standard deviation of 1.62 days. The median was 2.08 days and the maximum was 15.84 days. These values are considerably higher than the corresponding residence times from the slack low tide start simulations during the HRD period shown in Figure 3.4(b).

Figure 3.6(a) displays the average residence times for all 16 Lagrangian simulations carried out over the HRD period. This includes 8 simulations started on a neap tide and 8 simulations started on a spring tide. Within the 8 spring tide and 8 neap tide starts, there were 4 low tide and 4 high tide starts, respectively. This figure illustrates that average residence time is generally low throughout the domain during HRD periods, but can be higher in the backs of Barn and Post Office Creek and also in the upper ranges of the Duplin. The residence time averaged over the entire domain for the HRD period was 1.42 days with a

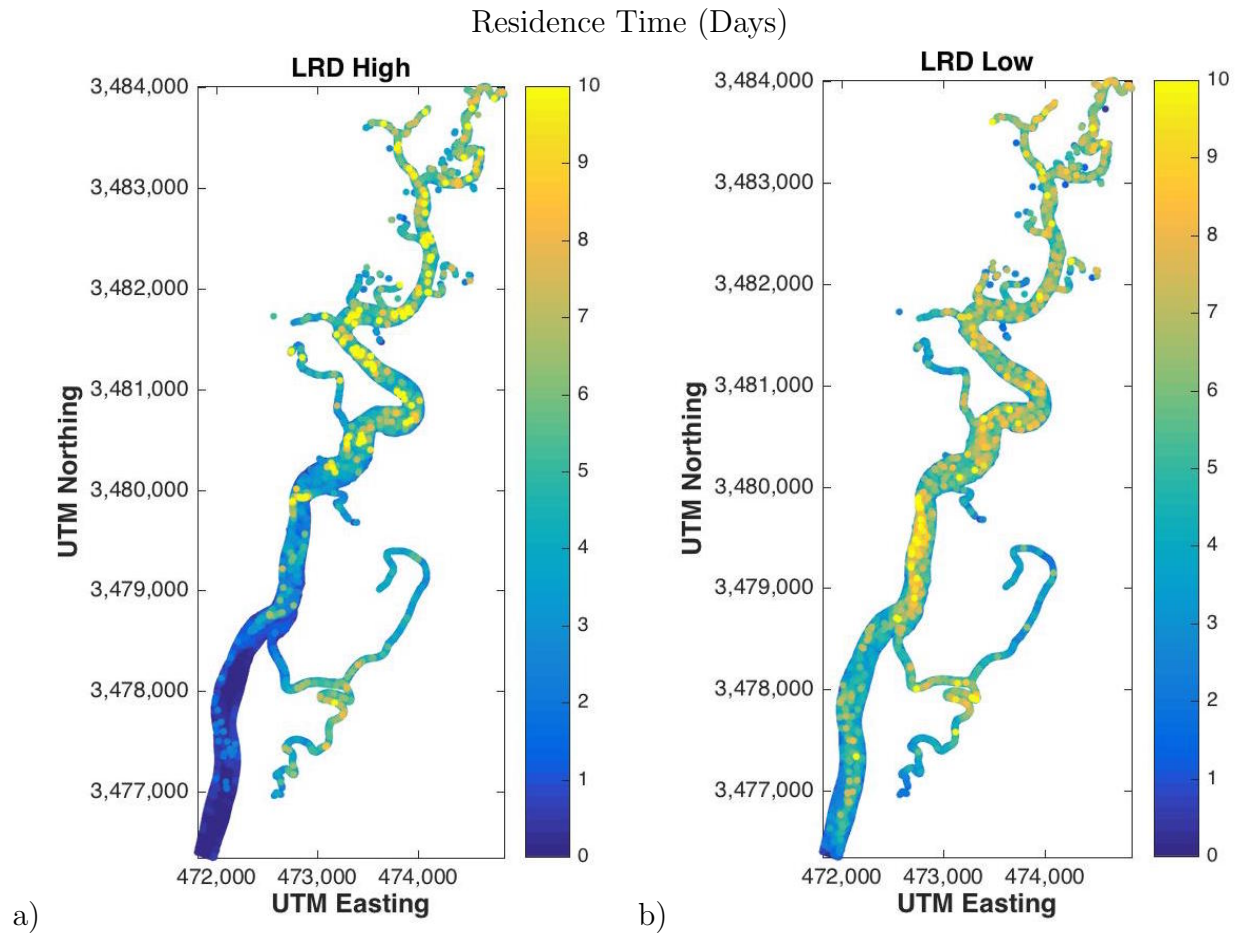


Figure 3.5: Average residence time for all 8 simulations starting on a) slack high tide and b) slow low tide during the period of LRD.

standard deviation of 1.04 days. The median residence time was 1.09 days with a maximum of 12.92 days.

Figure 3.6(b) shows the average residence time for all 16 simulations started during the period of LRD. This includes 8 simulations started on a spring tide and 8 simulations started on a neap tide. Within each spring and neap simulation, there were 4 simulations started on slack high water and 4 simulations started on slack low water. Average residence time is higher over most of the domain from the mid to upper regions of the Duplin for the period of LRD than for the period of HRD. The residence time averaged over the entire domain was 2.01 days with a standard deviation of 1.24 days. The median residence time was 1.81 days and the maximum was 12.0 days. The mean and the median residence times are considerably higher when compared to the overall residence time of the HRD simulations shown in Figure 3.6(a). This is most likely due to the higher inundation which is a function of the prevailing northeasterly winds that are characteristic during this LRD period. Higher inundation leads to particles being pushed farther back into the marsh and thus leads to greater residence times during this time period.

### 3.4 SUMMARY AND CONCLUSIONS

A tabular list of the domain averages for all runs are summarized in Tables 3.1 and 3.2. Three general conclusions can be seen: First, particles released in the Duplin at low water have higher residence time than particles released in the Duplin at high water. Simulations started on slack low water have the largest average and median residence times during the periods of both HRD and LRD. Second, regardless of river discharge effects, particles initiated over the neap tide have greater residence time than those initiated at spring tides. Third, low river discharge residence times are greater than high river discharge residence times regardless of the tidal phase. It can also be stated that residence times can vary strongly spatially, which agrees with what *Bilgili et al.* (2005) found in their study of the Great Bay estuarine system. Throughout this domain, the upper Duplin and the back reaches of Barn

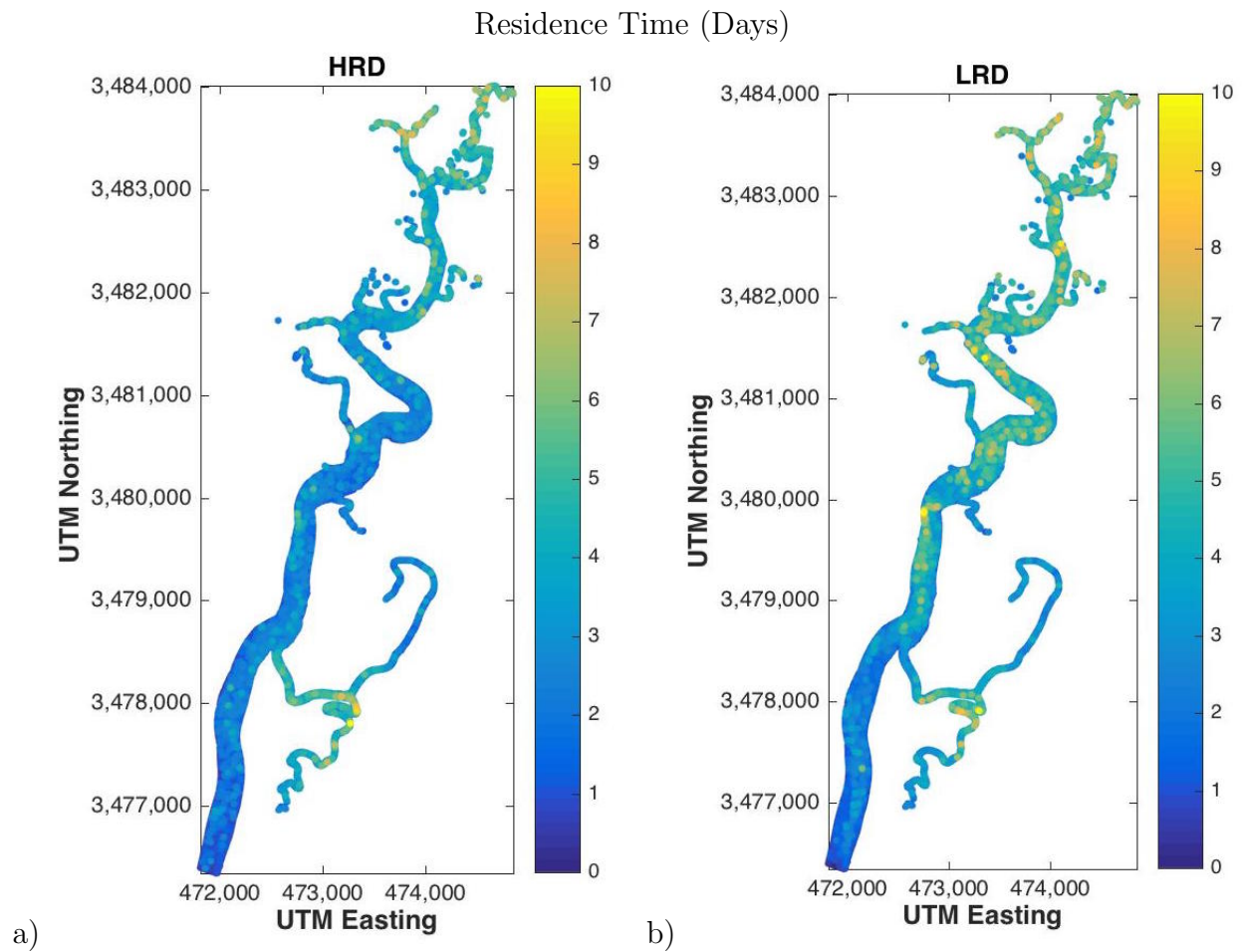


Figure 3.6: Average residence time for all 16 simulations during the a) high river and b) low river discharge period.

and Post Office Creeks show higher residence times over all averaging schemes presented here.

Simulations that are started on slack high water have smaller values of average residence time than simulations started on slack low water. Water that has flooded into the marshes and creeks on the rising tide will be immediately flushed down and out of the Duplin on the ebbing tide because of the powerful ebb dominant tide. This trend is observed for both the LRD and the HRD periods. Residence time is more sensitive to tidal phase than it is to the spring/neap cycle. This conclusion was also found by *Andutta et al.* (2016) in their study in southern Brazil.

For both the HRD and LRD periods, neap tide starts showed higher average residence times than spring tide starts. There is more variability throughout the Duplin and in the back sections of Barn and Post Office Creeks. This can be attributed to the less energetic neap tides not flushing water out of areas that are back in Barn and Post Office Creeks and from the mid to upper reaches of the Duplin. The more energetic spring tides flush water out of the domain much faster and thus have smaller average residence times over the domain.

Another major conclusion for this study is that the residence time over the domain is higher during the LRD period than during the HRD period for all runs. This trend held up for all of the averaging schemes presented here where the average residence time during the LRD period was always larger than the average residence time during the HRD period. From this, it can be concluded that freshwater inputs from the Altamaha river, that are tidally advected into the mouth of the Duplin, can be important drivers of residence times within this domain, which agrees with the findings from a study carried out in Mondego estuary in Portugal by *Kenov et al.* (2012). Also, inundation is generally higher during the LRD time of year due to offshore wind forcing and could also be a driver of the greater residence times.

Table 3.1: Statistical summary of residence time (RT) analysis during a high river discharge period.

Start	Mean RT(Days)	Median RT(Days)	Standard Deviation (Days)	Max RT(Days)
SLW	1.72	1.32	1.40	13.22
SHW	1.12	0.69	1.23	13
Spring	1.29	1.05	1.05	10.37
Neap	1.54	0.99	1.56	23.61
Total	1.42	1.09	1.04	12.92

Table 3.2: Statistical summary of residence time (RT) analysis during a low river discharge period.

Start	Mean RT(Days)	Median RT(Days)	Standard Deviation (Days)	Max RT(Days)
SLW	2.41	2.08	1.62	15.84
SHW	1.61	1.14	1.61	14.74
Spring	1.95	1.60	1.70	13.1
Neap	2.08	1.68	1.58	16.52
Total	2.01	1.81	1.24	12

## CHAPTER 4

### HORIZONTAL TRANSPORT AND SALT FLUX ANALYSIS THROUGH EULERIAN DECOMPOSITION

#### 4.1 INTRODUCTION

In order to study and quantify transport processes, which are major drivers of ecology and biogeochemistry, the patterns of the exchange of freshwater and saltwater must be understood. The distribution of fresh and salt water inputs are also important for management strategies (*Devkota and Fang, 2015*), as the balance between these inputs within an estuary can have large effects on the productivity of the system (*Devkota et al., 2013; Bales et al., 2006*). The hydrodynamics of an estuary along with the salt fluxes are integral to understanding processes that control the biogeochemistry and water quality within estuaries (*Zou et al., 2016*). Salt transport throughout an estuary is an important physical forcing and is controlled by the magnitudes and directionality of the velocities and salinities. The bathymetry of the study site in conjunction with the magnitude of the dominant forcings can also be major controllers of the salt transport within an estuary (*Devkota and Fang, 2015*).

Normally, estuaries have a salt gradient from fresh at the head to saltier at the mouth (a positive estuary). The Duplin River however, presents a unique case in that fresher water from Doboy Sound is tidally advected into the mouth. This fresher water is the result of the Altamaha River water that makes its way through tidal channels and the Intracoastal waterway from Altamaha Sound to Doboy Sound (*Wang, 2016b*). Other pathways are via the coastal ocean. As a result, the Duplin can have very dynamic salinity patterns on seasonal timescales.

In well mixed or weakly stratified estuaries, of which the Duplin is a good example, tidal and shear dispersion can be a major driver of the salt transport characteristics (*Smith, 1980*). A common way to study salt fluxes in estuarine systems is through the Eulerian decomposition method. This has been carried out in many different studies in a variety of different systems. *Devkota and Fang (2015)* used a calibrated hydrodynamic model to carry out a Eulerian decomposition analysis in Wolf and Perdido bays in the Gulf of Mexico and discovered that tidal oscillatory flux ( $F_T$ ) dominated the dispersive terms at some cross sections and that exchange fluxes ( $F_E$ ) dominated dispersion at other cross sections throughout the system. *Lerczak et al. (2006)* used cross sectional sampling techniques to create data sets for an Eulerian decomposition analysis in the Hudson River and found that the magnitudes of dispersion and salt fluxes were heavily dependent on the spring/neap cycle with vertical shear dispersion coefficients showing maximums on neap tides. *MacCready (2011)* used an isohaline and Eulerian decomposition to carry out a salt flux analysis in the Columbia River Estuary and made comparisons between the two approaches. *Chen et al. (2012)* used the isohaline salt flux approach on numerical model output to explore the transport dynamics of the Hudson and Merrimack Rivers and discovered that the ratio of the length scale between salinity intrusion and tidal excursion could be used to identify estuarine systems. *Kim and Park (2012)* used an Eulerian decomposition approach on hydrodynamic model output to explore salt exchange patterns in a northern Gulf of Mexico estuary and showed that salt transport was highly dependent on prevailing winds and riverine discharge rates. *Aristizabal and Chant (2015)* used the Eulerian decomposition approach described by *Lerczak et al. (2006)* to carry out an observational study of salt flux in the Delaware Bay and found that advective salt fluxes ( $F_0$ ) dominated in their system.

*Fischer (1973)* describes dispersion as the spreading of fluid particles due to a combination of the effects of the distribution of velocity and the diffusive processes. Horizontal dispersion is an important parameter that can be quantified by applying the Eulerian decomposition salt flux analysis approach to numerical model output. Dispersion controls the distribution

of pollutants, nutrients, larvae, carbon, and sediments within an estuary (*Aristizabal and Chant, 2015*). Dispersion is dependent on the horizontal salinity gradient and the sum of the exchange and tidal oscillatory components of the salt flux. Longitudinal fluxes along with dispersion, which is dependent on these fluxes, can vary strongly over seasonal and spring/neap time scales (*McKay and DiIorio, 2010*). *Devkota and Fang (2015)* quantified the horizontal dispersion coefficient by applying this analysis to hydrodynamic model output and found that it could vary by an order of magnitude between cross sections in their system. *Silva et al. (2014)* estimated these parameters in the Rio de la Plata estuary along the Argentinian and Uruguayan coasts using a tracer study coupled with a hydrodynamic model and showed that horizontal dispersion coefficients spatially vary significantly within their system.

The initial motivation to carry out this analysis came from previous work by *McKay (2008)*, who found that the salinity gradient reverses on spring/neap timescales in the mid to upper reaches of the Duplin. Figure 4.1 is an example of spring/neap variations observed in the upper Duplin during an experimental program in 2003. The upper panel shows that as the tidal height rises on spring tides (red), the tidal component of salinity also increases, implying that spring tides advect and mix salty water into the upper reaches of the Duplin. However, as tidal height rises on neap tides (green), the tidal salinity decreases, implying that freshwater existing in the mid Duplin is not mixed away. The lower panel shows the along channel salinity gradient reversing on a spring/neap timescale. The sign convention in this plot is defined to be positive out of the estuary, so that a positive salinity gradient corresponds to a positive estuary (salty water at the mouth and fresher water at the head).

In the model simulations, this same phenomenon, the reversing of the salinity gradient, was observed under certain seasonal forcings. It was found that at times of low river discharge (LRD), the Duplin fits into the classical description of a positive estuary where the salinity along the Duplin is from salty to fresh from the mouth to the head. This can clearly be seen

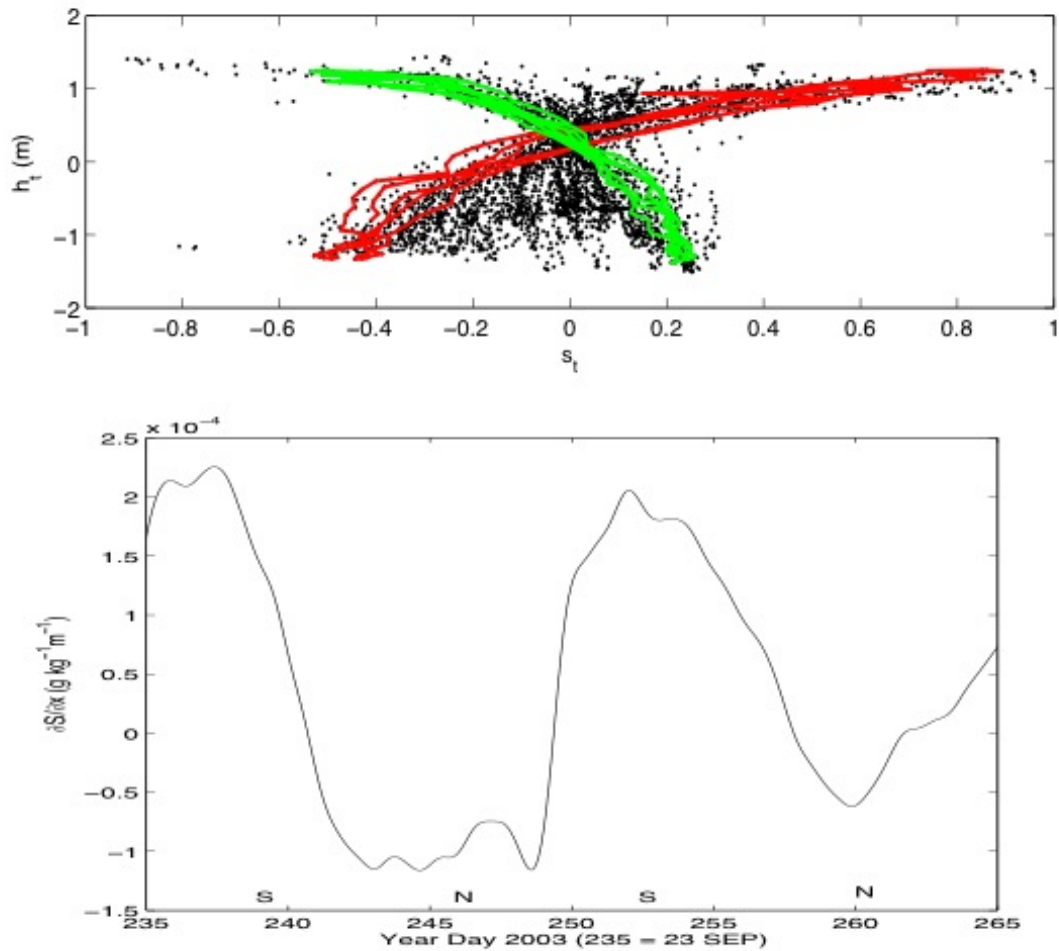


Figure 4.1: (upper panel) Tidal height versus the tidal component of salinity with red representing spring tides and green representing neap tides. (lower panel) The along channel salinity gradient during September/October 2003 in the upper Duplin.

in Figure 4.2, which shows the salinity as a function of depth along the thalweg of the Duplin starting 400 m south of Marsh Landing, which is at the mouth.

However, during times of high river discharge (HRD) from the Altamaha River, the salinity gradient reverses along the thalweg causing what is referred to in this paper as a negative estuary effect. This occurs when a plug of freshwater becomes trapped in the middle Duplin causing a reversal of the salinity gradient from the middle to upper reaches of the

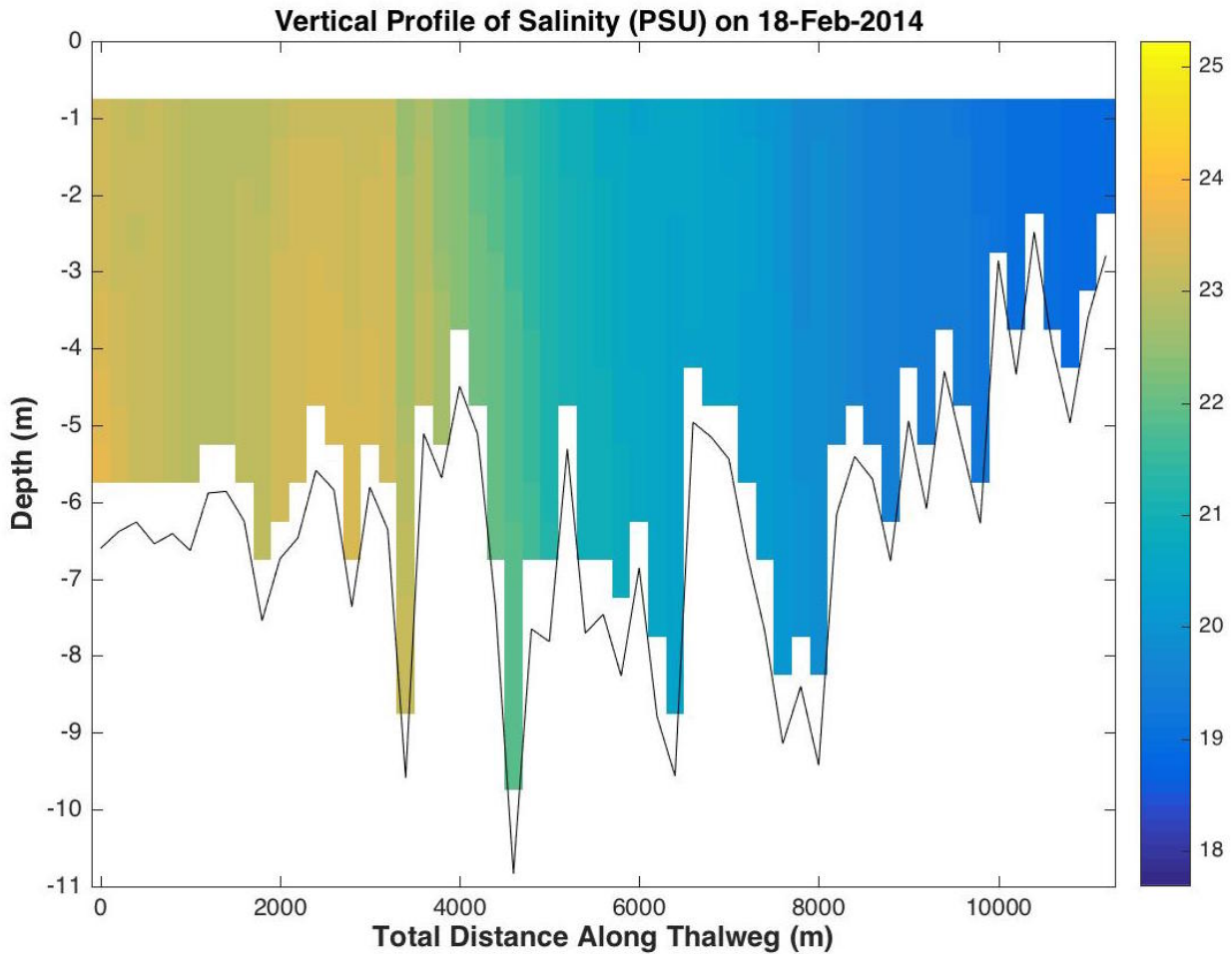


Figure 4.2: A vertical profile of model salinity along the thalweg demonstrating a positive estuary.

Duplin. This plug of freshwater can clearly be seen in Figure 4.3 taken during a time when the Altamaha River discharge was high and the salinity in Doboy Sound was low. The plug of freshwater can cause very interesting and varying dynamics in the mid to upper regions of the Duplin. The plug is generally concentrated in the middle range of the Duplin and thus 4 cross sections along the Duplin are chosen so as to capture spatial changes in salt flux dynamics. The placement of the cross sections relative to the freshwater plug is noted by an asterisk in Figure 4.3.

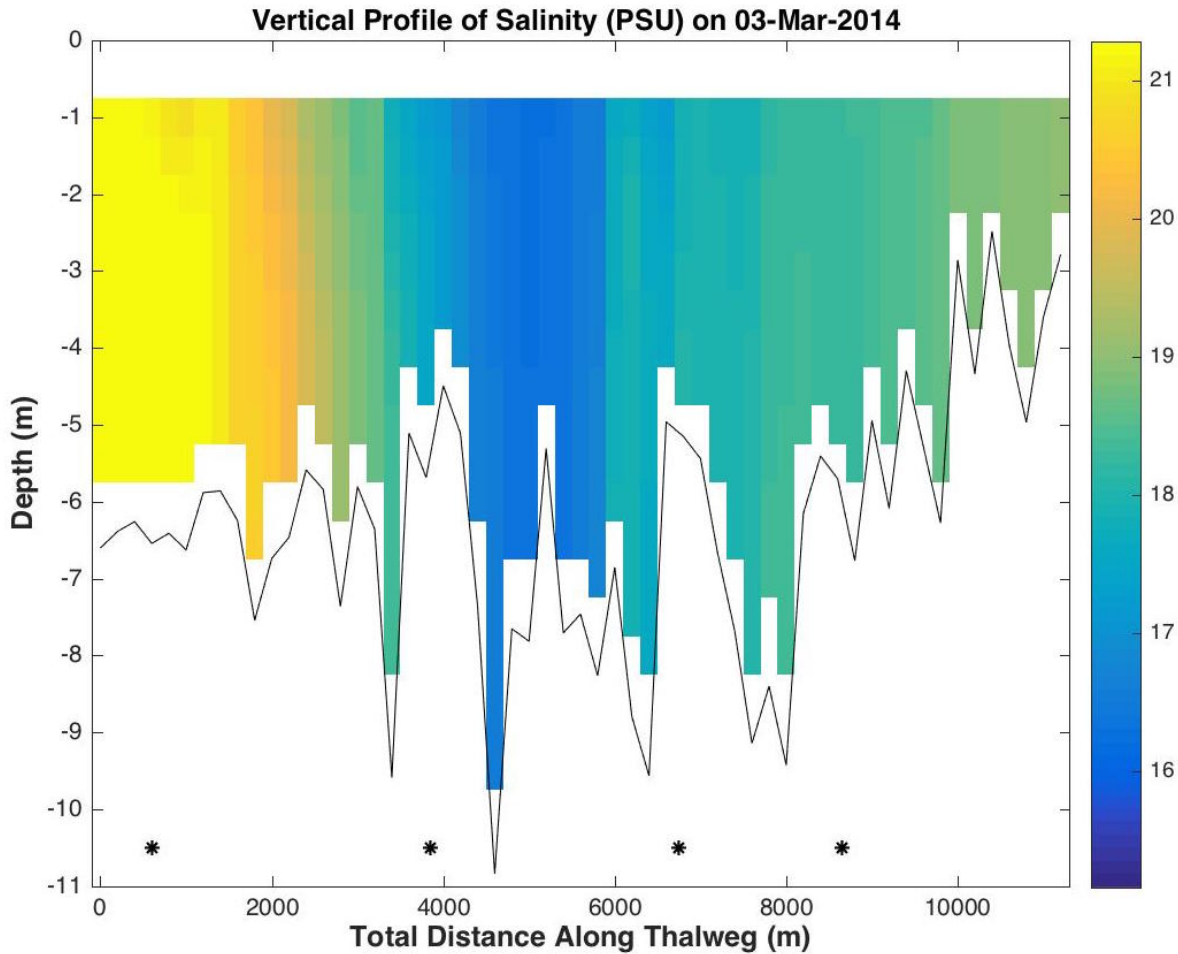


Figure 4.3: A vertical profile of model salinity along the thalweg demonstrating the negative estuary effect in the mid to upper Duplin, with the locations of the 4 cross sections identified by asterisks.

After reviewing the discharge record for the Altamaha, it was determined that when *McKay* (2008) carried out the study in the upper Duplin there was a significant river discharge event that caused the observed reversal of the salinity gradient. This observation is the major motivation for a salt flux analysis in order to better understand how this negative estuary effect can influence the transport dynamics within this system.

## 4.2 METHODS

### 4.2.1 THEORETICAL FRAMEWORK

The subtidal or tidally averaged salt flux  $F_S$  is broken down into flux components representing the mean advective flux  $F_0$ , the flux due to the vertically and laterally sheared exchange flow  $F_E$ , and the tidal varying flux  $F_T$ . The equation for the subtidal salt flux  $F_S$  as defined by *Lerczak et al.* (2006) is

$$F_S = \langle \int v s dA \rangle \quad (4.1)$$

where,  $\langle \rangle$  represent a tidal filter to create tidally averaged quantities of sectionally integrated kinematic salt fluxes. Salinity is  $s$  (PSU) and the along channel flow is  $v$  ( $m s^{-1}$ ). The subtidal component of the volumetric flow rate ( $m^3 s^{-1}$ ) through the cross sectional area in question is represented by,

$$Q_F = \langle \int v dA \rangle \quad (4.2)$$

The tidally and sectionally averaged components for salinity  $s_0$  (PSU) and along channel flow  $v_0$  ( $m s^{-1}$ ) are defined as,

$$s_0 = \frac{\langle \int s dA \rangle}{A_0} \quad (4.3)$$

$$v_0 = \frac{\langle \int v dA \rangle}{A_0} = \frac{Q_F}{A_0} \quad (4.4)$$

where the tidally averaged component of the cross-sectional area is,

$$A_0 = \langle \int dA \rangle \quad (4.5)$$

The tidally averaged and sectionally varying components of the velocity and salinity at each grid cell are,

$$v_E = \langle v \rangle - v_0 \quad (4.6)$$

$$s_E = \langle s \rangle - s_0 \quad (4.7)$$

where the components  $v_E$  ( $m s^{-1}$ ) and  $s_E$  (PSU) are due to the estuarine exchange flow and include the lateral and vertical shear of the velocity along with the lateral and vertical

salinity gradients at each cross section. These components vary on sub-tidal timescales. The tidally and cross sectionally varying components of velocity and salinity at each grid cell are represented by  $v_T$  ( $m s^{-1}$ ) and  $s_T$  ( $PSU$ ),

$$v_T = v - v_0 - v_E \quad (4.8)$$

$$s_T = s - s_0 - s_E \quad (4.9)$$

These components vary over tidal timescales over each cross section.

Using the scheme described by (*Lerczak et al.*, 2006), the subtidal component of the salt flux  $F_S$  can be broken down into the three major components: the advective flux ( $F_0$ ), given by ( $Q_F s_0$ ), due to the average advective transport of salt across the cross sections, the exchange component of the subtidal salt flux ( $F_E$ ) due to shear dispersion which is a function of vertical and lateral shear transport, and the tidal salt flux ( $F_T$ ) due to tidal pumping. These fluxes are calculated using the parameters defined above and then sectionally integrated and tidally averaged,

$$F_S = \langle \int (v_0 + v_E + v_T)(s_0 + s_E + s_T) dA \rangle = \langle \int (v_0 s_0 + v_E s_E + v_T s_T) dA \rangle \quad (4.10)$$

$$= Q_F s_0 + F_E + F_T \quad (4.11)$$

According to *Lerczak et al.* (2006), terms with cross correlations from Equation (4.10),  $v_0 s_E$ ,  $v_0 s_T$ ,  $v_E s_0$ ,  $v_E s_T$ ,  $v_T s_0$ ,  $v_T s_E$ , are assumed to be zero because of the different spatial and temporal scales associated with each variable.

The first term given in Equation (4.11) is the advective flux ( $F_0$ ) and the next two terms together ( $F_E + F_T$ ) represents the dispersive flux. Given the longitudinal residual salinity gradient, the horizontal dispersion coefficient  $K_y$  ( $m^2 s^{-1}$ ) can be calculated. This is an important parameter to quantify in estuaries because it gives information about how scalars such as salt, pollutants, or even nutrients will spread throughout a system as a function of spatial velocity gradients (*Devkota and Fang*, 2015). The horizontal dispersion coefficient can be calculated from the dispersive flux term using the equation described by *Devkota and*

Fang (2015),

$$-A_0(y)K_y(y)\frac{\partial s_0}{\partial y} = F_E + F_T \quad (4.12)$$

where our sign convention is such that the positive along channel y-axis is directed into the Duplin (northward) and  $\partial s_0/\partial y < 0$ , for a positive estuary.

The one dimensional along-estuary salt conservation equation is,

$$\frac{\partial s}{\partial t} + \frac{\partial(vs)}{\partial y} = 0 \quad (4.13)$$

The tidally averaged and sectionally integrated salt balance then becomes

$$A_0 \frac{\partial s_0}{\partial t} = \frac{-\partial F_S}{\partial y} \quad (4.14)$$

If the domain is broken up into a box model, then this equation states that when more salt is leaving the box than entering ( $\partial F_S/\partial y > 0$ ) then the salinity ( $s_0$ ) in the box will decrease. When more salt enters the box than is leaving ( $\partial F_S/\partial y < 0$ ),  $s_0$  will increase.

#### 4.2.2 DATA PROCESSING

For all analysis described in this chapter, the positive y-axis is directed northward, or into the estuary through the mouth of the Duplin and through the open boundary. This sign convention may be opposite to other estuarine studies. This section describes the methods for obtaining subtidal and tidal velocities and salinities using the mathematical framework described in the previous section for each cross section. The four cross sections used for this analysis are identified on an inundation field at flood tide in Figure 4.4 and were chosen to have a fairly straight section along the channel to minimize secondary circulation (cross channel flows) due to channel curvature. They are numbered starting at the most southern cross section and counting up in the northward direction.

Cross section 1 (CS1) is located very close to Marsh Landing. This cross section has 50  $(x, y)$  positions spaced at approximately 5 *m* apart with a total length of approximately 250 *m* across the channel. Cross section 2 (CS2) is located between Barn Creek and Lumber

### Inundation (m) on Slack High Tide with Cross Sections

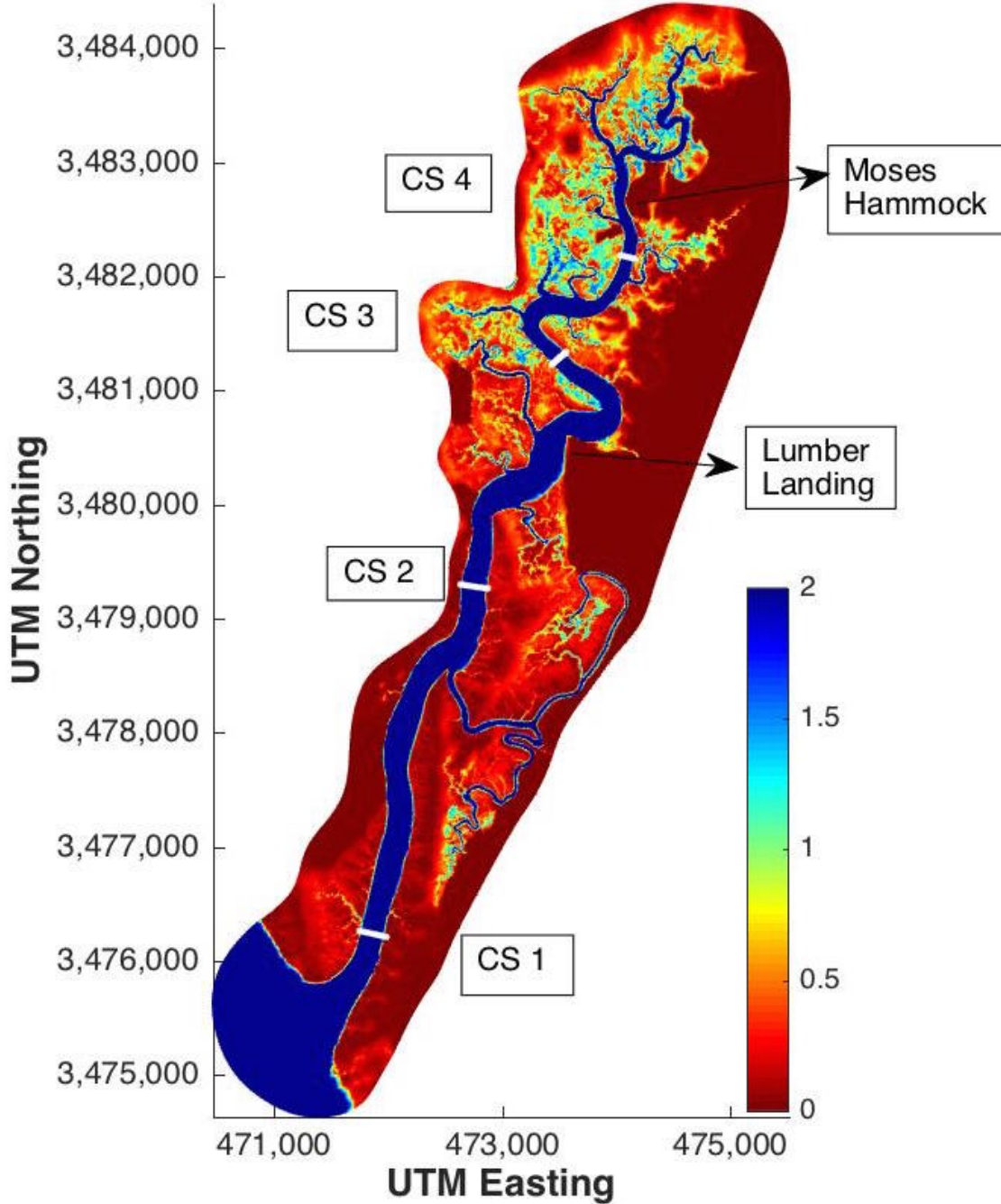


Figure 4.4: The locations of cross sections with inundation at a flood tide.

Landing. This cross section also consists of 50  $(x, y)$  positions and is approximately 250  $m$  wide with similar spacing. Cross sections 1 and 2 represent the lower to mid section of the Duplin where inundation is less than 0.5  $m$  in adjacent marsh. Cross section 3 (CS3) is north of Lumber Landing and is made up of 36  $(x, y)$  positions. The total length is approximately 175  $m$  across the channel with a 5  $m$  spacing between each point. Cross section 4 (CS4) is just south of Moses Hammock and is made up of 29  $(x, y)$  positions. This cross section is approximately 140  $m$  wide with a 5  $m$  spacing between  $(x, y)$  positions. Cross sections 3 and 4 represent the mid to upper regions showing a distinct difference in inundation patterns where adjacent marsh can have over 1  $m$  of water.

For each cross section, the along channel velocity component and salinity were interpolated to vertical depth bins ranging from 1 to -10  $m$  at an increment of every 0.5  $m$  and interpolated along the cross section every 5  $m$ . An example of the along channel velocity from cross section 1 on 3/3/2014, which is during a period of HRD from the Altamaha, and during the flood tide can be seen in Figure 4.5, where the vertical and lateral shear of the velocity gradient can be seen. This shear contributes to the exchange component of the flux ( $F_E$ ). The maximum flow is on the eastern side of the channel. We expect to see some cross sectional variability because of the sinuous nature of the Duplin. The cross sectional salinity at cross section 1 for the same time period can be seen in Figure 4.6, which gives an example of the vertical and lateral salinity gradients that can exist. Note that fresher water is on the eastern side of the cross section associated with the faster moving flow.

These parameters were calculated at 20 minute increments, which is the rate at which the model output is stored, at all cross sections for the year 2014. With the velocity and salinity output, the residual (Equations 4.3 and 4.4), exchange (Equations 4.7 and 4.6), and tidal components (Equations 4.9 and 4.8) of salinity and velocity, are then calculated. All data relating to salinity from 7/27/2014 to 8/1/2014 was removed due to suspect salinities at the GCE6 station during this time period. A 40-hour lowpass digital filter with a hamming window function that can deal with not a numbers (NaN) in MATLAB (`ndnanfilter.m`) was

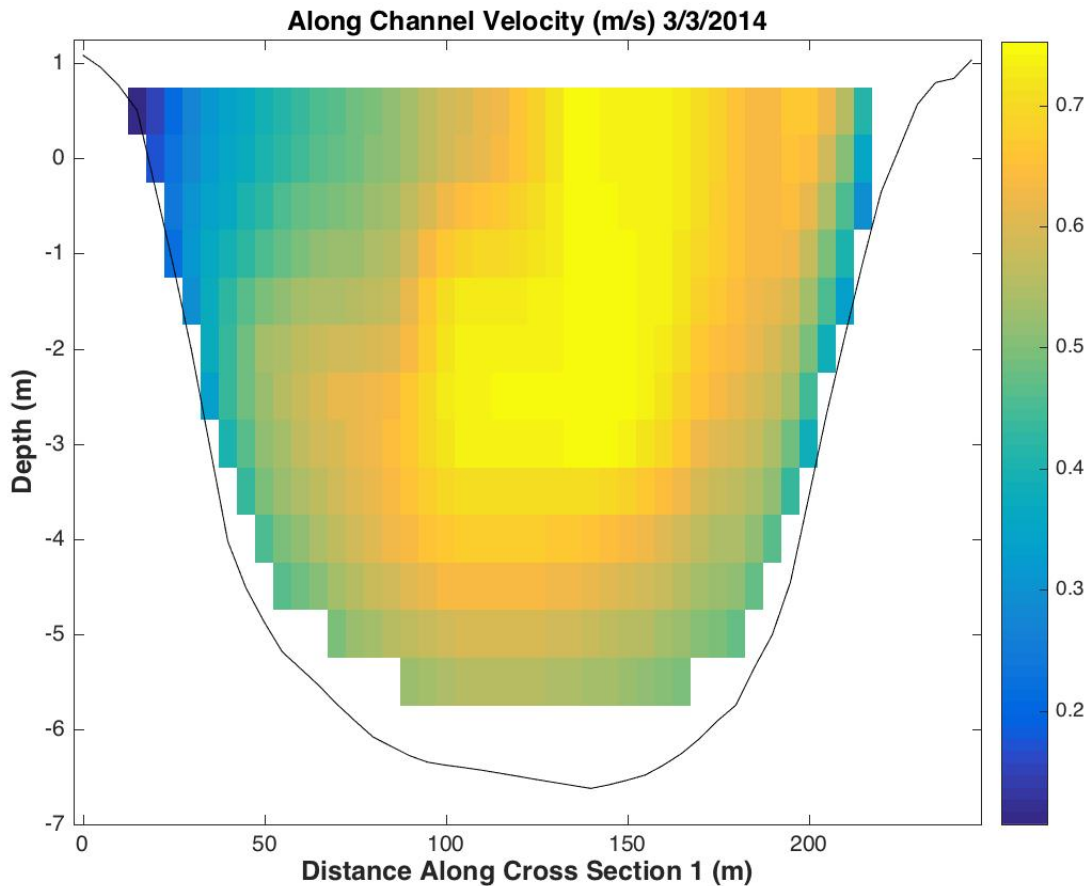


Figure 4.5: The along channel velocity at CS1 during the HRD period on a flood tide.

chosen to calculate tidally averaged quantities for  $v$  and  $s$  at each grid cell, which was needed to calculate exchange ( $v_E, s_E$ ) and tidal ( $v_T, s_T$ ) components of salinity and velocity. NaN's are present in the data because of the changing surface due to tides: at low water NaN's fill the cross section from 1 m to -1 m, but at high water data exists to 1 m elevation. A 3rd order 40 hr lowpass Butterworth filter was used for tidally averaging quantities when a sectional integration had already occurred as sectionally integrating removes NaN's. This type of filtering was applied to the residual quantities ( $v_0, s_0, A_0$ ) and flux quantities ( $F_0, F_E, F_T$ ).

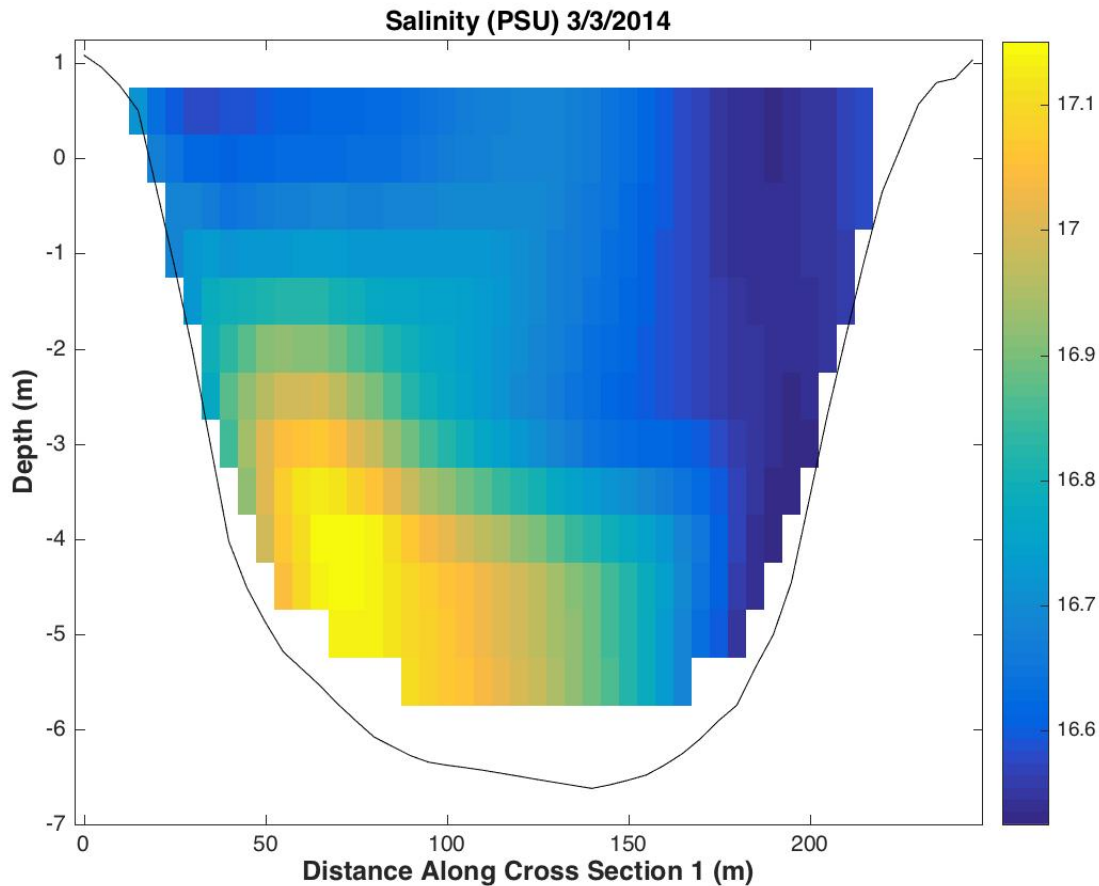


Figure 4.6: The cross sectional salinity at CS1 during the HRD period on a flood tide.

Figure 4.7 shows the residual components of the velocity, salinity, and area, which are tidally and sectionally averaged, at the first cross section. The residual component of velocity ( $v_0$ ) varies over a range of  $0.04 \text{ m s}^{-1}$  and oscillates between positive ( $+ 0.02 \text{ m s}^{-1}$ ) and negative ( $- 0.02 \text{ m s}^{-1}$ ), but is predominately negative implying net flow out of the estuary. The residual component of the salinity ( $s_0$ ) varies based on freshwater inputs from the Altamaha. There is a minimum of 13.8 PSU at the beginning of May, which coincides with the end of the HRD period. The maximum is 30 PSU and comes in November, during the LRD period. The residual area ( $A_0$ ) varies based on sea surface height and how much

inundation there is within the cross section and varies from 825 to 1000  $m^2$ . The residual area follows the same pattern as subtidal SSH from Marsh Landing shown in Figure 2.15, which is expected.

Figure 4.7 also displays the exchange and tidal oscillatory components of velocity and salinity ( $v_E, s_E, v_T, s_T$ ) at cross section 1. The exchange component of the velocity, which is tidally averaged and sectionally varying, is plotted for grid cells near the bottom of the cross section and near the surface of the cross section at approximately mid-channel at the deepest point. This figure illustrates that we generally have positive velocity at the bottom (flow into the estuary) and negative flows leaving the estuary at the surface layer. The exchange components of the salinity, which are tidally averaged and sectionally varying, are also shown at the deepest position, which is approximately mid-channel, along the cross section at the surface and bottom. There is saltier water ( $s_E > 0$ ) at the bottom layer and fresher water ( $s_E < 0$ ) at the top as would be expected for a classic estuarine exchange with a stratification of approximately 1 PSU over the depth range. The tidal components of the salinities and velocities, which are tidally and sectionally varying, are also shown. These components illustrate the tidal variations and show that tidal flows can exceed magnitudes of  $\pm 1 m s^{-1}$  and are strongly modulated by the spring/neap cycle. The tidal salinity can have variations as large as 10 PSU during the HRD period and are reduced to less than 5 PSU during the LRD discharge time period.

Figure 4.8 shows the residual components of the velocity, salinity, and area at the second cross section. The residual velocity ( $v_0$ ) oscillates over a more reduced range of  $0.03 m s^{-1}$  compared to CS1, and is predominately negative implying net outflow. The residual salinity ( $s_o$ ) varies between a range of 13 to 28 PSU. The minimum coincides with the period of HRD in early May and the maximum happens at the time of LRD in September. The residual area ( $A_o$ ) varies based on sea surface height and inundation patterns at the second cross section and  $A_0$  varies between 680 to 880  $m^2$ . Once again, the residual area closely follows the pattern of subtidal SSH variability.

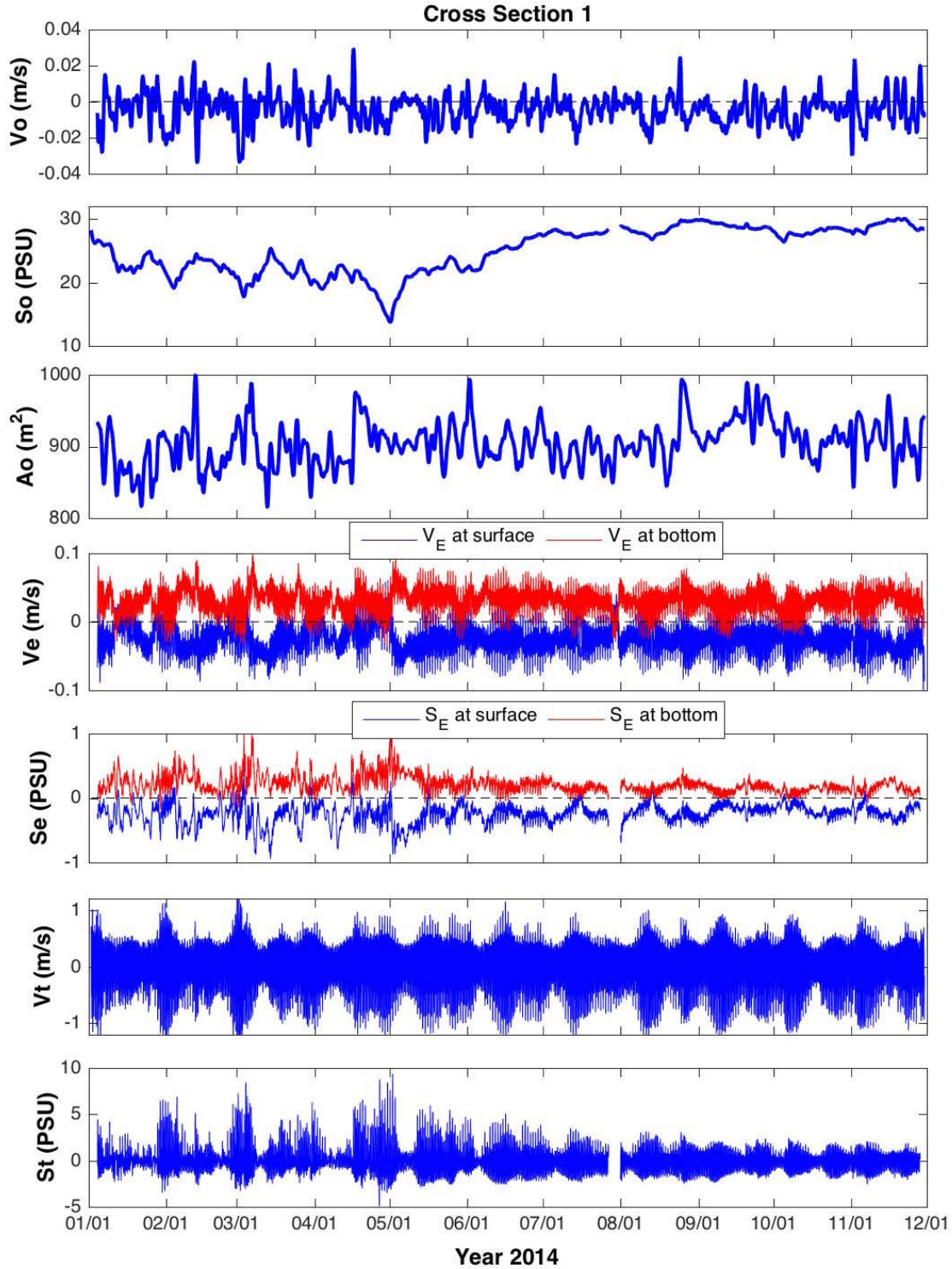


Figure 4.7: The residual, exchange, and tidal components of salinity and velocity at cross section 1.

Figure 4.8 also displays the exchange and tidal oscillatory components of velocity and salinity ( $v_E, s_E, v_T, s_T$ ) at the second cross section. The exchange component of the velocity is reduced by a factor of 2 compared to CS1 and this shows a noisier time series. The bottom is generally positive, if you average over the noise, showing that there is flow into the estuary. However, there are times throughout the year where this trend reverses. This is most pronounced during periods of HRD and can be seen in February, March, April, and May during the highest spring tides. The surface component of the exchange velocity oscillates between negative and positive and generally is opposite to the bottom flows. The exchange component of the salinity is generally always positive at the bottom layer showing higher salinity compared to the surface layer which is generally negative. This shows a stratification of approximately 0.6 PSU over the depth range with the bottom component showing greater salinity variation. The tidal oscillatory components of velocity and salinity are also shown but are reduced compared to CS1.

Figure 4.9 shows the depth averaged ( $\bar{v}$ ), tidally filtered velocity ( $\langle \bar{v} \rangle$ ) at the centroid of every tenth mesh element throughout the lower domain with cross sections 1 and 2 identified. This is during September, 2014 which is during the period of LRD. This figure identifies the patterns of net residual circulation in the lower Duplin. Flows at the first cross section are into the estuary on the eastern boundary and out of the estuary on the western boundary implying that the flood tide is strongest on the eastern side and the ebb tide is strongest on the western side. This trend is the same at the second cross section. This shows that the sectional average for the residual velocities at cross sections 1 and 2 are dominated by the ebb flows on the western side. A clockwise eddy over the deep hole at the mouth of Barn Creek can also be seen in this figure and shows that the model can be used to understand morphological features in the channel (a topic beyond the scope of this research project).

Figure 4.10 shows the residual components of the velocity, salinity, and area at the third cross section. It should be noted that CS3 separates the deeper marsh area in the mid to upper Duplin from the high marsh region in the mid to lower Duplin. The residual velocity

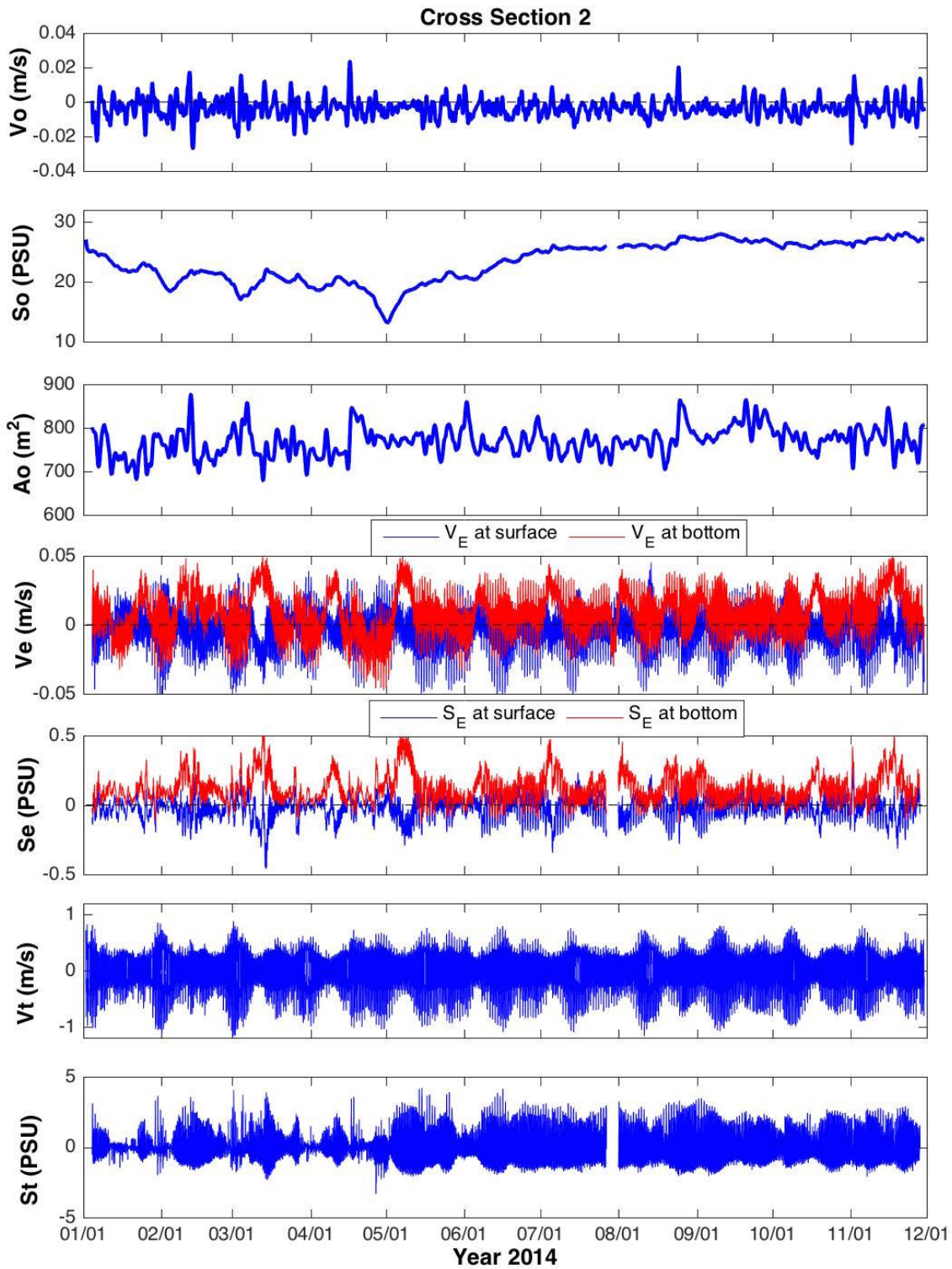


Figure 4.8: The residual, exchange, and tidal components of salinity and velocity at cross section 2. Residual area is also shown.

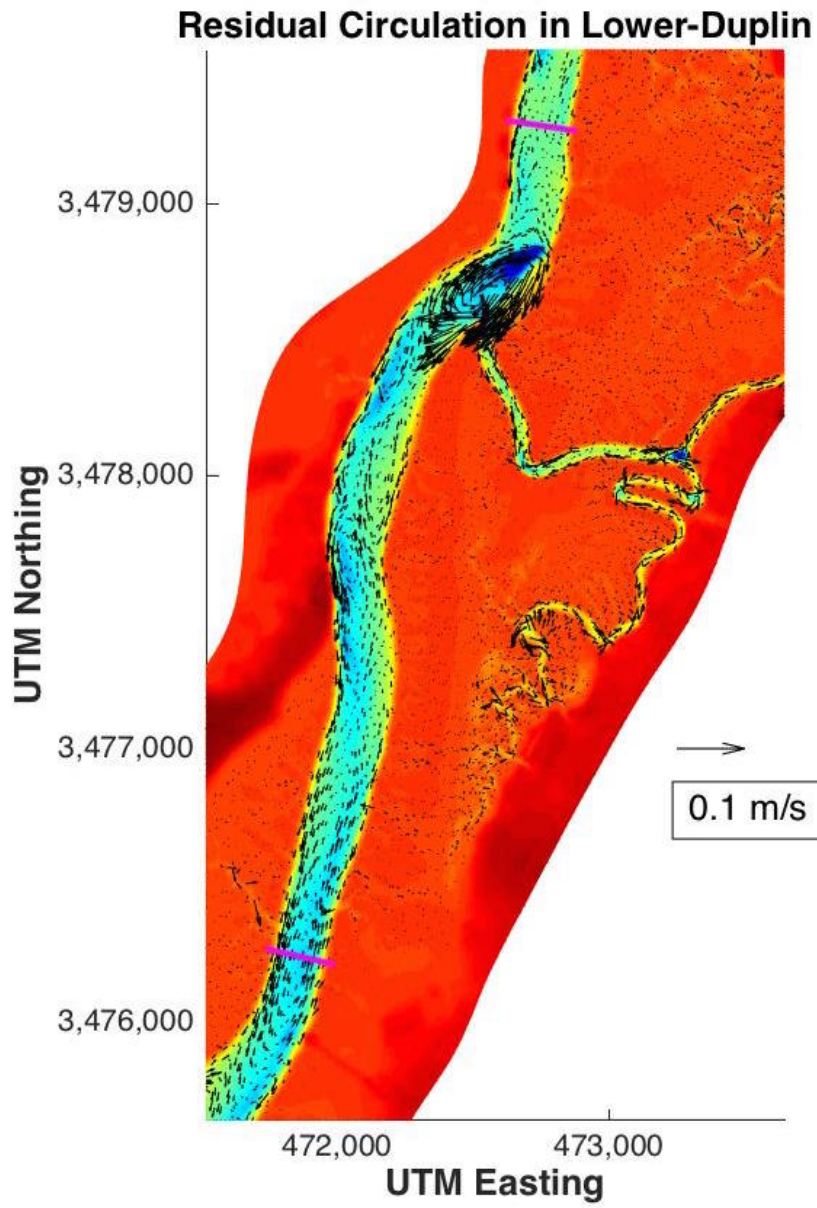


Figure 4.9: Residual circulation patterns in the lower Duplin plotted on the bathymetry (m) with cross sections 1 and 2 identified.

$(v_0)$  fluctuates between positive and negative over a reduced range of  $0.02 \text{ m s}^{-1}$  and is predominately positive in the second half of the year. The residual salinity ( $s_0$ ) also shows variability controlled by the freshwater discharge. The minimum is directly after the period of the highest river discharge at the start of May and is 14.2 PSU. The maximum of the residual salinity is in September during the period of LRD and is 26.5 PSU. The residual ( $A_0$ ) area fluctuates as a function of the tidal stage and level of inundation. These values range from 440 to  $570 \text{ m}^2$  showing that the cross sectional areas get progressively smaller as you move into the estuary. The residual area shows the same dependency on subtidal SSH discussed previously but the variability is reduced.

Figure 4.10 also displays the exchange and tidal components of velocity and salinity ( $v_E, s_E, v_T, s_T$ ) at cross section 3. The exchange velocity is reduced further and bottom and surface velocities fluctuate between negative and positive values throughout the year. The exchange component of the salinity is positive at depth, which means that saltier water moves according to  $v_E$  at depth. The surface exchange salinity is generally negative during the year, showing weak stratification between the two depths. The tidal components of salinity and velocity are further reduced in magnitude.

Figure 4.11 shows the residual components of the velocity, salinity, and area at the fourth cross section. The tidally and sectionally averaged velocity ( $v_0$ ), is positive for most of the year and varies over a range of  $0.02 \text{ m s}^{-1}$  implying a net flow into the upper reaches as will be explained. The residual salinity,  $s_0$ , follows a very similar pattern to all of the previous cross sections with a minimum of 14.6 PSU at the end of the HRD period and a maximum of 25.6 PSU during the LRD period. The residual area ( $A_0$ ) varies over a range of 290 to  $400 \text{ m}^2$  and is highly correlated with subtidal SSH as at all other cross sections.

Figure 4.11 also displays the exchange and tidal components of velocity and salinity ( $v_E, s_E, v_T, s_T$ ) at the fourth cross section. The surface component of the exchange velocity fluctuates between negative and positive. The bottom component of the exchange velocity is generally positive, except for at time points early in the year during the period of high river

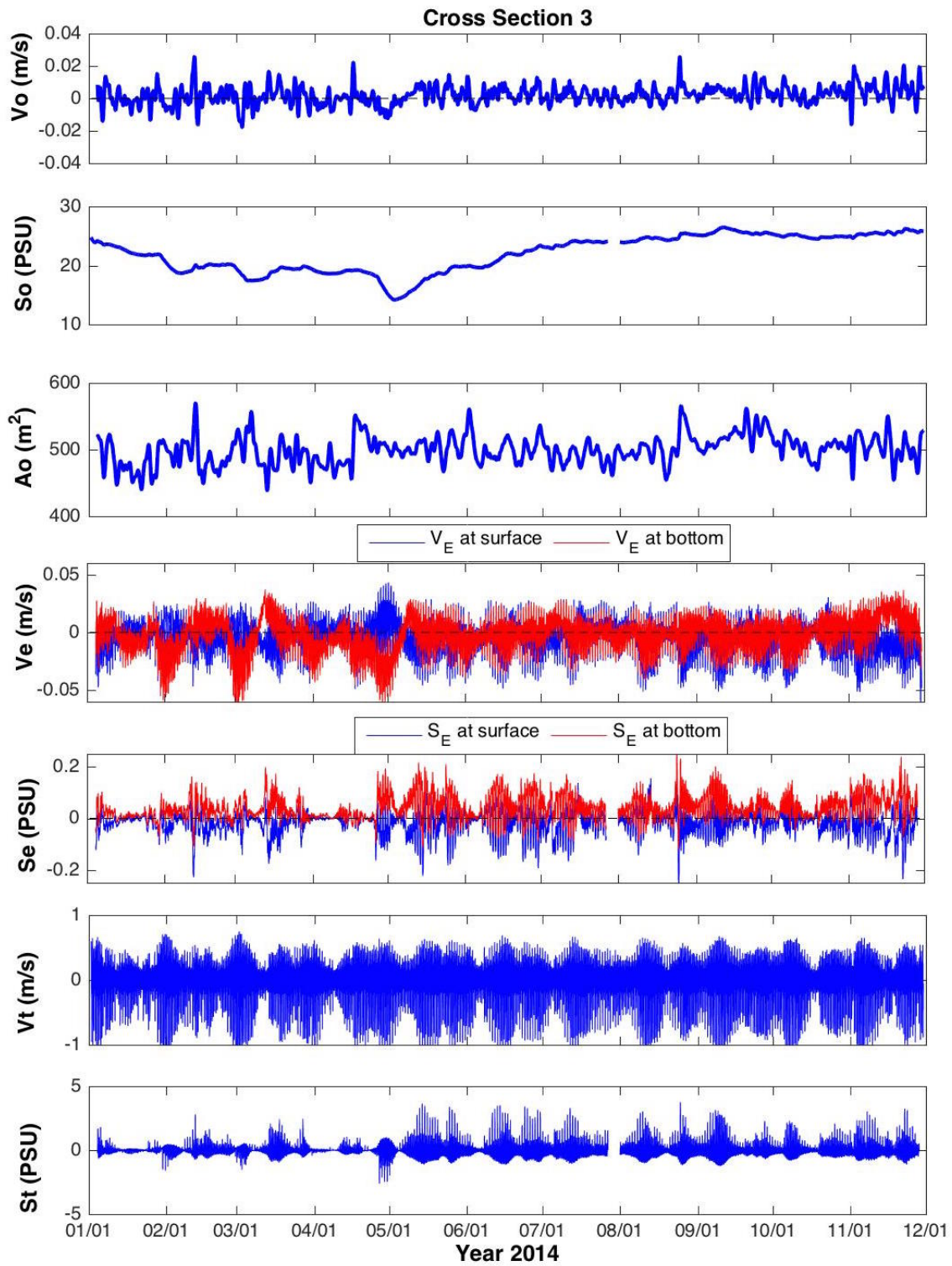


Figure 4.10: The residual, exchange, and tidal components of salinity and velocity at cross section 3. Residual area is also shown.

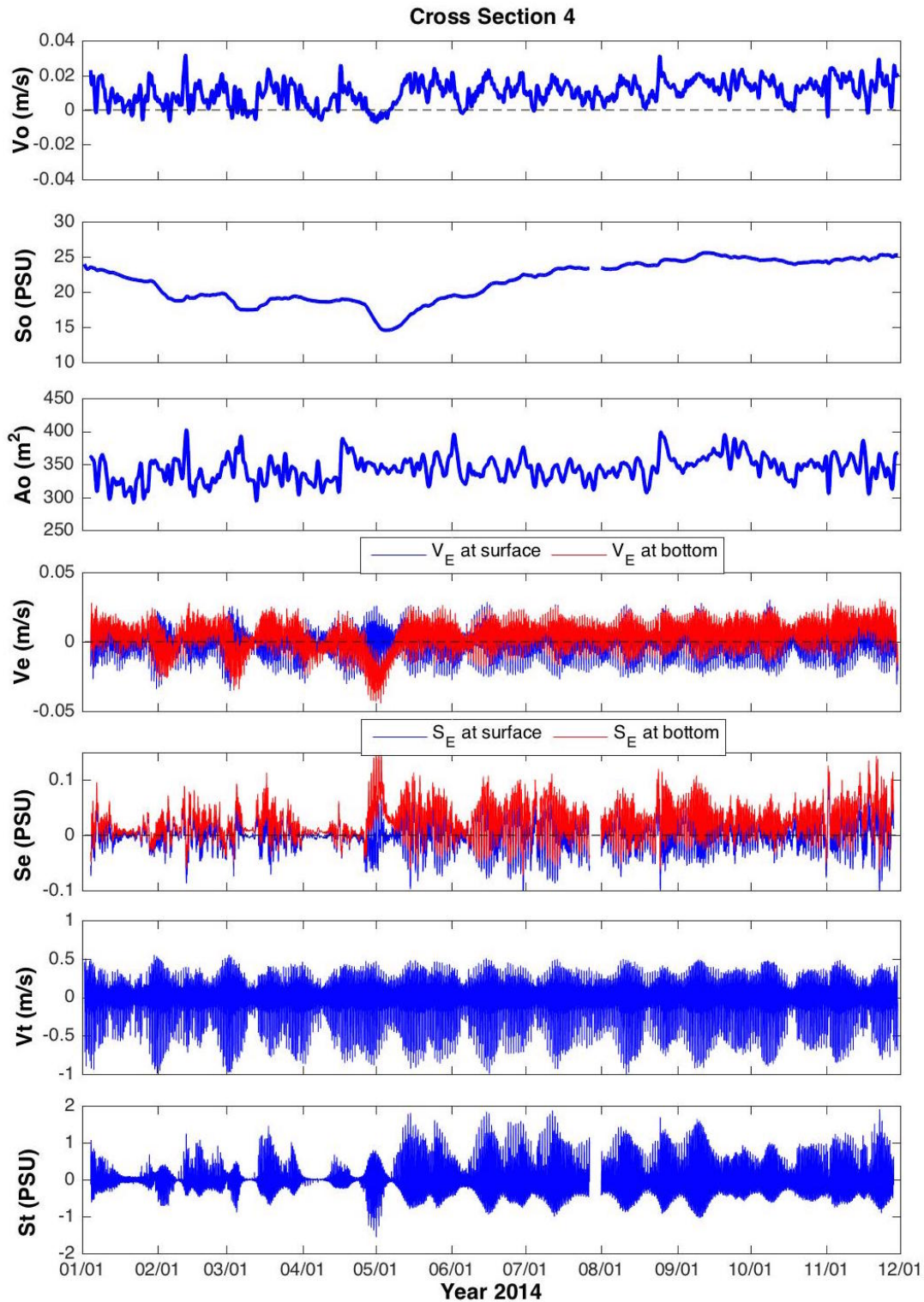


Figure 4.11: The residual, exchange, and tidal components of salinity and velocity at cross section 4. Residual area is also shown.

discharge. The exchange component of the salinity is generally positive at the bottom. The surface component of the exchange salinity is generally negative and the overall stratification is weak. The tidal component of the velocity varies over a range of  $1.5 \text{ m s}^{-1}$ . The tidal oscillatory component of the salinity varies over a range of 1-3 PSU.

Figure 4.12 shows the depth averaged ( $\bar{v}$ ) and tidally filtered velocity ( $\langle \bar{v} \rangle$ ) at every tenth element centroid in the upper Duplin. Cross sections 3 and 4 are also identified. This is during September 2014. This figure shows the net residual circulation patterns in the mid to upper Duplin. With regards to cross section 4, the residual velocity, ( $\langle \bar{v} \rangle$ ), is generally always positive. The net advective transport in the main channel is into the estuary, while the advective transport out of the estuary generally takes place on the western side of the marsh showing a counterclockwise circulation in the upper Duplin. This is also the case at cross section 3 with advective transport out of the estuary taking place in the marsh on both sides of the channel and advective transport into the estuary happening in the main channel. This sheds light on why  $v_0$  is positive at cross sections 3 and 4 and why advective flux ( $F_0$ ), which will be quantified in the next section, is positive or into the estuary at the third and fourth cross section. This marsh circulation shows the complexities of using salt flux decomposition in a marsh dominant system like the Duplin.

The horizontal salinity gradient ( $\partial s_0 / \partial y$ ) was approximated by calculating the slope of a fifth order polynomial fitted to the curve of the depth averaged and tidally filtered salinity ( $\langle \bar{s} \rangle$ ) as a function of distance along the thalweg of the Duplin. Figure 4.13 shows the salinity ( $\langle \bar{s} \rangle$ ) as a function of distance along the thalweg at two different time periods. The colored dots represent the horizontal distances where the cross sections are located. At the first time point in February, the salinity along the thalweg is as expected for a typical estuary, which is from salty at the mouth to fresh at the head of the estuary ( $\partial \langle \bar{s} \rangle / \partial y < 0$  at all cross sections). The salinity measured in March illustrates a reversal of the salinity gradient from fresh to salty water between the second and fourth cross sections ( $\partial \langle \bar{s} \rangle / \partial y > 0$ ), or the

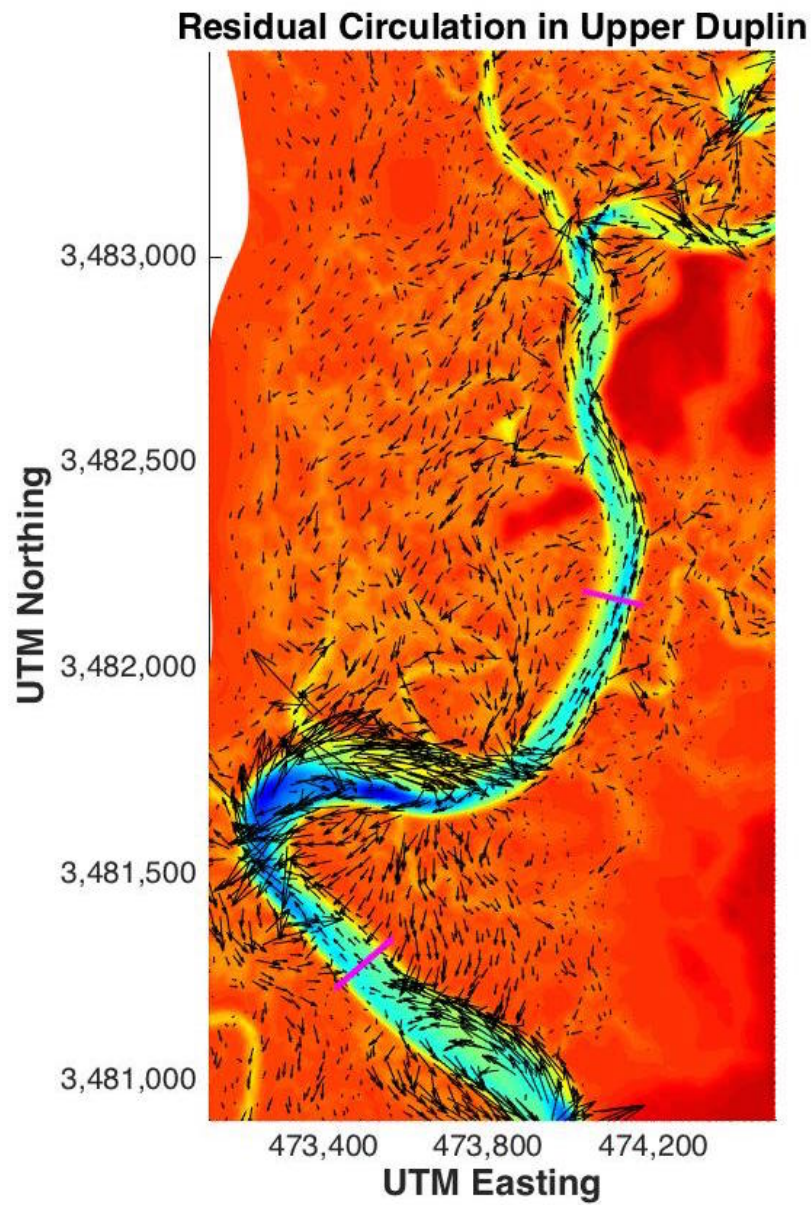


Figure 4.12: Residual circulation patterns in the upper Duplin plotted on the bathymetry (m) and showing cross sections 3 and 4.

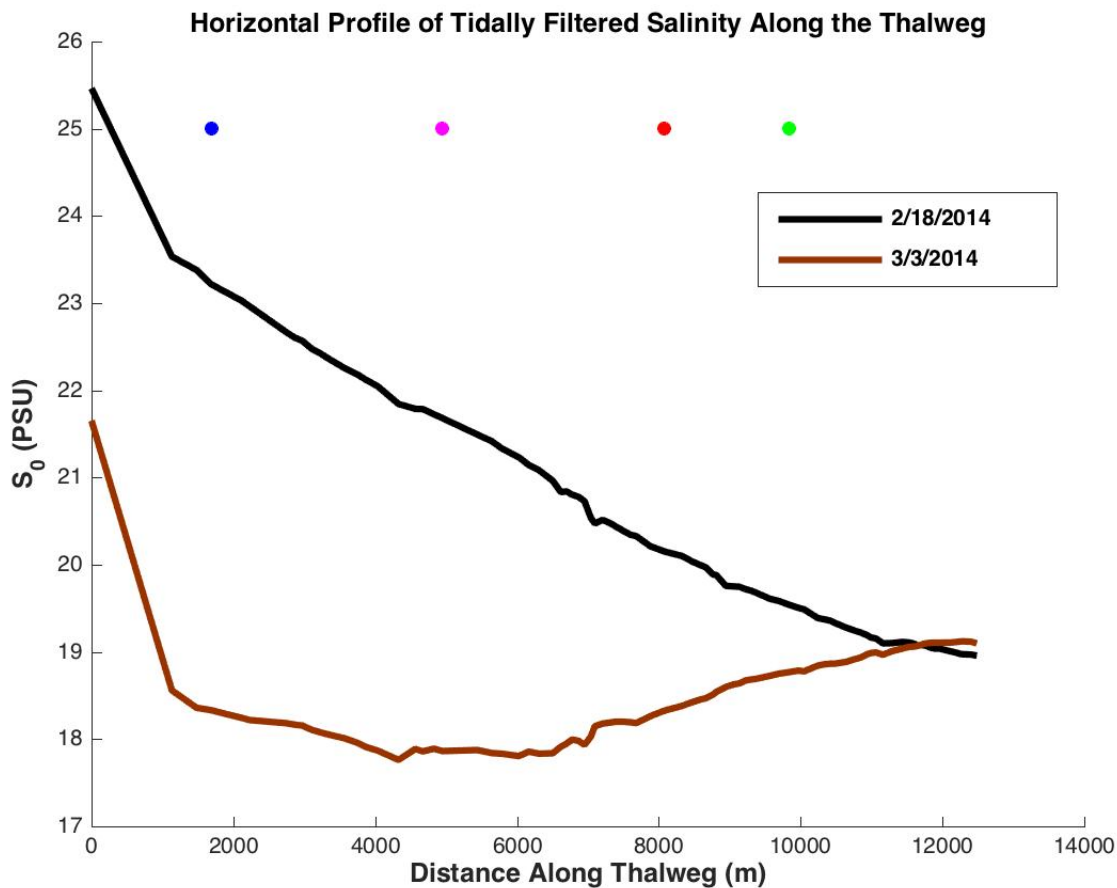


Figure 4.13: An example of depth averaged salinity as a function of distance along the thalweg for two different river discharge times.

negative estuary effect described previously. This time period coincides with a large pulse of freshwater associated with the Altamaha River.

### 4.3 RESULTS AND DISCUSSION

All parameters were calculated at 20 minute increments, which is the rate at which the model output is stored, at all cross sections for the year 2014. The residual, exchange, and tidal oscillatory fluxes were then calculated following the mathematical methods described in the

previous section. The units for the fluxes are given in ( $PSU\ m^3\ s^{-1}$ ), which can be considered to be ( $kg\ s^{-1}$ ), due to the fact that fluxes scaled by the density will change the numbers by 3% at the most. The dispersive flux ( $F_E + F_T$ ) and the horizontal salinity gradient are then used to calculate the horizontal dispersion coefficient. The horizontal dispersion coefficient ( $K_y$ ) is calculated with Equation (4.12) and is cleaned by removing data where the horizontal salinity gradient becomes close to zero and causes the horizontal dispersion coefficient to become very large in the negative and positive directions. Negative dispersion coefficients are also removed indicating a time lag between  $F_E + F_T$  and  $\partial\langle \bar{s} \rangle/\partial y$ .

Figure 4.14 shows all kinematic flux components at cross section 1. The tidal oscillatory component of the flux ( $F_T$ ), which is dependent on temporal correlations between the tidal velocity and salinity, oscillates between negative and positive values early in the year, which is during the period of HRD. This can be interpreted to show that during periods where there are large pulses of freshwater input at the mouth of the Duplin, the tidal component of the flux at the first cross section will switch between moving salt in and out of the estuary. Later in the year during the period of LRD, the tidal flux is always positive, or always moving salt into the estuary. The exchange flux ( $F_E$ ), which is dependent on vertical and lateral gradients is generally always positive. This means that the estuarine circulation moves salt into the estuary. The values are smaller than the tidal effects as this system is generally well mixed. Exchange fluxes ( $F_E$ ) during HRD are generally higher than LRD because of higher stratification. Tidal flux ( $F_T$ ) dominates exchange flux ( $F_E$ ) and thus controls the dispersive flux. The residual flux ( $F_0$ ) is the largest component of the overall flux and varies from positive to negative throughout the year but is mostly negative implying an outflow of salt. The advective transport dominates over the dispersive transport so that the total subtidal salt flux ( $F_S$ ) is heavily influenced by this term. It can be interpreted that the overall movement of salt at this cross section is out of the estuary. The salt flux at the first cross section is very variable though, and its variability is dominated by the net outflow velocity.

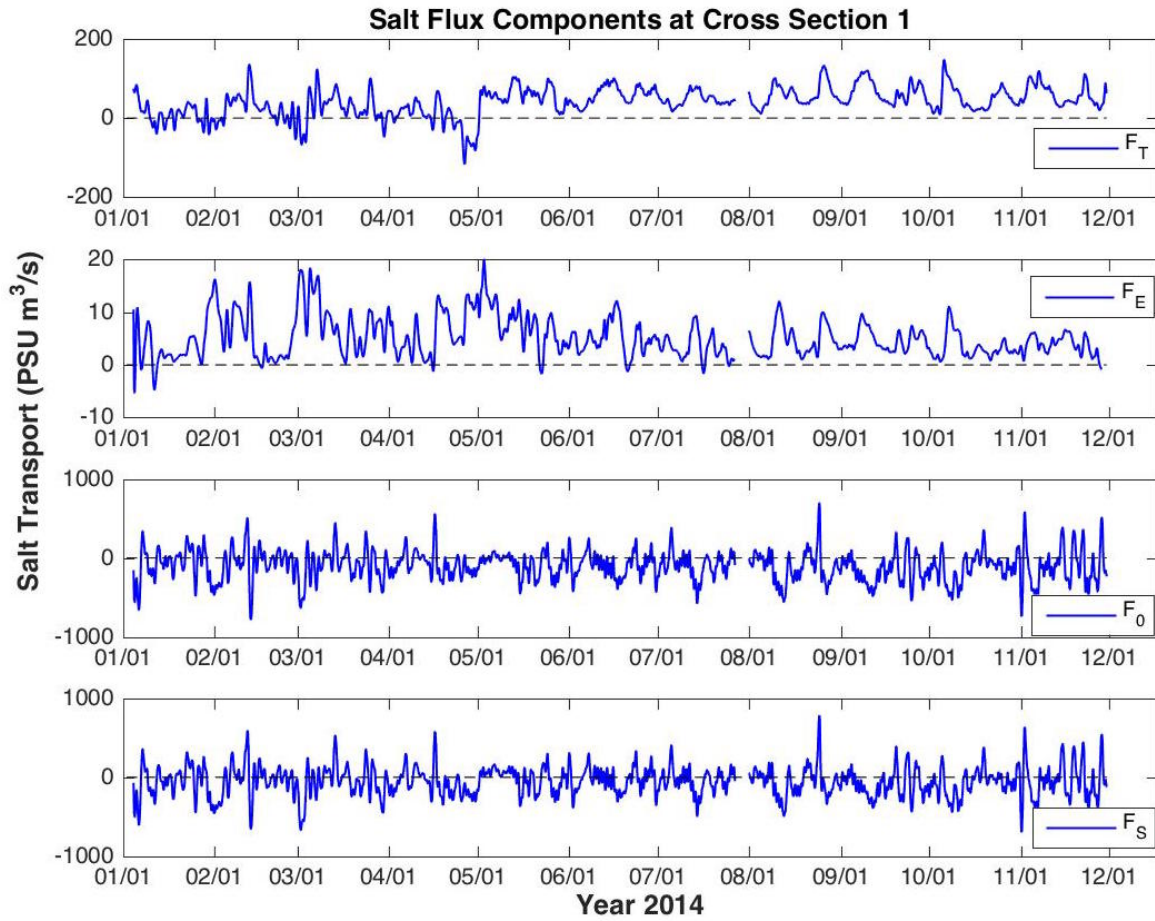


Figure 4.14: Tidal, exchange, residual, and total salt fluxes shown at CS1.

Figure 4.15 displays the parameters used to calculate the horizontal dispersion using Equation (4.12). These are the sum of the exchange and tidal oscillatory fluxes ( $F_E + F_T$ ), or the dispersive fluxes, and the horizontal salinity gradient ( $\partial\langle \bar{s} \rangle/\partial y$ ) at cross section 1. The dispersive flux is always positive during the LRD period later in the year, but oscillates between negative and positive during the HRD period. The dispersive movement of salt can be out of the estuary when freshwater pulses from the Altamaha dominate. The horizontal salinity gradient is almost always negative at the first cross section. This means that the gradient is from salty to fresh in this location.

The horizontal dispersion coefficient ( $K_y$ ) ranges from 0 to  $175 \text{ m}^2 \text{ s}^{-1}$  during the HRD period from January to May, with an outlier event with a coefficient of  $500 \text{ m}^2 \text{ s}^{-1}$  that occurs when the salinity gradient goes to zero. Later in the year during the period of LRD, where salty water dominates at the mouth of the Duplin, the dispersion coefficient oscillates according to the spring/neap cycle with values exceeding  $200 \text{ m}^2 \text{ s}^{-1}$ . The dispersive movement of salt is higher during this LRD period. The pattern of horizontal dispersion becomes much more periodic after the period of HRD. The spring/neap cycle is denoted on the figure with circles representing spring tides and asterisks representing neap tides.

Figure 4.16 shows all kinematic flux components at cross section 2. The axes are different from the previous cross section due to reduced magnitudes by a factor of 3. The tidal oscillatory component of the flux ( $F_T$ ) varies from -50 to  $50 \text{ PSU m}^3 \text{ s}^{-1}$ . The tidal flux ( $F_T$ ) is generally positive for the year 2014, except for specific time periods during the HRD where it becomes negative during large pulses of freshwater in February, March, and April. The exchange flux ( $F_E$ ) ranges from -10 to  $10 \text{ PSU m}^3 \text{ s}^{-1}$  and is generally negative early in the year during the HRD period until May. After this point, the exchange flux becomes generally positive when there is LRD. Tidal Flux ( $F_T$ ) still dominates the exchange flux ( $F_E$ ) and thus controls the dispersive flux, but the difference isn't as large as at the first cross section. The residual flux ( $F_0$ ) varies from -500 to  $500 \text{ PSU m}^3 \text{ s}^{-1}$  and dominates the overall subtidal flux. It is generally negative throughout the year, meaning that advective

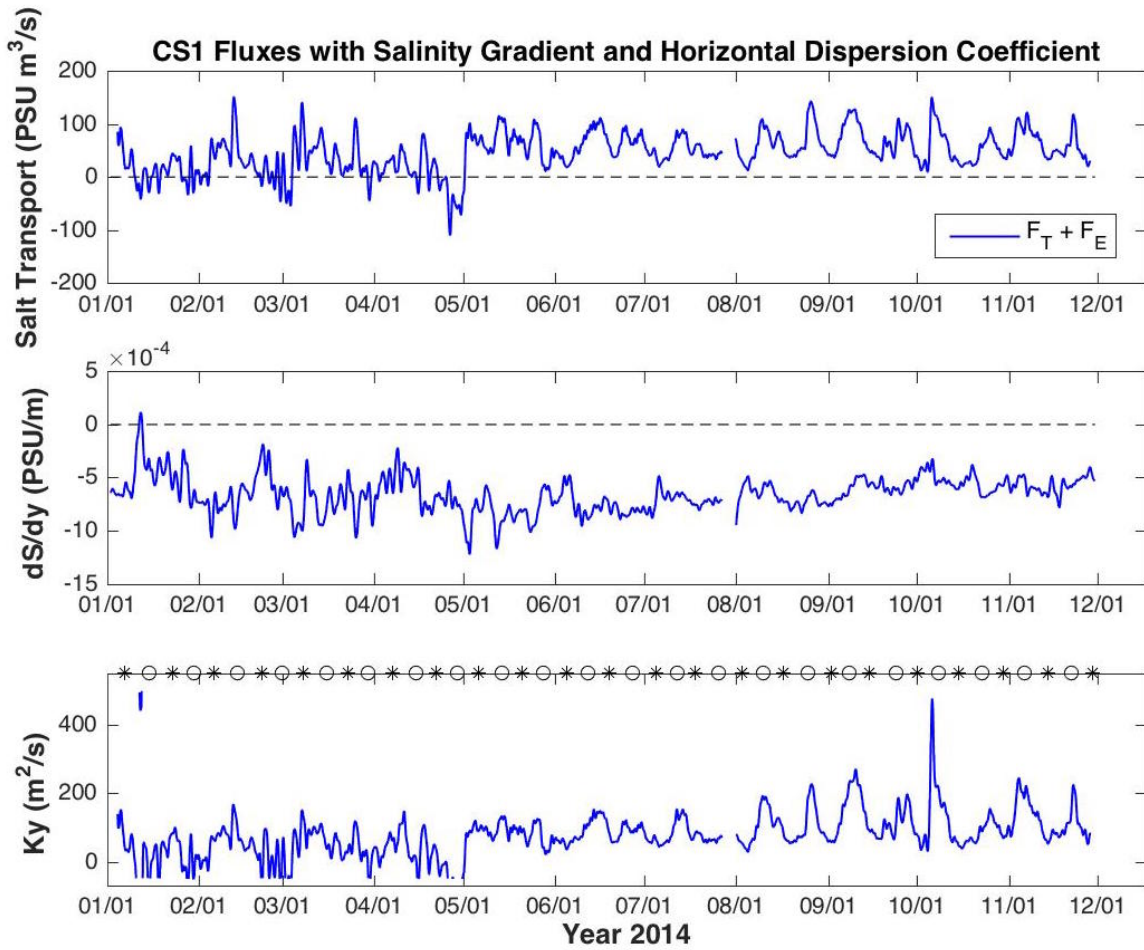


Figure 4.15: (upper panel) The sum of exchange and tidal oscillatory flux. (middle panel) The horizontal salinity gradient. (lower panel) The horizontal dispersion coefficient at CS1 with spring tides indicated by a circle and neap tides indicated by an asterisk.

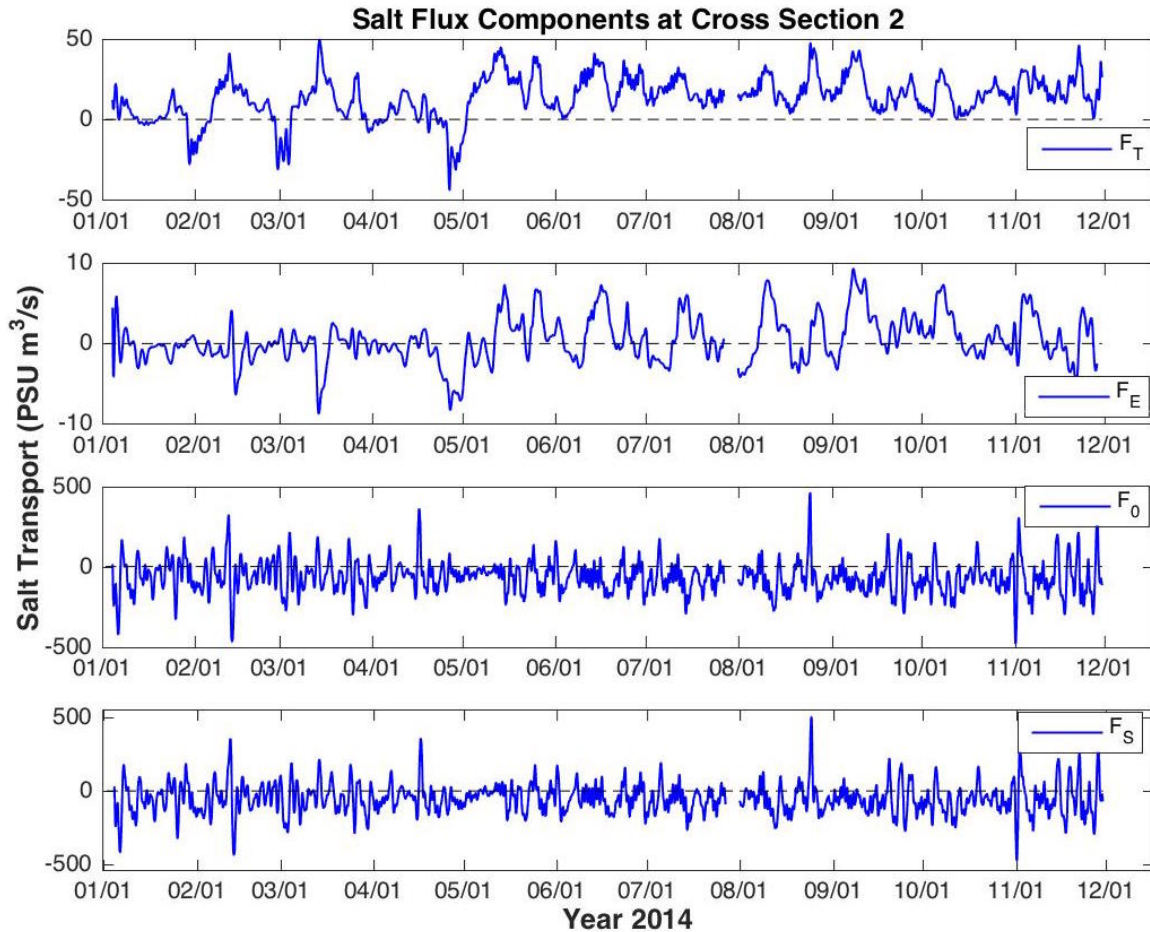


Figure 4.16: The tidal, exchange, residual, and total salt flux, respectively at CS2.

transport moves salt out of the estuary for the year 2014 at the second cross section. There are many points where this component is positive throughout the year, which corresponds to times of high inundation, but on average the residual flux is negative for this year. The total subtidal salt flux ( $F_S$ ) follows the residual salt flux very closely and has the same overall trends. From Equation (4.14), 56% ( $R=0.75$ ) of the time rate of change of salinity variability can be explained by the along channel salt flux gradient ( $\partial F_S/\partial y$ ) between cross section 1 and 2.

Figure 4.17 displays the sum of the exchange and tidal oscillatory fluxes, or dispersive flux, and the horizontal salinity gradient needed to calculate  $K_y$ . The trends at cross section 2 are very similar to the trends at the first cross section since the dispersive flux is always positive after the period of HRD later in the year. The sum is negative at certain points during the HRD period, January through April. This coincides with the largest pulses of freshwater from the Altamaha extending to cross section 2. The horizontal salinity gradient is always negative later in the year during the period of LRD, or after May 1. However; during the period of HRD, the salinity gradient will oscillate from negative to positive at time points that coincide with large pulses of freshwater discharge from the Altamaha River. Refer back to Figure 2.6 (lower panel) for an illustration of the patterns of river discharge. This is the negative estuary effect, which occurs when the salinity goes from fresh to salt in the positive or northward direction. This effect is prominent at the second cross section during times of HRD for the year.

The horizontal dispersion coefficient varies from 0 to  $300 \text{ m}^2 \text{ s}^{-1}$ , which is the maximum, during the HRD period. Horizontal dispersion is much more variable during this time period at the second cross section due to the freshwater inputs and the changing salinity gradient. After the HRD period ends, the patterns of horizontal dispersion become much more regular and vary on spring/neap timescales, ranging from 0 to  $120 \text{ m}^2 \text{ s}^{-1}$ , which is very similar to the patterns at the first cross section.

Figure 4.18 shows all kinematic flux components at cross section 3. The tidal oscillatory component of the flux is generally always positive throughout the whole year of 2014. It becomes slightly negative early in the year during the HRD period at times of the largest freshwater pulses from the Altamaha that extends to this cross section. The tidal flux ranges from -8 to  $22.5 \text{ PSU m}^3 \text{ s}^{-1}$ . The exchange component of the flux is also generally positive for the whole year except when HRD events occur. It ranges from -12.4 to  $5.4 \text{ PSU m}^3 \text{ s}^{-1}$ . During these high river pulses, both terms become negative indicating that the movement of salt due to temporal correlations between tidal velocity and salinity and between vertical

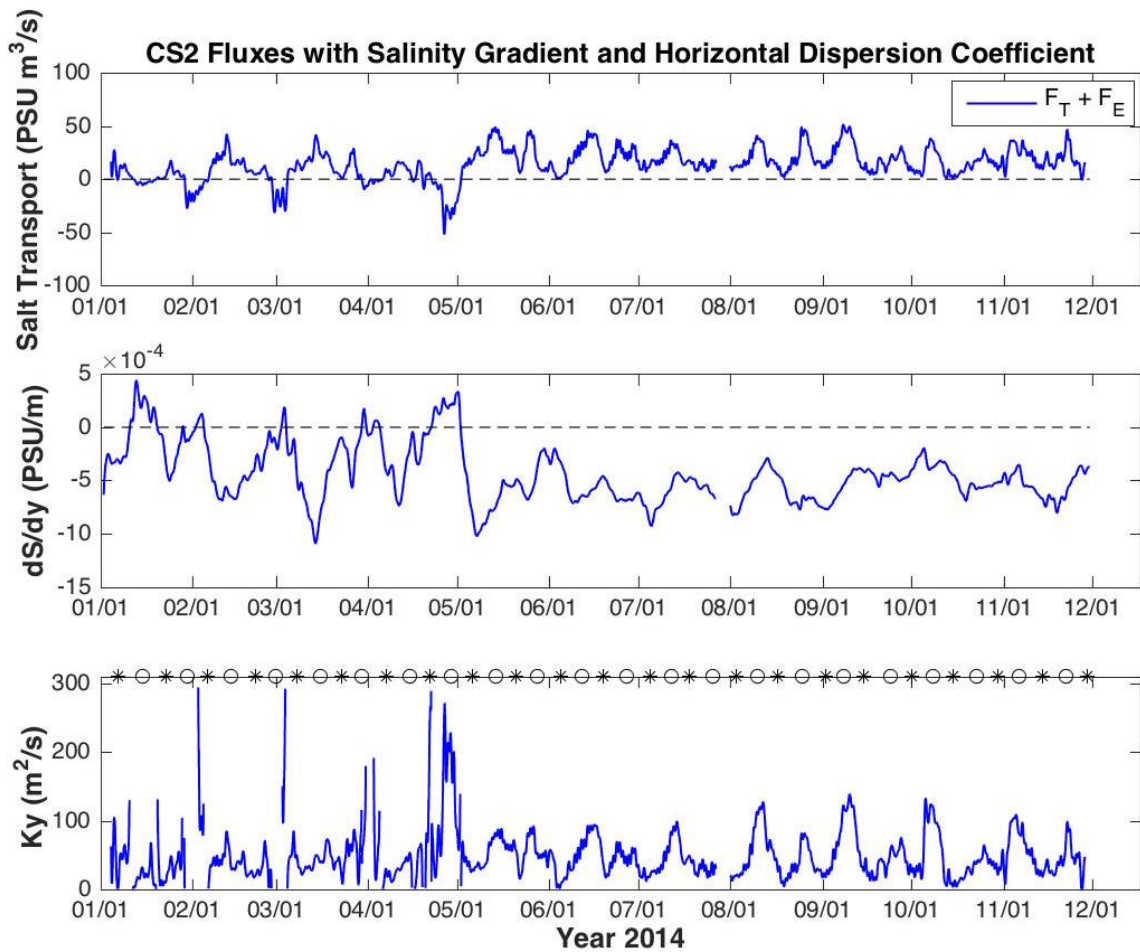


Figure 4.17: (upper panel) The sum of exchange and tidal oscillatory flux. (middle panel) The horizontal salinity gradient. (lower panel) The horizontal dispersion coefficient at CS2 with spring tides indicated by a circle and neap tides indicated by an asterisk.

and lateral shear (exchange) becomes negative causing a freshening of the estuary. Tidal flux ( $F_T$ ) also dominates exchange flux ( $F_E$ ) and thus controls the dispersive flux. The residual flux or flux due to advective transport oscillates between positive and negative early in the year and becomes generally positive later in the year when the river discharge is low and inundation is high. It ranges from -190 to 350  $PSU m^3 s^{-1}$ . This net northward transport in the channel is presumably balanced by the net residual outflow over the marsh as described in Figure 4.12. The added complication of marsh outflow implies that the advective flux is not accurately represented by confinement to the channel, thus careful interpretation of  $F_S$  is needed as it will not be able to predict how salinity varies in the mid to upper reaches of the Duplin. It should also be noted that all of the fluxes are becoming smaller in magnitude through the progression of the cross sections.

Figure 4.19 displays the parameters used to calculate the horizontal dispersion. The sum of the tidal oscillatory and exchange fluxes are generally always positive with the exception of the time periods of large fresher water originating from the Altamaha. This means that dispersion generally moves salt into the estuary in the positive north direction at this cross section, except when there are large freshwater pulses. The horizontal salinity gradient is generally always negative but on occasion it becomes positive at these same time points of high riverine freshwater pulses. During these times, the Duplin displays the negative estuary effect, or is an estuary where the salinity gradient is from fresh to salty in the direction from the mid to upper reaches and is only seen during the highest pulses of freshwater input. The horizontal dispersion coefficient ranges from 0 to 300  $m^2 s^{-1}$  and is most variable early in the year during the period of HRD. After the HRD period ends, horizontal dispersion becomes much more regular and varies over a smaller range and on more predictable tidal time scales. The variation starts to follow the spring/neap cycle with higher values of about 50  $m^2 s^{-1}$  on spring tides and lower values of about 0  $m^2 s^{-1}$  on the neap tides. This is very similar to what has been shown at the previous two cross sections, so it is shown once again that

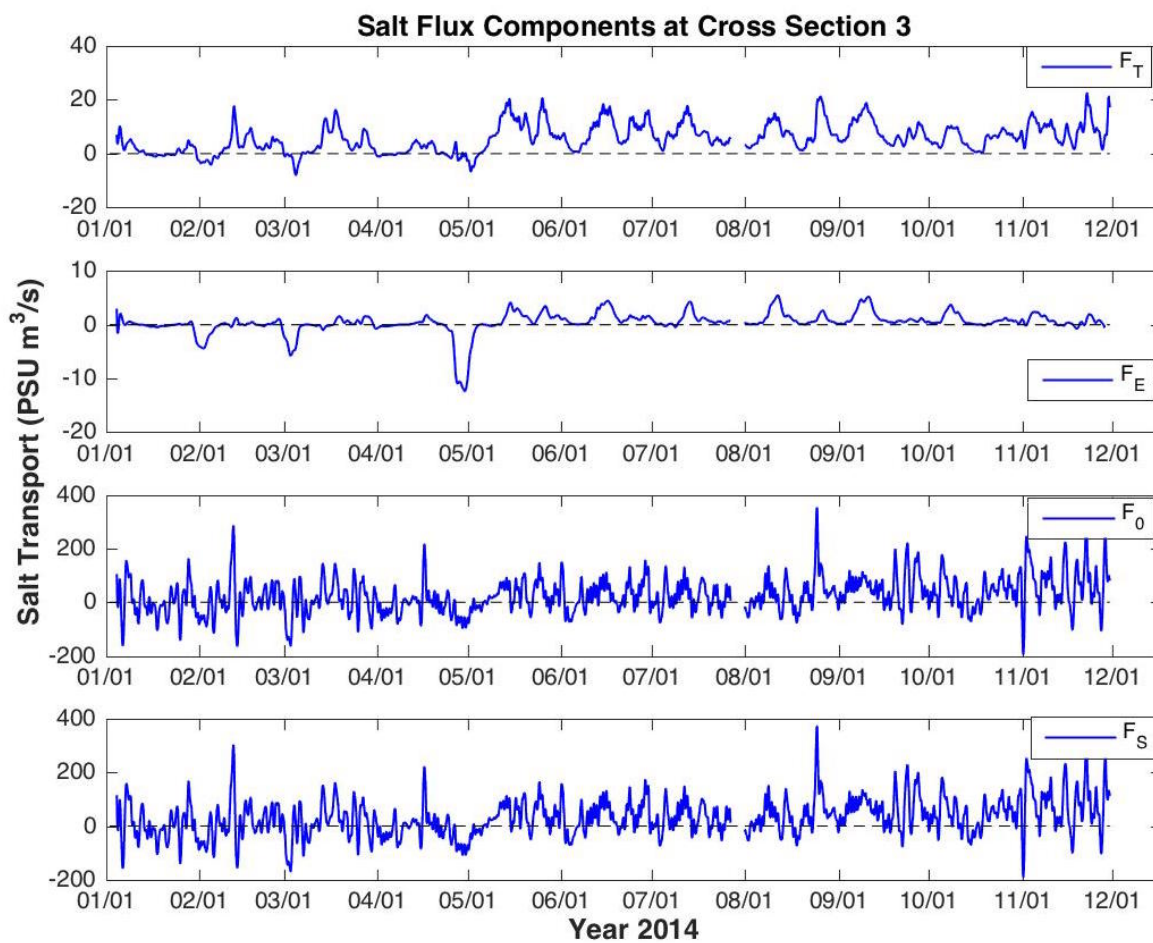


Figure 4.18: The tidal, exchange, residual, and total salt flux at CS3.

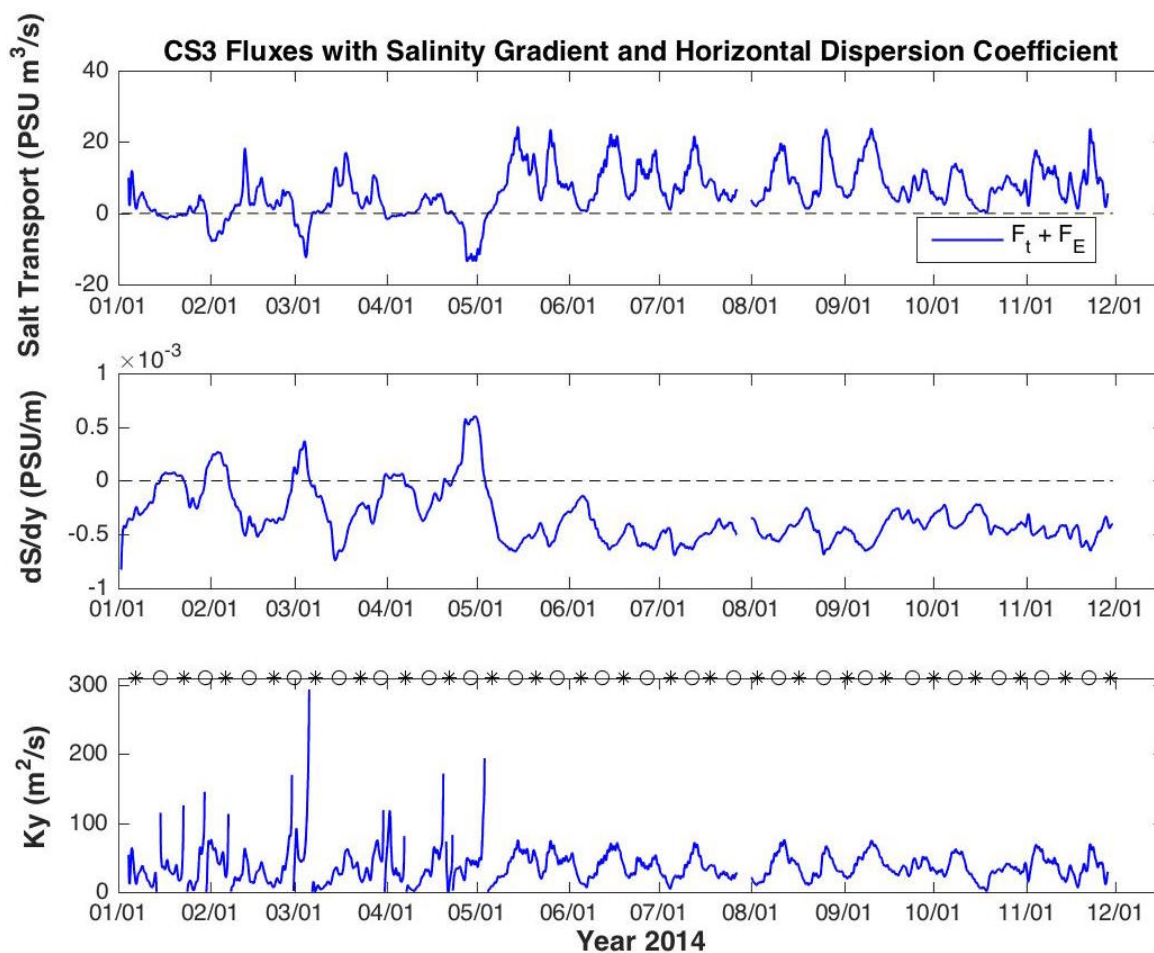


Figure 4.19: (upper panel) The sum of exchange and tidal oscillatory flux. (middle panel) The horizontal salinity gradient. (lower panel) The horizontal dispersion coefficient at CS3 with spring tides indicated by a circle and neap tides indicated by an asterisk.

during periods where freshwater from river discharge does not dominate, the spring/neap cycle is what controls the variability in the horizontal dispersion.

Figure 4.20 shows all kinematic flux components at cross section 4. The tidal oscillatory flux ( $F_T$ ) is always positive at this highest cross section and varies over a range of 0 to  $15.7 \text{ PSU } m^3 \text{ s}^{-1}$ . This means that the movement of salt due to temporal correlations between velocity and salinity is always positive or into the estuary at cross section 4 and is smaller during the period of HRD. The exchange flux ( $F_E$ ), due to vertical and lateral

shear transport, is generally positive throughout the whole year except when there are large pulses of freshwater at the mouth of the Duplin, during the HRD period.  $F_E$  is very small at cross section 4. Tidal flux ( $F_T$ ) dominates the exchange flux ( $F_E$ ) and thus controls the dispersive flux, but the effect is less than at the first, second, and third cross sections. The residual flux ( $F_0$ ), or flux due to advective transport, is almost always positive ranging from -40 to 290  $PSU m^3 s^{-1}$ . This can be interpreted to mean that the movement of salt due to advective transport is generally positive or into the estuary at the most northerly position. As discussed in Figure 4.12, marsh circulation on the western side of the channel can contribute to southward transport that is not accounted for in this measurement. The total salt flux ( $F_S$ ) is very dependent on the advective flux, like at all previous cross sections and ranges from -41 to 300  $PSU m^3 s^{-1}$  and is also generally positive. This can be interpreted to show that the overall movement of salt in the channel is in the positive direction or into the estuary at the fourth cross section.

Figure 4.21 displays the parameters used to calculate the horizontal dispersion from the dispersive flux and the horizontal salinity gradient. The horizontal dispersion coefficient at cross section 4 is also displayed. The dispersive flux is positive at the fourth cross section with occasional negative values during the HRD period. This indicates that the movement of salt is mostly positive or into the estuary in the upper reaches of the Duplin but values are small and range from 0 to 20  $PSU m^3 s^{-1}$ . The horizontal salinity gradient is negative during the LRD period. This fits the model of a normal or positive estuary where the salinity gradient goes from saltier to fresher water as you move from the mouth to the head of the system. There are time points earlier in the year during the period of HRD where the salinity gradient reverses, or where the negative estuary effect can be seen. This is due to large pulses of freshwater being input at the mouth of the Duplin from the Altamaha that can extend to cross section 4. The freshwater water mass will move up the Duplin and at certain times the salinity gradient will reverse. This phenomenon is seen more strongly at cross sections 3 and 4. The horizontal dispersion coefficient,  $Ky$ , becomes very large and more variable

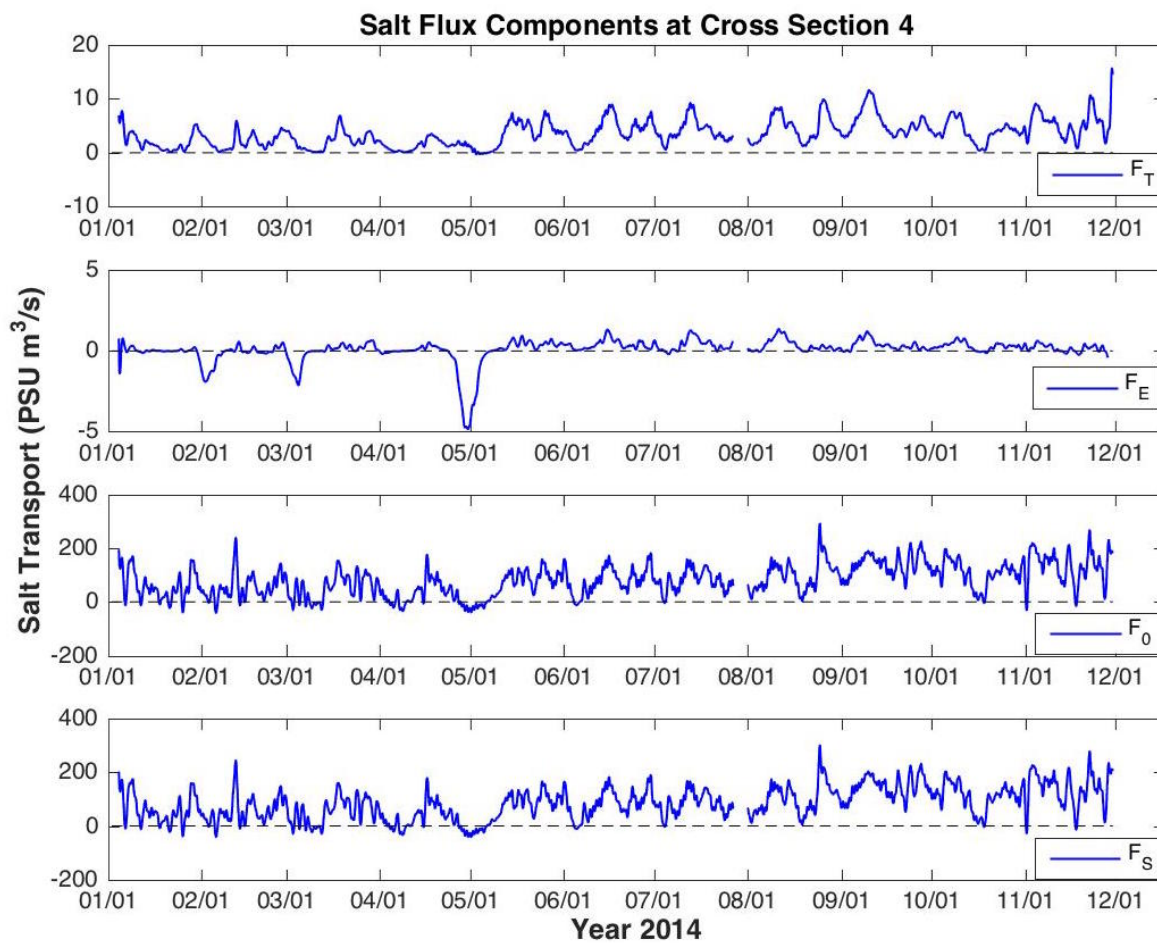


Figure 4.20: The tidal, exchange, residual, and total salt flux at CS4.

during periods of HRD and ranges from 0 to  $400 \text{ m}^2 \text{ s}^{-1}$ . This is very similar to what has been documented at all previous cross sections indicating that the parameterization shown in Equation 4.12 may not be appropriate when the salinity gradient switches from negative to positive and vice versa. After the period of HRD ends and the transition to the LRD period begins,  $Ky$  becomes much less variable and much more predictable. The range of values becomes significantly smaller varying 0 to  $75 \text{ m}^2 \text{ s}^{-1}$ . The timescales of the oscillations begin to follow the spring/neap cycle with maximums on the the spring tides and minimums on the neap tides. This is very similar to what has been seen at all previous cross sections.

#### 4.4 SUMMARY AND CONCLUSIONS

In summary, with respect to advective and dispersive fluxes and horizontal salinity gradients, all cross sections show a range of spatial and temporal fluctuations depending on seasonal forcings associated with HRD periods or LRD when inundation is high. The fluxes are greater at the lower cross sections and the flux decreases in the positive north direction throughout the domain.

The total salt flux ( $F_S$ ) is mainly driven by residual flux ( $F_0$ ) within the Duplin domain. This can be interpreted to show that advective transport is the major driver of salt transport within this domain. Net advective transport is not completely captured by the channel cross sections in the upper reaches of the Duplin as there is much transport over the marsh advecting water out of the Duplin. The dispersive flux is dominated by the tidal flux ( $F_T$ ) compared to the exchange flux ( $F_E$ ) at all cross sections indicating a well mixed system dominated by tidal flows.

Generally, the horizontal salinity gradient follows the classical definition of an estuary, where the gradient is always from salty to fresh in the direction from the mouth to the head respectively. However, during periods of HRD, where pulses of freshwater dominate at the mouth of the system, the salinity gradient will reverse through the middle to the upper ranges of the Duplin. This is the negative estuary effect and is caused by the pulses of freshwater

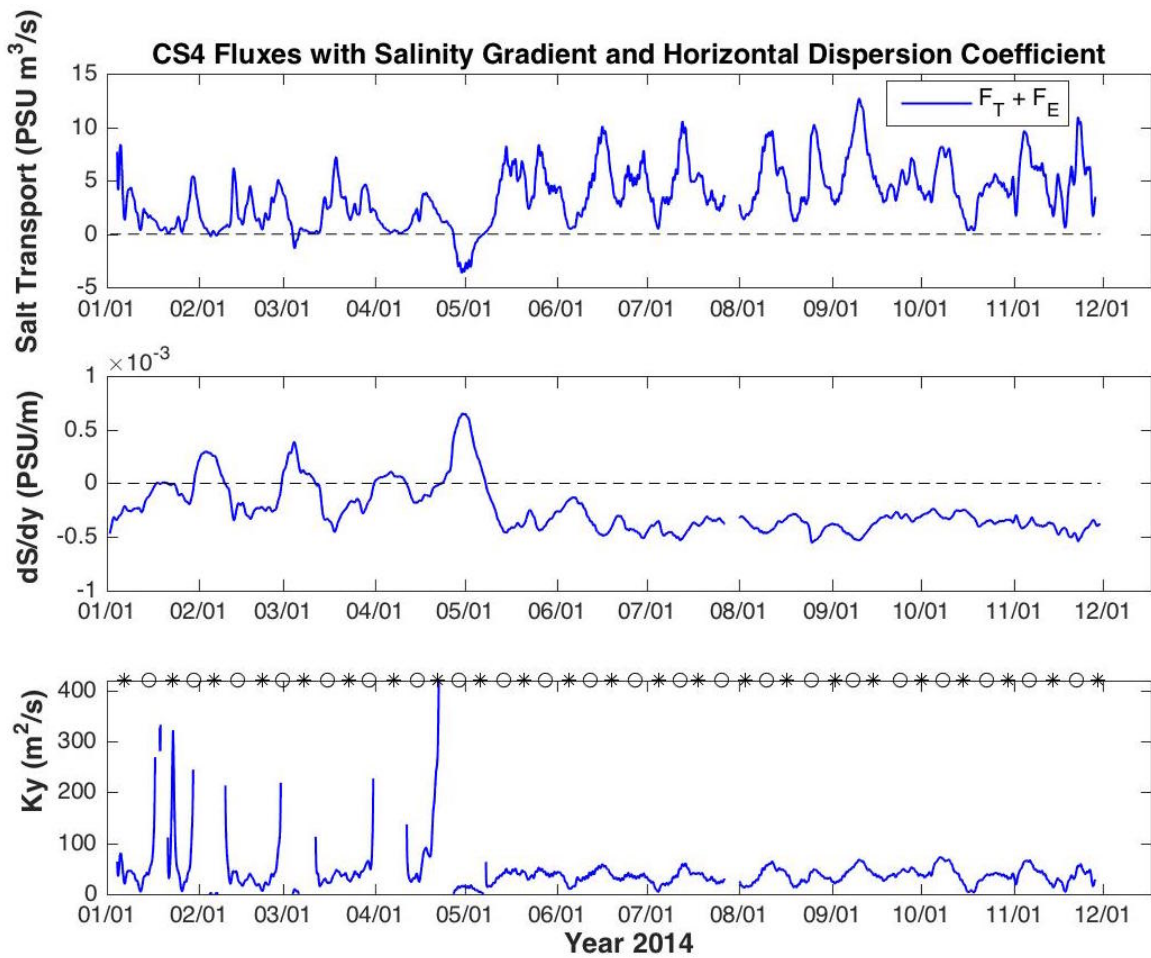


Figure 4.21: (upper panel) The sum of exchange and tidal oscillatory flux. (middle panel) The horizontal salinity gradient. (lower panel) The horizontal dispersion coefficient at CS4 with spring tides indicated by a circle and neap tides indicated by an asterisk.

becoming trapped in the middle ranges of the Duplin. There are large variations in fluxes because of this and this has a strong effect on horizontal dispersion and questions whether the parameterization along a salinity gradient is valid during these times.

In the fall when inundation is relatively high and freshwater within the system is low, the salinity gradient behaves as expected and horizontal dispersion becomes much more regular and predictable at all cross sections. Figure 4.22 displays all values of the horizontal dispersion coefficient at each cross section during time periods of HRD, LRD, and for the whole year of 2014. The HRD period is a two month range from March 1 to May 1, 2014 and the LRD period is the two month period from August 1 to October 1, 2014 when subtidal sea surface heights were high. This figure displays the spatial trend for the horizontal dispersion coefficient from the lower to the upper Duplin. The histogram plot and resulting median values show the amount of variability and where the dominant values are.

During the period of HRD, it can be seen that the horizontal dispersion coefficient is more variable at the first two cross sections, or in the lower ranges of the Duplin, than at the upper two cross sections. The second cross section has the most variability in the calculated horizontal dispersion and together with cross section 1 also has the highest median value. The freshwater input is presumably trapped in the mid ranges of the Duplin and tends to hover between the second and third cross section. This freshwater plug that appears during the period of HRD causes horizontal dispersion to be much higher and much more variable as the salinity gradient crosses the zero axis. The pattern and scale of the horizontal dispersion coefficient is very similar at the third and fourth cross sections, which shows that the upper Duplin can be considered to be homogeneous with respect to horizontal dispersion.

During the period of LRD, horizontal dispersion is much larger and more variable at the lower two cross sections than at the upper two cross sections, especially at cross section one. This is because tidal movement of salty ocean water will dominate at the mouth of the Duplin during this time period. The strong variability is a function of the spring/neap cycle and the median value is  $101.6 \text{ m}^2 \text{ s}^{-1}$ . At the second cross section, horizontal dispersion is

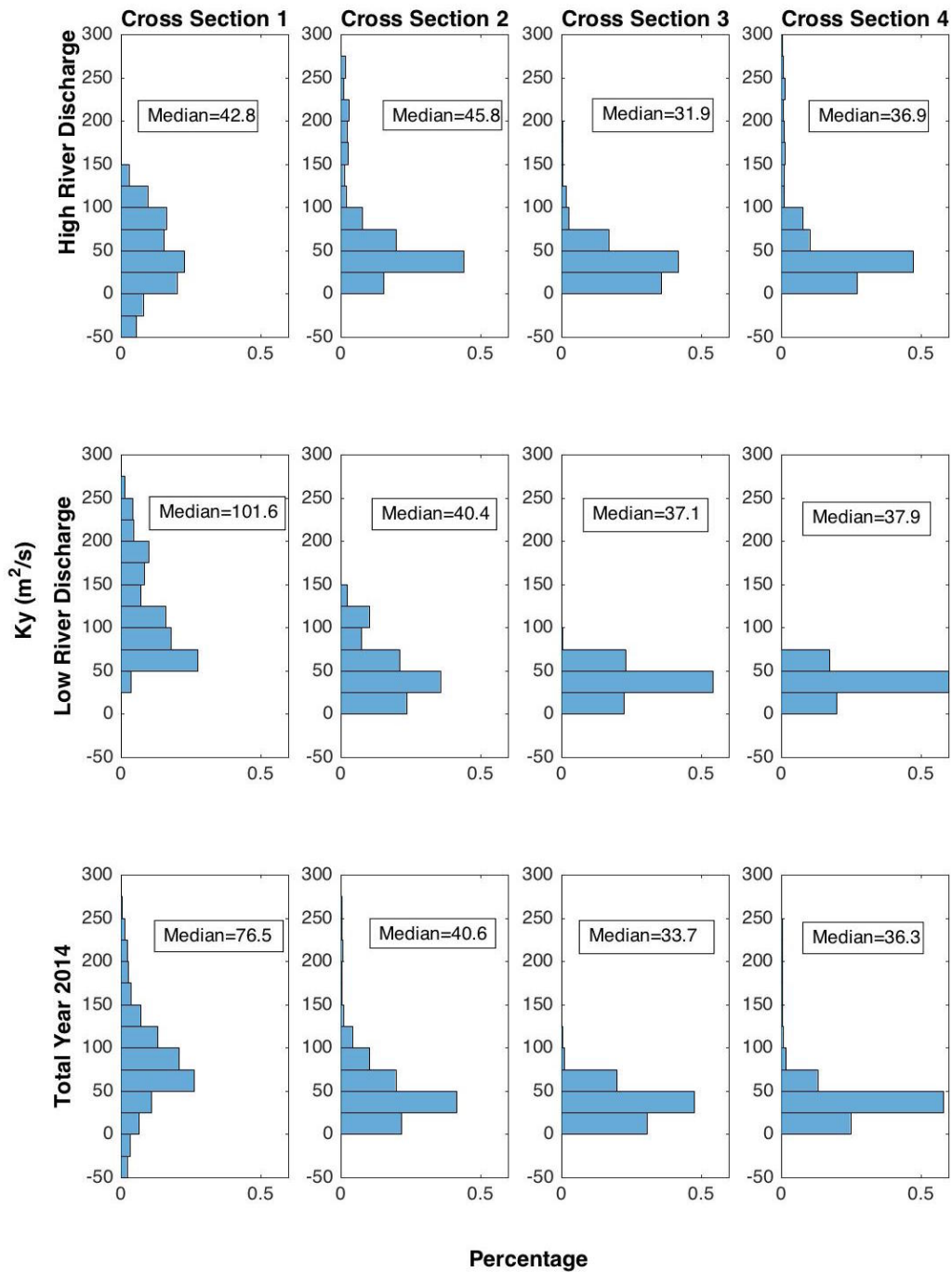


Figure 4.22: Horizontal dispersion coefficients at all cross sections displayed over seasonal scales.

generally smaller but is still larger and more variable than at the higher cross sections. Cross sections 3 and 4 are very similar and appear to be homogeneous with respect to horizontal dispersions much like what was seen during the period of HRD.

The summary for the whole year of 2014, shows that horizontal dispersion is greater and more variable at the first two cross sections and much smaller and more regular at the highest two cross sections. The horizontal dispersion coefficient shows a trend of decreasing values going from the first cross section to the fourth cross section. This makes sense that the movement of salt would be the greatest closer to the mouth of the Duplin where the majority of freshwater and saltwater is input to the domain. The horizontal dispersion coefficient becomes smaller and more regular at the highest two cross sections.

Horizontal dispersion is controlled by tidal advection of riverine freshwater inputs during times when these pulses are prevalent at the mouth of the system. Horizontal dispersion is extremely variable and difficult to predict during these time periods suggesting that the parameterization along the salinity gradient may not be valid when the salinity gradient switches from positive to negative. In times where river inputs are small, horizontal dispersion is controlled by the spring/neap cycle at all cross sections and can easily be predicted based on the location within the system and on where the time point falls with respect to the spring/neap cycle.

## CHAPTER 5

### CONCLUSIONS AND FUTURE RECOMMENDATIONS

#### 5.1 SUMMARY OF MAJOR CONCLUSIONS

A stable, high resolution, three dimensional, hydrodynamic model for the Duplin River has been developed and simulations for 2014 have been produced, which represents an average year in terms of river discharge. This model will be helpful for understanding processes that affect ecosystem function. Overall, the model does well with simulating tidal cycles, tidal constituents, subtidal variations in SSH and salinity, and thus inundation throughout the entire domain. The tidal height comparisons at GCE10 and at Marsh Landing shown in Figures 2.12 and 2.14 display that the model is very capable of accurately representing tidal height throughout the entire Duplin domain with very high  $r^2$  values of 0.98 and 0.97, respectively. The tidal harmonic analysis carried out using T\_tide shows that the model also does a very good job of simulating the major tidal constituents within the Duplin domain. The tidal harmonic analysis on model output and measured data at stations GCE10 and Marsh Landing show that the tidal constituent amplitudes and phases are very similar within the standard deviations.

The subtidal variations of SSH were also estimated well by the model. The model did well at picking up variations in subtidal SSH at both the GCE10 and Marsh Landing stations with  $r^2$  values of 0.91 and 0.93, respectively. The model also performed well at picking up the variations in the subtidal salinity at both the GCE10 and Marsh Landing stations with  $r^2$  values of 0.86 and 0.92, respectively. However, model salinity values were always underestimated. We hypothesize that there are large inputs of salty water overflowing through the northern and western boundaries from Sapelo Sound and the surrounding tidal creeks and

marshes during periods where offshore SSH forcing is large as this is more prevalent later in the year when offshore SSH forcing is known to be largest.

Since tidal and subtidal elevations are well modeled, it can be assumed that inundation patterns in the marsh and mudflats can be accurately measured. Given the large spring/neap variation and offshore forcing, the percent of time a marsh region is under water could also be calculated. How well inundation is modeled depends on the accuracy of the high resolution DEM.

There are three major conclusions that can be made with regards to the Lagrangian particle tracking study. First, particles initiated in the Duplin on the flood tide always have higher residence times than particles initiated in the Duplin on the more energetic ebb tides or simulations started on slack low water will always have higher residence times than simulations started on slack high water regardless of the level of river discharge or level of inundation. Second, particles initiated over the neap tide will always have greater residence times than particles initiated on spring tides regardless of the magnitude of river discharge present or level of inundation. Third, residence times during periods of low river discharge when inundation is generally higher are always higher than residence times during periods of high river discharge, regardless of the stages of the semi-diurnal and spring/neap tidal cycles. It should also be noted that residence time can vary strongly spatially throughout the Duplin domain. This is mainly seen in the upper domain and in the back reaches of Barn and Post Office Creeks and this can be seen over all starting schemes for Lagrangian particles.

Through quantifying residence times or retention and shedding light on the physical drivers that control residence times, processes such as larval recruitment or the efficiency of the wetland to filter contaminants could be better understood. Seasonal, spring/neap cycles, and semi-diurnal tidal cycles could have drastic effects on the amount of time larvae spend within the Duplin system. The spring/neap cycle can be of particular importance due to the influence on inundation patterns (*Bruno and Acha, 2015*). It's possible that organisms could

take advantage of the effects of these different drivers to allow for better recruitment within this estuarine system. Also, wetland efficiency as a natural way to improve water quality is directly tied to residence time within the system (*Savickis et al.*, 2016).

The major conclusions from the Eulerian salt flux analysis are as follows: First, salt flux varies spatially along the Duplin channel with the greatest values in the lower Duplin and decreasing in the upper cross sections. Second, the total salt flux ( $F_S$ ) is mainly driven by the residual flux ( $F_0$ ) which shows that advective transport in the lower Duplin is the major driver of salt transport with a net output of salt. In the upper reaches, the net transport is into the domain along the channel because marsh outflow has not been accounted for. Third, the tidal salt flux dominates the dispersive transport as the exchange flux is small. Fourth, the salinity gradient follows the definition of a classical estuary under low river discharge conditions but can reverse (the negative estuary effect) throughout the mid to upper ranges of the Duplin under high river discharge conditions. Fifth, the horizontal dispersion coefficients can be much more variable under high river discharge forcing scenarios presumably due to fresher water at the mouth of the Duplin and a reversing salinity gradient. During periods of low river discharge, the horizontal dispersion coefficient becomes more regular and periodic, and is controlled by the spring/neap tidal cycle.

## 5.2 FUTURE RECOMMENDATIONS

The model run time should be expanded for a three year period from 2013 to 2015 in order to vary the forcing scenarios. Riverine input and offshore winds that contribute to subtidal SSH, have been proven to be major drivers of the dynamics within the Duplin system and this time period has characteristics of a wet year (2013), a dry year (2015), and a normal year (2014). The freshwater input at the mouth of the Duplin under varying levels of Altamaha discharge will help understand the effect and persistence of the Altamaha River on Duplin processes.

Local winds should also be incorporated into the model as along channel winds can heavily affect water transport and residence times within estuarine systems. Along channel winds have been shown to be the major mechanism that controls estuarine exchange flows when winds are energetic (*Scully et al.*, 2005). Therefore, wind forcing could be important at times within the Duplin domain.

The groundwater inputs should be allowed to vary on temporal scales based on the subtidal salinity averaged over the entire domain. This would allow for a better representation of the recirculated groundwater input that will vary based on the temporally varying salinity within the system and could improve model agreement with subtidal salinity throughout the domain.

The western and upper boundary of the model domain should also be converted to an open boundary to allow for the import and export of water with adjacent tidal channels and sounds. It has been shown that subtidal SSH is a major driver of inundation within this system and during times of high subtidal SSH forcings combined with spring tides, there could be large inputs of salty water from Sapelo Sound overflowing into the Duplin domain. This could be one major reason why the subtidal salinity time series at the GCE10 station underestimates the measured salinity later in the year when offshore (subtidal) SSH forcing is known to be large.

The Duplin model also needs to be coupled or nested into the larger GCE domain model that has been created by collaborator Dr. Castelao within the GCE LTER project (summarized by *Wang* (2016b)). Allowing the model to use the output from the GCE model will create a more robust system that can be used by all collaborators on the GCE LTER project and help better understand connectivities the Duplin has with the coastal waters.

The Eulerian salt flux analysis also should be expanded for the same three year period discussed above. This would tell a more complete story of salt transport throughout the Duplin domain under varied scenarios. This would also allow for the patterns of salt transport to emerge on much longer timescales. For example, are there times when the estuarine

exchange flux will dominate as the stratification increases? The cross sections should also be extended across the marsh to capture the total residual circulation in the upper domain. The counterclockwise circulation with northward transport in the main channel and southward transport over the marsh on the western side presents a unique opportunity to quantify marsh effects on salt transport, particularly if evapotranspiration and pore water salinities are important processes in controlling changes in salinity. A spatially varying friction factor input would need to be used for this based on the vegetation and substrate class present throughout the Duplin domain.

## BIBLIOGRAPHY

- Andutta, F., F. Helfer, L. B. de Miranda, E. Deleersnijder, C. Thomas, and C. Lemckert (2016), An assessment of transport timescales and return coefficient in adjacent tropical estuaries, *Continental Shelf Research*, *124*, 49–62.
- Arega, F. (2013), Hydrodynamic modeling and characterization of Lagrangian flows in the West Scott Creek wetlands system, South Carolina, *Journal of Hydro-Environment Research*, *7*, 50–60.
- Aristizabal, M. F., and R. J. Chant (2015), An observational study of salt fluxes in Delaware Bay, *Journal of Geophysical Research*, *120*, 2751–2768.
- Bales, J., S. Tomlinson, and G. Tillis (2006), Flow and salt transport in the Suwannee River estuary, Florida, 1999-2000: Analysis of data and three-dimensional simulations, *Tech. rep.*, US Geological Service.
- Bilgili, A., J. Proehl, D. Lynch, K. Smith, and R. Swift (2005), Estuary/ocean exchange and tidal mixing in a Gulf of Maine estuary: A Lagrangian modeling study, *Estuarine, Coastal and Shelf Science*, *65*, 607–624.
- Blanton, J. O., and L. P. Atkinson (1983), Transport and fate of river discharge on the Continental Shelf of the Southeastern United States, *Journal of Geophysical Research*, *88*, 4730–4738.
- Bodin, H., J. Persson, J.-E. Englund, and P. Milberg (2013), Influence of residence time analyses on estimates of wetland hydraulics and pollutant removal, *Journal of Hydrology*, *501*, 1–12.

- Bruno, D. O., and E. M. Acha (2015), Winds vs. tides: factors ruling the recruitment of larval and juvenile fishes into a micro-tidal and shallow choked lagoon (Argentina), *Environmental Biology of Fishes*, *98*, 1449–1458.
- Carter, E., S. White, and A. Wilson (2008), Variation in groundwater salinity in a tidal marsh basin, North Inlet estuary, South Carolina, *Estuarine, Coastal and Shelf Science*, *76*, 543–552.
- Chen, C., and H. Liu (2003), An unstructured grid, finite-volume, three-dimensional, primitive equations ocean model: Application to coastal ocean and estuaries, *Journal of Atmospheric and Oceanic Technology*, *20*, 159–186.
- Chen, C., R. Beardsley, and G. C. et al. (2013), *FVCOM User Manual*, SMAST/UMASSD.
- Chen, S., W. Geyer, D. Ralston, and J. Lerczak (2012), Estuarine exchange flow quantified with isohaline coordinates: Contrasting long and short estuaries, *Journal of Physical Oceanography*, *42*, 748–763.
- Devkota, J., and X. Fang (2015), Quantification of water and salt exchanges in a tidal estuary, *Water*, *7*, 1769–1791.
- Devkota, J., X. Fang, and V. Fang (2013), Response characteristics of the Perdido and Wolf Bay system to inflows and sea level rise, *British Journal of Environment and Climate Change*, *3*, 229–256.
- DiIorio, D., and R. M. Castelao (2013), Dynamical response of salinity to freshwater discharge and wind forcing in adjacent estuaries on the Georgia coast, *Oceanography*, *26*, 44–51.
- DiIorio, D., and K. R. Kang (2007), Variations in turbulent flow with river discharge in the Altamaha River estuary, Georgia, *Journal of Geophysical Research*, *112*, C05,016.
- Fischer, H. B. (1973), Longitudinal dispersion and turbulent mixing in open-channel flow, *Annual Review of Fluid Mechanics*, *5*, 59–78.

- Hladik, C., and M. Alber (2014), Classification of salt marsh vegetation using edaphic and remote sensing-derived variables, *Estuarine, Coastal and Shelf Science*, 141, 47–57.
- Hladik, C., J. Schalles, and M. Alber (2013), Salt marsh elevation and habitat mapping using hyperspectral and LIDAR data, *Remote Sensing of Environment*, 139, 318–330.
- Huhn, F., A. von Kameke, S. Allen-Perkins, P. Montero, A. Venancio, and V. Perez-Munuzuri (2012), Horizontal Lagrangian transport in a tidal-driven estuary: Transport barriers attached to prominent coastal boundaries, *Continental Shelf Research*, 39-40, 1–13.
- Jonsson, B., K. Doos, K. Myrberg, and P. Lundberg (2011), A Lagrangian-trajectory study of a gradually mixed estuary, *Continental Shelf Research*, 31, 1811–1817.
- Kenov, I., A. C. Garcia, and R. Neves (2012), Residence time of water in the Mondego Estuary, Portugal, *Estuarine, Coastal and Shelf Science*, 106, 13–22.
- Kim, C., and K. A. Park (2012), A modeling study of water and salt exchange for a micro-tidal, stratified northern Gulf of Mexico estuary, *Journal of Marine Systems*, 96-97, 103–115.
- Kjerfve, B. (1973), *Volume Transport, salinity distribution, and net circulation in the Duplin estuary, Georgia*, UGAMI and Ga. Tech.
- Lerczak, J. A., W. R. Geyer, and R. J. Chant (2006), Mechanisms driving the time-dependent salt flux in a partially stratified estuary, *Journal of Physical Oceanography*, 36, 2296–2311.
- MacCready, P. (2011), Calculating estuarine exchange flow using isohaline coordinates, *Journal of Physical Oceanography*, 41, 1116–1124.
- McKay, P. (2008), Temporal and spatial variability of transport and mixing mechanisms using heat and salt in the Duplin River, Georgia, Ph.D. thesis, University of Georgia.
- McKay, P., and D. DiIorio (2008), Heat budget for a shallow, sinuous salt marsh estuary, *Continental Shelf Research*, 28, 1740–1753.

- McKay, P., and D. DiIorio (2010), Cycle of vertical and horizontal mixing in a shallow tidal creek, *Journal of Geophysical Research*, *115*, C01,004.
- Mellor, G., and T. Yamada (1982), Development of a turbulence closure model for geophysical fluid problems, *Reviews of Geophysics and Space Physics*, *20*, 851–875.
- Musner, T., A. Bottacin-Busolin, M. Zaramella, and A. Marion (2014), A contaminant transport model for wetlands accounting for distinct residence time bimodality, *Journal of Hydrology*, *515*, 237–246.
- Pawlowicz, R., B. Beardsley, and S. Lentz (2002), Classical tidal harmonic analysis including error estimates in MATLAB using T-TIDE, *Computers and Geosciences*, *28*, 929–937.
- Persson, J., N. Somes, and T. Wong (1999), Hydraulics efficiency of constructed wetlands and ponds, *Water Science Technology*, *40*, 291–300.
- Porubsky, W., S. Joye, W. Moore, K. Tuncay, and C. Meile (2011), Field measurements and modeling of groundwater flow and biogeochemistry at Moses Hammock, a backbarrier island on the Georgia coast, *Biogeochemistry*, *104*, 69–90.
- Ragotzkie, R. A., and R. A. Bryson (1955), Hydrography of the Duplin River, Sapelo Island, Georgia, *Bulletin of Marine Science of the Gulf and Caribbean*, *5*, 297–314.
- Safak, I., P. Wiberg, D. Richardson, and M. Kurum (2015), Controls on residence time and exchange in a system of shallow coastal bays, *Continental Shelf Research*, *97*, 7–20.
- Savickis, J., A. Bottacin-Busolin, M. Zaramella, N. Sabokrouhiyeh, and A. Marion (2016), Effect of a meandering channel on wetland performance, *Journal of Hydrology*, *535*, 204–210.
- Schultz, G., and C. Ruppel (2002), Constraints on hydraulic parameters and implications for groundwater flux across the upland-estuary interface, *Journal of Hydrology*, *260*, 255–269.

- Schulz, E., H. Schuttelaars, U. Grawe, and H. Burchard (2015), Impact on the depth to width ratio of periodically stratified tidal channels on the estuarine circulation, *Journal of Physical Oceanography*, *45*, 2048–2069.
- Scully, M. E., C. Friedrichs, and J. Brubaker (2005), Control of estuarine stratification and mixing by wind-induced straining of the estuarine density field, *Estuaries*, *28*, 321–326.
- Silva, C., C. Marti, and J. Imberger (2014), Horizontal transport, mixing, and retention in a large shallow estuary: Rio de la Plata, *Environmental Fluid Mechanics*, *14*, 1173–1197.
- Smagorinsky, J. (1963), General circulation experiments with the primitive equations, *Monthly Weather Review*, *91*, 99–164.
- Smith, R. (1980), Buoyancy effects upon longitudinal dispersion in wide well-mixed estuaries, *Phil. Trans. R. Soc. Lond.*, *296*, 467–496.
- Snyder, M., M. Taillefert, and C. Ruppel (2004), Redox zonation at the saline-influenced boundaries of a permeable surgical aquifer: effects of physical forcing on the biogeochemical cycling of iron and manganese, *Journal of Hydrology*, *296*, 164–178.
- Spencer, D., C. Lemckert, Y. Yu, J. Gustafson, S. Lee, and H. Zhang (2014), Quantifying dispersion in an estuary: A Lagrangian drifter approach, *Journal of Coastal Research*, *70*, 29–34.
- Traynum, S., and R. Styles (2008), Exchange flow between two estuaries connected by a shallow tidal creek, *Journal of Coastal Research*, *24*, 1260–1268.
- Wang, S. (2016a), Inorganic carbon and oxygen dynamics in a marsh-dominated estuary, Master's thesis, University of Georgia.
- Wang, Y. (2016b), Fronts and variability in the coastal ocean, Ph.D. thesis, University of Georgia.

Weber, A., and J. Blanton (1980), Monthly mean wind fields for the South Atlantic Bight, *Journal of Physical Oceanography*, 10, 1,256–1,263.

Zou, T., H. Zhang, Q. Meng, and J. Li (2016), Seasonal hydrodynamics and salt exchange of a shallow estuary in northern China, *Journal of Coastal Research*, 74, 95–103.